# DEVELOPMENT OF ATMOSPHERIC PLASMA SYSTEM BY DIELECTRIC BARRIER DISCHARGE

**PONGSATHON JITSOMBOONMIT**

**A THESIS SUBMITTED IN PARTIAL FULFILLMENT
OF THE REQUIREMENTS FOR
THE DEGREE OF MASTER OF SCIENCE (PHYSICS)
FACULTY OF GRADUATE STUDIES
MAHIDOL UNIVERSITY
2010**

Thesis
entitled

# DEVELOPMENT OF ATMOSPHERIC PLASMA SYSTEM BY DIELECTRIC BARRIER DISCHARGE

……………………………………………
Mr. Pongsathon Jitsomboonmit
Candidate

……………………………………………
Lect. Somsak Dangtip, Ph.D.
Major advisor

……………………………………………
Asst. Prof. Tanakorn Osotchan, Ph.D.
Co-advisor

……………………………………………
Asst. Prof. Toemsak Srikhirin, Ph.D.
Co-advisor

……………………………………………
Prof. Banchong Mahaisavariya,
M.D., Dip Thai Board of Orthopedics
Dean
Faculty of Graduate Studies
Mahidol University

……………………………………………
Assoc. Prof. Wannapong Triampo, Ph.D.
Program Director
Master of Science Program in Physics
Faculty of Science, Mahidol University

Thesis
entitled

**DEVELOPMENT OF ATMOSPHERIC PLASMA SYSTEM BY DIELECTRIC BARRIER DISCHARGE**

was submitted to the Faculty of Graduate Studies, Mahidol University
for the degree of Master of Science (Physics)
on
May 26, 2010

……………….…………….…..………
Mr. Pongsathon Jitsomboonmit
Candidate

………………….…..………………
Asst. Prof. Mudtorlep Nisoa, Ph.D.
Chair

………………….…..……….………
Lect. Somsak Dangtip, Ph.D.
Member

……………………..…..……………...…
Asst. Prof. Toemsak Srikhirin, Ph.D.
Member

……………………..…..………………..
Asst. Prof. Tanakorn Osotchan, Ph.D.
Member

……………………..…..……………...…
Prof. Banchong Mahaisavariya,
M.D., Dip Thai Board of Orthopedics
Dean
Faculty of Graduate Studies
Mahidol University

……………………..…..……………...…
Prof. Skorn Mongkolsuk, Ph.D.
Dean
Faculty of Science
Mahidol University

# ACKNOWLEDGEMENTS

This thesis can be succeeded by the attentive support from my major advisor Lect. Somsak Dangtip, co-advisors, Assist. Prof. Tanakorn Osotchan and Assist. Prof. Toemsak Srikhirin. I would like to thank to them for their kindness, valuable advice, helpful guidance and encouragement throughout my study.

I would like to thanks Assist. Prof. Mudtorleb Nisoa and his staffs at experimental physics research unit of Walailuck University for their initiating and teaching atmospheric plasma research field.

This thesis could not be complete without the help from all members in the Thin Film, K406 laboratory through discussion and giving hands in solving the problems, in particular, Mr. Narongchai Boonyopakorn and Ms. Suthisa Leasen, for their useful comments and lathing metal electrodes.

I would also like to acknowledge NANOTEC Centre of Excellence at Mahidol University for financial support.

Finally, I would like to express my gratitude to my family for taking care, supporting and encouraging me. Without them, my study could not be accomplished.

Pongsathon Jitsomboonmit

DEVELOPMENT OF ATMOSPHERIC PLASMA SYSTEM BY DIELECTRIC BARRIER DISCHARGE

PONGSATHON JITSOMBOONMIT 4936252 SCPY/M

M.Sc. (PHYSICS)

THESIS ADVISORY COMMITTEE: SOMSAK DANGTIP, Ph.D., TANAKORN OSOTCHAN, Ph.D., TOEMSAK SRIKHIRIN, Ph.D.

## ABSTRACT

Atmospheric Plasma (AP) may be generated by dielectric barrier discharge (DBD) technique. In such a system, electrodes are arranged in the form of two parallel plates; one or both electrodes are covered by dielectric materials. A high voltage power supply at medium or high frequency is normally required in a DBD system. This work presents the development of a high voltage medium frequency power supply. A full bridge or H-bridge inverter, controlled by IC TL494CN, is employed to convert DC voltage into 17-kHz square wave signals. The square wave signals are then filtered by 2.4-mH inductor before feeding the primary winding of a 1:20 step-up transformer. The output voltage of up to 17 $kV_{p\text{-}p}$ is sinusoidal by means of resonance circuit.

The developed AP system was used to generate plasma from argon, helium, nitrogen and air. Their discharged characteristics were analyzed by snap-shot photographs, voltage-current characteristic, *Lissajous Figure* and optical emission spectroscopy (OES). Helium started the first discharge of a few μs long at 2 $kV_{p\text{-}p}$ and added the second discharge of a few ten μs at 4 $kV_{p\text{-}p}$. The former discharge is understood as a glow-like discharge while the latter as Townsend-like one. In the 6 $kV_{p\text{-}p}$ range, four discharge peaks were observed in total. Argon had its first discharge at about 5 $kV_{p\text{-}p}$. Nitrogen and air plasma were more difficult to discharge. They did not glow even up to the maximum 17 $kV_{p\text{-}p}$, but rather showed filamentary discharge instead. OES confirmed characteristic spectral lines of each gas. Applications of atmospheric argon plasma have been demonstrated by treating ITO thin films and tapioca starch. The water contact angle of ITO surface reduced after treating with plasma. The effect was stronger with increased power and a longer treatment time. OES and a scanning electron micrograph of starch showed starch molecules have undergone the cross-linking process after plasma treatment.

KEY WORDS: ATMOSPHERIC PLASMA/ HIGH VOLTAGE POWER SUPPLY/ APGD/ MATERIAL MODIFICATION/ SURFACE TREATMENT

101 pages

การพัฒนาระบบผลิตพลาสมาที่ความดันบรรยากาศแบบไดอิเล็กตริกแบริเออร์
DEVELOPMENT OF ATMOSPHERIC PLASMA SYSTEM BY DIELECTRIC BARRIER DISCHARGE

พงศธร จิตสมบูรณ์มิตร 4936252 SCPY/M

วท.ม. (ฟิสิกส์)

คณะกรรมการที่ปรึกษาวิทยานิพนธ์ : สมศักดิ์ แดงติ๊บ, Ph.D., ธนากร โอสถจันทร์, Ph.D., เติมศักดิ์ ศรีคิรินทร์, Ph.D.

## บทคัดย่อ

พลาสมาที่ความดันบรรยากาศสามารถสร้างด้วยเทคนิคไดอิเล็กตริกแบริเออร์ ในระบบดังกล่าว แผ่นอิเล็กโตรดคู่ขนาน แผ่นใดแผ่นหนึ่งหรือทั้งสองแผ่นจะมีฉนวนครอบอยู่ แหล่งกำเนิดไฟฟ้าศักย์สูงและความถี่กลาง ๆ หรือสูง เป็นอุปกรณ์หลักใน ระบบ งานวิจัยนี้นำเสนอการออกแบบวงจรไฟฟ้าของเครื่องจ่ายไฟฟ้าศักย์สูงความถี่ปานกลาง โดยใช้ฟูลบริดจ์คอนเวอร์เตอร์ที่ควบคุมจากไอซี TL494CN ทำหน้าที่แปลงไฟกระแสตรง ให้เป็นสัญญาณรูปร่างสี่เหลี่ยมมีความถี่ 17 kHz ก่อนที่จะกรองโดยตัวเหนี่ยวนำ 2.4 mH แล้วจึงจ่ายให้กับหม้อแปลงขึ้นที่มีอัตราส่วนขดลวดเป็น 1:20 สัญญาณไฟฟ้าขาออกเป็นคลื่นรูปซายน์จากการทำงานของวงจรกำทอนจะปรับค่าความต่างศักย์ได้ในช่วง 0-17 $kV_{p-p}$

ระบบผลิตพลาสมาที่ความดันบรรยากาศถูกนำไปจุดโดยใช้ก๊าซอาร์กอน ฮีเลียม ไนโตรเจน และอากาศ คุณลักษณะของพลาสมาที่ความดันบรรยากาศถูกวิเคราะห์จาก รูปถ่าย คุณลักษณะของศักย์ไฟฟ้าและกระแส *Lissajous Figure* และ สเปกตรัมทางแสงที่ให้ออกมา (OES) ฮีเลียมเกิดการคายตัวและอาร์กอนจะมีลักษณะเป็นเนื้อเดียวกันในขณะที่ไนโตรเจนและอากาศจะมีลักษณะเป็นfilament อย่างไรก็ตามพลาสมาที่เป็นเนื้อเดียวกันนั้นสามารถแบ่งออกได้เป็นอีก2ประเภทนั้นคือ atmospheric glow discharge (APGD) and atmospheric Townsend discharge (APTD) ซึ่งขึ้นอยู่กับคุณลักษณะของกระแสดิสชาร์จ การประยุกต์ใช้พลาสมาที่ความดันบรรยากาศถูกสาธิตโดยการนำฟิล์มบางITOและแป้งมันสำปะหลังมาผ่านอาร์กอนพลาสมา โดยหยดน้ำบนฟิล์มบางITOลดลงเมื่อเพิ่มกำลังไฟฟ้าและระยะเวลาการผ่านพลาสมา และผล OESและ SEMของแป้งนั้นชี้ให้เห็นถึงการทำปฏิกิริยาระหว่างอนุมูลอิสระในพลาสมากับโมเลกุลของแป้ง

101 หน้า

# CONTENTS

## CONTENTS (cont.)

# LIST OF TABLES

# LIST OF FIGURES

# LIST OF FIGURES (cont.)

# LIST OF FIGURES (cont.)

# LIST OF FIGURES (cont.)

# LIST OF FIGURES (cont.)

# LIST OF FIGURES (cont.)

# CHAPTER I
# INTRODUCTION

There are two major environments to generate plasma; one at low pressure (LP) and the other at atmospheric pressure. In the former case, radio frequency (RF) generator has played a major role for plasma operation. Its system requires vacuum condition and impedance matching network [1]. This makes the system expensive and limits sample size to the size of a vacuum chamber which is less attractive for commercial industry. The low pressure plasma system, on the other hand is, advantageous in providing clean condition and uniform plasma. LP plasma can be operated in either capacitively-couple plasma mode (CCP) or inductively couple plasma mode (ICP). In the other case, atmospheric plasma offers a possibility to build a system at more affordable cost by using MOSFET and IGBT components. These components can switch at very high speed in range of a few kHz to a few MHz [2-4]; therefore, eliminate the need for costly matching network [5]. As this system operates at atmospheric pressure, vacuum condition is no longer needed [6-8]. However, atmospheric plasma also has many drawbacks such as heat loss in electrodes, contamination following an exposure to air [9], and larger gas.

Many recent researches have been focus on atmospheric plasma which has a large potential that can be applied into large scale industries. Many type of atmospheric pressure plasmas are investigated such as dielectric barrier discharges (DBDs) [6-8], corona discharge and atmospheric plasma torch [7, 8, 10]. The DBD technique was initially used to generate ozone about decades ago; Nowadays DBDs is the important technique in semiconductor industries, textile industries and etc. In this work, dielectric barrier discharge is chosen and developed due to the ease in designing, in operating and suitability for treating thin and flat substrates.

DBDs technique needs a high voltage AC power supply and a plasma chamber. The former part is commercially available but with considerably dearly tagged price. The latter part has to be custom-made to suit user's applications. It is thus a focus of this thesis to be an alternative for fabricating an affordable high power medium frequency with most components and parts available locally and with relatively simple plasma chamber.

**Objectives**

- To design and construct dielectric barrier discharge plasma system for generating plasma at near or atmospheric pressure
- To characterize plasma generated from the system under various conditions
- To study effects of plasma treatment on surface properties of ITO and other organic materials

# CHAPTER II
# LITERATURE REVIEW

## 2.1 Introduction to Plasma

Plasma is usually considered to be the fourth state of matter. Naturally, 99% of our universe consists of plasma in forms of stars, nebular and also interstellar medium. Plasma also appears in the earth such as lightning, aurora, flame and etc. Man-made plasma can be achieved by a number of methods under various conditions depending on their applications [11].

Plasma occurs over a wide range of temperatures and pressures (see Fig. 2.1). Plasma composes of ionized gas or charged particles, neutral molecules and also electrons. All plasma contains positive charges approximately equal to negative charges, so that its total space charge approaches zero. In general, plasma can be classified into two types, i.e., *thermal equilibrium plasma* and *non-thermal equilibrium plasma* [8, 11-13].

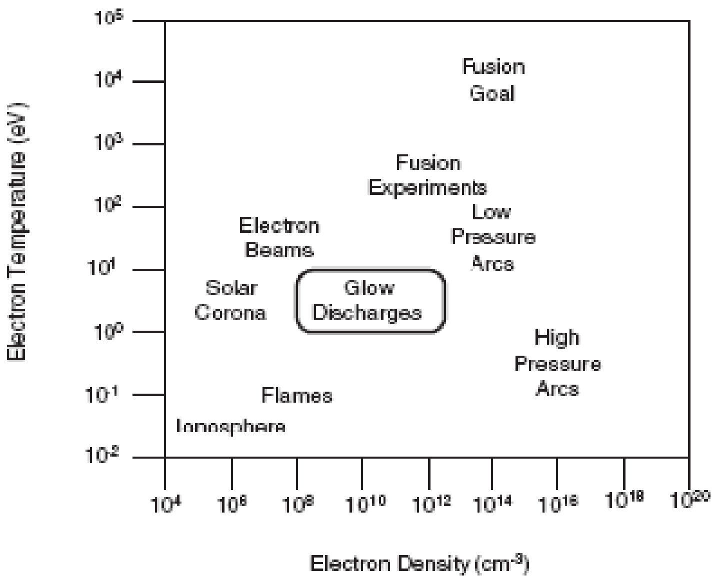


**Figure 2.1** Types of plasma and their electron density Vs electron kinetic energy [14].

*Thermal equilibrium plasma*, ions temperature is equal to electrons temperature [11] (often at temperature >10,000 ˚C) such as stellar interiors, lightning and thermonuclear plasma. *Non-thermal equilibrium plasma* has the bulk gas at room temperature, while the electron temperature can be 10 to 100 times of ion temperature [11] (as hot as 10,000 ˚C). *Non-thermal equilibrium plasma* will be focused on this work. Table 2.1 shows various applications of non-thermal and thermal equilibrium plasma at atmospheric pressure.

**Table 2.1** Typical applications of non-thermal and thermal equilibrium plasma at atmospheric pressure.

| Non-thermal equilibrium | Thermal equilibrium |
|---|---|
| **Etching** | **Cutting** |
| **Plasma Cleaning** | **Surface Hardening** |
| **Fluorescent lamps** | **Metal Welding** |
| **Ozone production** | |

## 2.2 Gas Discharge Phenomena

### 2.2.1 V-I Characteristics

Gas discharge experiment may be carried out in a simple setup to study about types of cold plasma and discharge behavior. A couple of metal planar electrodes inserted into a glass tube that can be evacuated and filled with various gases such as argon. Both electrodes are then connected to adjustable DC power supply. The voltage across the electrodes and current in a circuit are then measured. Cold plasma can be classified depend upon their V-I characteristic (see Fig. 2.2).

As the pressure is approximately at 1 Torr, at initial state **AB**, low voltage is supply the electrodes with small current. In this region there is only background ionization occurring in gas tube which may be the result from cosmic ray collision or radioactive radiation [11]. As the voltage increase further to **BC** region, the current remain constant because all available electrons and ions will recombine, then ionization rate is constant so-called saturation region. If the voltage still increases beyond point **C**, the current will rise exponentially from electron avalanche however the discharge cannot sustain itself. The region **CE** is called Townsend discharge region. The breakdown voltage is in Townsend discharge at point **E** that the voltage will drop dramatically while current will sharply increase and visible light is observed. Next state from breakdown voltage is glow discharge which visible plasma is ignited. In **FG** region called normal glow discharge region, the voltage is independent from the discharge current. The current density remains constant although total current increase that affect the change of plasma area covering cathode. At point **G**, plasma will cover the entire cathode surface. Beyond this point, the voltage as well as the current will increase due to no further free cathode surface so the increasing voltage causes the cathode current density to rise. This discharge is called abnormal glow discharge. The last region is the arc discharge region, when the cathode current density rise in abnormal region, the cathode will be heated up. Then it will emit thermionic electrons. In this region plasma become hot and the voltage will drop while the current increases.

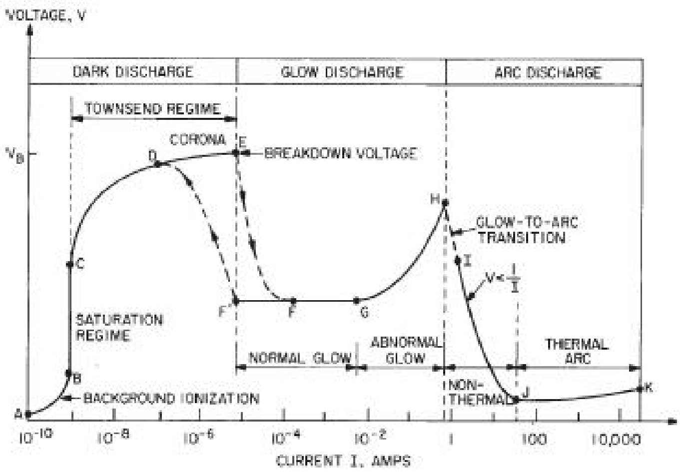


**Figure 2.2** Universal V-I characteristic of DC low pressure discharge tube [15].

### 2.2.2 Townsend Mechanism

To understand gas breakdown mechanism, let's consider an avalanche which starts from only one free electron in space which in turn, comes from comic ray ionization or radioactive radiation. Gas breakdown usually starts from such an avalanche that will generate many new electrons along their movement from any point in space to anode so this process is a source of many primary electrons in cascade ionization as shown in Fig. 2.3.

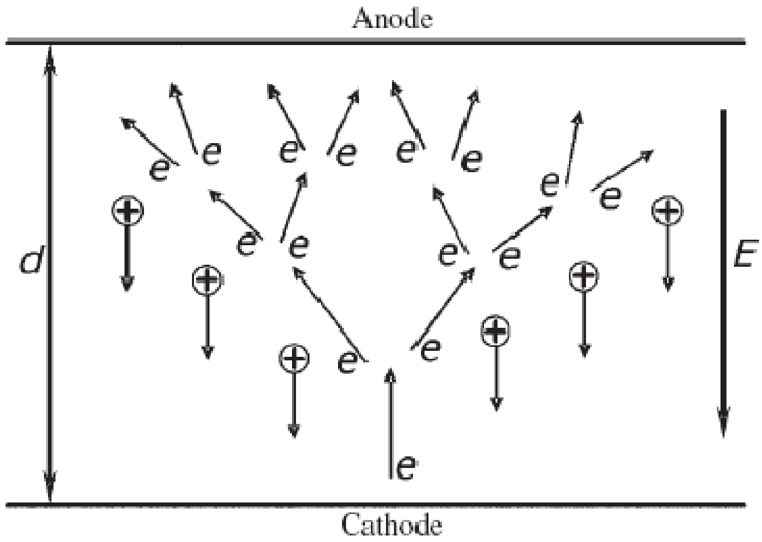


**Figure 2.3** Illustration of the Townsend breakdown gap [12].

Let's assume that the electric field between parallel electrodes is homogeneous. Starting with one seeding electron, it will be accelerated by electric field toward an anode and then ionize gas on its trajectory to produce secondary electron which will be a chain reaction so an avalanche occurs. Consider at any small space gap $dx$;

$$\frac{dN}{dx} = \alpha N \qquad 2.1$$

where $N$ is number of electron at any $x$ and $\alpha$ is a proportionality. So $N(x) = exp(\alpha x)$ for one electron seed. However, there are many electrons from primary process that can be electron seeds so the equation will be;

$$N(x) = N_0 exp(\alpha x) \qquad 2.2$$

or rewritten in term of number of electrons per unit length

$$n(x) = n_0 exp(\alpha x) \qquad 2.3$$

The constant $\alpha$ has an important role to describe ionization in avalanche called *Townsend ionization coefficient*. From numerical and experimental analysis of discharge, simplify expression of $\alpha$ was introduced by Townsend as

$$\frac{\alpha}{p} = Aexp\left[-\frac{B}{E/p}\right] \qquad 2.4$$

where $E$ and $p$ are electric field and pressure respectively. The constant $A$ and $B$ are determined by approximating the experimental discharge curves. According to electron avalanche, each primary electron generated near cathode produces positive ion so total number of positive ions ($N^+$) creating from single ionization cascade will be;

$$N^+ = exp(\alpha d) - 1 \qquad 2.5$$

which $d$ represents the gap width. So all the $N^+$ ions are accelerated toward the cathode, impinge on the cathode and then knock electrons out from cathode. This process is called *secondary electron emission process* which plays important role to sustain the discharge or plasma. Neglect the effects from electron capture from electronegative gas and loss from recombination so $N^+$ ion will create $\gamma[exp(\alpha d) - 1]$ electrons where $\gamma$ is *secondary electron coefficient* implying the probability to knock out secondary electron by an ion impact. To sustain the discharge, the $N^+$ positive ion have to generate at least one secondary electron to be an electron seed of new avalanche so the condition to sustain the discharge can be expressed in the following form;

$$\gamma[exp(\alpha d) - 1] = 1 \qquad 2.6$$

*Townsend mechanism* is used to explain and understand how the plasma ignite and sustain itself. However, in electronegative gases such as air, oxygen or halogen compound gases, the attachment of electron to such gases cannot be ignored. This point will be discussed again later.

### 2.2.3 The Streamer

To describe gas discharge at high pressure, *Townsend mechanism* was not successful in explaining a dependency of breakdown voltage on gas pressure and electrode configuration. Also *Townsend mechanism* predicts that plasma to be diffused discharge, the discharge at atmospheric pressure was found to have a filamentary form. As a result, around 1940, Rather, Meek and Loeb independently proposed the *"Streamer theory"* [12].

Consider an electron avalanche, the space charge was created and the applied electric field was distorted. This is noticeable when charge concentration is about $10^6$ [11]. However, if space charge concentration in avalanche is more than $10^8$ [11, 12], the distorted field is the same magnitude as applied field leading to the formation of a thin column of conducting ions called the streamer.

When the streamer connects the electrodes, current increases significantly to form spark. In the case of the gap and the overvoltage are not too high, the avalanche can reaches anode, the streamer is initiated and then propagates to cathode so called cathode-directed streamer or positive streamer (see Fig. 2.4). If the gap and overvoltage is high, the avalanche transforms to streamer before reaching the anode. The streamer can propagates to both electrodes but mostly grow to the anode so called anode-directed streamer or negative streamer (see Fig. 2.5).

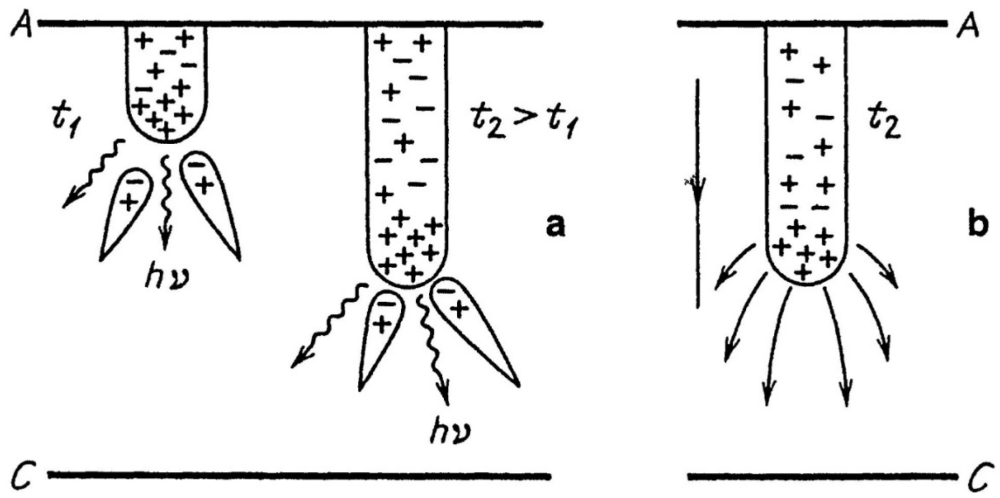


**Figure 2.4** Cathode-directed streamer: (a) Streamer at two consecutive moments of time, with secondary avalanches moving towards the positive head of the streamer, wavy arrows are photons that generate seed electrons for avalanches, (b) Electrical field line near the streamer head [11].

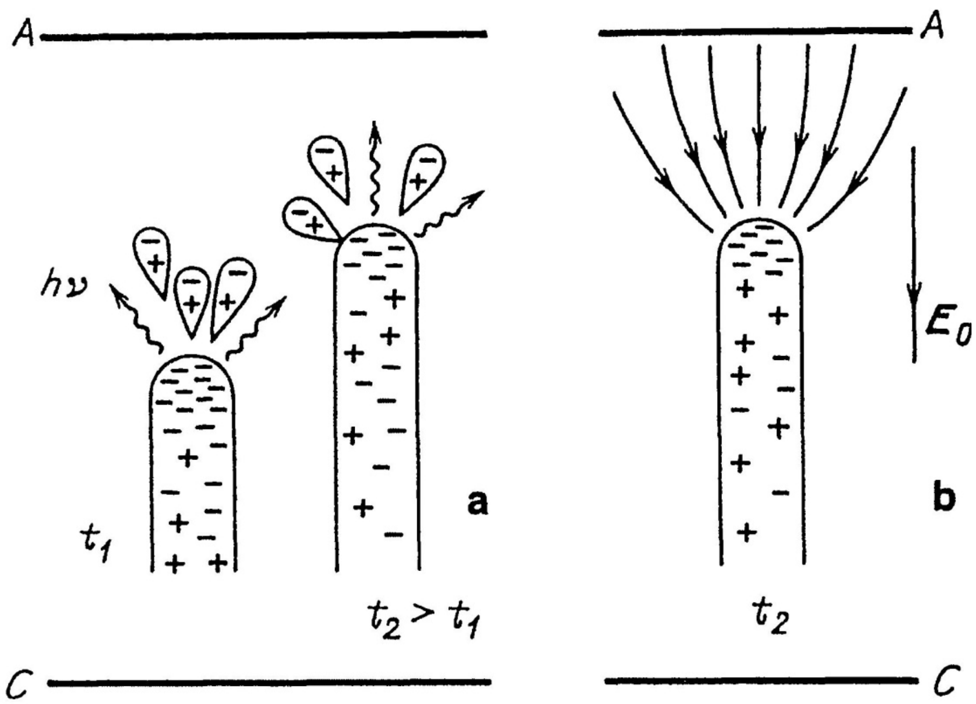


**Figure 2.5** Anode-directed streamer: (a) Photons and secondary avalanches in front of the streamer head at two consecutive moments of time, (b) Field in the vicinity of the head [11].

The electric field in one avalanche is

$$E_a = \frac{e}{4\pi\varepsilon_0 r_A^2} exp(\alpha x). \tag{2.7}$$

From above streamer occur when avalanche field is comparable to the external field so this relation can be written in the form:

$$E_a = \frac{e}{4\pi\varepsilon_0 r_A^2} exp(\alpha x) \approx E_0 \tag{2.8}$$

This can be regarded as the criterion of streamer formation [11, 12]. The gap width $x = d$ is minimal for given $E_0$. Taking avalanche head radius $r_A = 1/\alpha$ = 0.1 cm as ionization length so $\alpha d$ = 20 and $N_e = exp(\alpha d) \approx 3\times10^8$ [10, 11].

These conditions are important in formation of streamer which is known as *Meek's breakdown condition*. The concept of streamer was originally developed by Raether, Loeb, Meek and Craggs [11, 12] which the streamer acts as small needle connecting both electrodes. Photon also plays important role to initiate streamer that photon is emitted from excited or metastable atoms in avalanche vicinity causing photoionization. Electrons created from photons start a new avalanche that will be added into streamer and then new photons are emitted to begin electron avalanche again as shown in Figs. 2.4 and 2.5. This explains how streamer grows.

Another case is that $E$ is much higher and satisfy *Meek's breakdown condition* at $x < d$. The avalanche transforms to streamer between gaps but far away from cathode or anode and can grows to both anode or cathode.

### 2.2.4 Paschen's Law

The breakdown characteristics of a gap are a function of the product of the gas pressure and the gap distance, usually written as $V = f(\,pd\,)$ as shown in Fig. 2.6, where $p$ is the pressure and $d$ is the gap distance. To get the expression of *Paschen's curve*, substitute $\alpha$ into breakdown condition Eq. (2.6). Then, we get

$$V = \frac{B(pd)}{\ln(pd) + C} \tag{2.9}$$

where $$C = \ln A - \ln\left[\ln\left(\frac{1}{\gamma} + 1\right)\right]. \tag{2.10}$$

As seen in Fig. 2.6, each breakdown curves of gases (*Paschen's curve*) have a minimum breakdown voltage as shown in Table 2.2 that can be found from;

$$V_{min} = \frac{eB}{A}\ln\left(\frac{1}{\gamma} + 1\right) \tag{2.11}$$

**Table 2.2** Minimum breakdown voltage of gas that satisfy *Paschen' law* [16].

| Gas | $V_{min}$ (V) | *pd* at $V_{min}$ (torr.cm) | Gas | $V_{min}$ (V) | *pd* at $V_{min}$ (torr.cm) |
|---|---|---|---|---|---|
| **Air** | 327 | 0.567 | **$N_2$** | 251 | 0.67 |
| **Ar** | 137 | 0.9 | **$N_2O$** | 418 | 0.5 |
| **$H_2$** | 273 | 1.15 | **$O_2$** | 450 | 0.7 |
| **He** | 156 | 4.0 | **$SO_2$** | 457 | 0.33 |
| **$CO_2$** | 420 | 0.51 | **$H_2S$** | 414 | 0.6 |

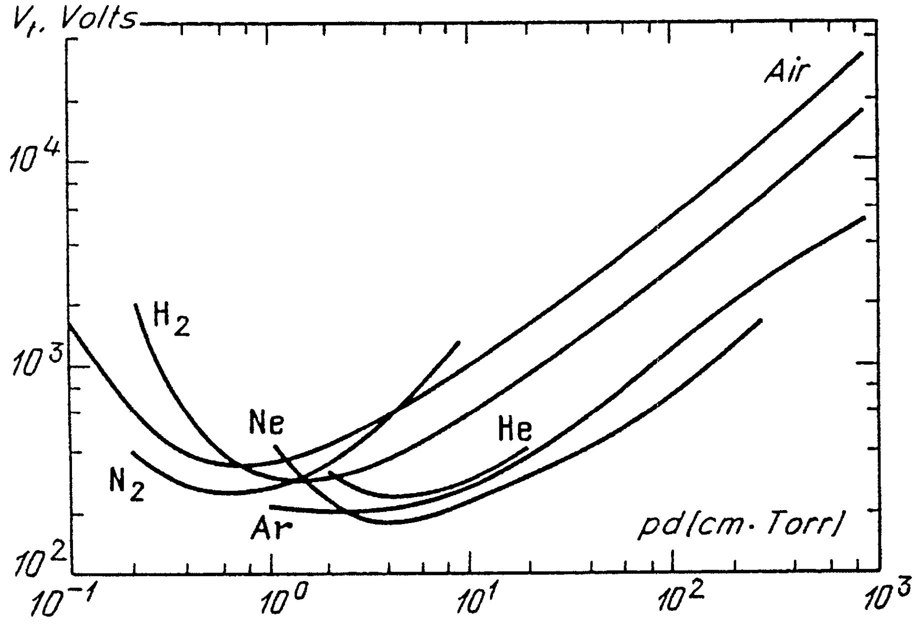


**Figure 2.6** Breakdown potentials in various gases over a wide range of *pd* values (*Paschen's curves*) on the basis of data given in Table 2.2 [11].

## 2.3 Gas Discharge under Various Frequency

Plasma can be generated by several methods not only electric field but also magnetic field, and electromagnetic field. However, stimulated by electric field is the easiest way to produce plasma with simple instruments. Next we will discuss about plasma generation under various frequency.

### 2.3.1 Direct Current (DC) Discharge

Plasma can be produced by applying DC voltage between cathode and anode. If the voltages across both electrodes satisfy $pd$ value in *Paschen's law*, gas starts to breakdown and plasma can be said ignited. This method mainly operates in vacuum condition to prevent glow to arc transition.

Parallel-plate configuration or a capacitively couple plasma mode is the most widely used for plasma operation. The potential distributions between its two parallel electrodes are shown in Fig. 2.7. The anode is at ground and the cathode is connected with negative voltage. Normally, application of DC plasma operation will be chosen in range of abnormal glow discharge as seen in Fig. 2.2. The bulk of the plasma floats above ground by the plasma potential, $\Delta V_p$ and has little voltage drop across it because of its high conductivity relative to that of the sheaths. The cathode has voltage of $V_0$. This voltage drop results in high-energy ion bombardment that causes secondary electron emission. And if positive ions bombarding cathode have enough energy, they will sputter or dislodge cathode atoms.

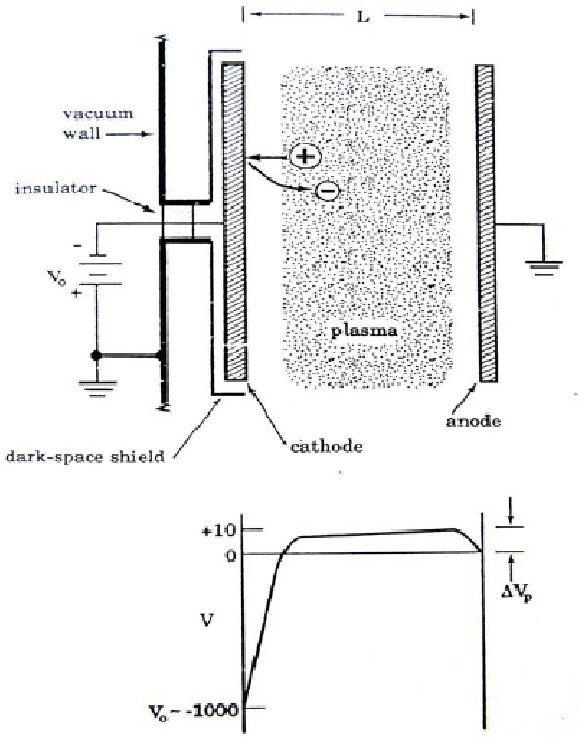


**Figure 2.7** Geometry and typical voltage profile of the parallel-plate DC glow discharge [1].

The mechanism of discharge is explained above by *Townsend mechanism* started from free electrons which gain energy from DC field to produce electron avalanche and many positive ions and so on. General application of DC discharge is to produce thin film by sputtering process. However, the disadvantage of DC discharge for sputtering is to produce dielectric thin film due to the insertion of dielectric material will cause the extinction of the discharge. To overcome this problem the AC or RF discharge is used [1].

### 2.3.2 Alternating Current (AC) Discharge

The AC discharge has the advantage above DC discharge because plasma can go on even though there is presence of insulating material between electrodes so power may pass through the insulator by capacitive coupling. However, AC discharge properties and mechanism at low frequency will be different from those at high frequency [11, 15, 17, 18].

Let's start from equation of motion of charged particle in uniform electric field

$$qE(t) - \psi mv = ma$$
$$m\frac{d^2x}{dt^2} + \psi m\frac{dx}{dt} = qE_0 sin(\omega t) \qquad 2.12$$

where $\psi$ is a rate of momentum loss due to collisions. Assume that the solution will be written in form $x(t) = Asin\omega t + Bcos\omega t$ and substitute it into Eq. (2.12), so we get

$$m\omega A - \psi mB = 0$$
$$-m\omega^2 B - \psi\omega mA = qE_0 \qquad 2.13$$

Then

$$A = \frac{\psi}{\omega}\left[\frac{-qE_0}{m\omega^2 + m\psi^2}\right]$$
$$B = \frac{-qE_0}{m\omega^2 + m\psi^2} \qquad 2.14$$

From solving all the equation above the solution can be rewritten in form $x(t) = x_0 \sin(\omega t + \delta)$ where $\delta = arctan\frac{\psi}{\omega}$, so the amplitude of charged particle moving in uniform electric field becomes

$$x_0 = \sqrt{A^2 + B^2} = \frac{qE_0}{m\omega\sqrt{\omega^2 + \psi^2}} \qquad 2.15$$

The useful parameter to characterize AC discharge is the oscillation amplitude limit which can be defined from Eq. (2.15). The oscillation amplitude limit is $x_0 = L/2$, where $L$ is the relevant chamber dimension. Beyond this limit ($x_0 > L/2$), charged particles or electrons will impact the chamber wall and be lost from the system. The breakdown voltage as a function of frequency is shown in Fig. 2.8.

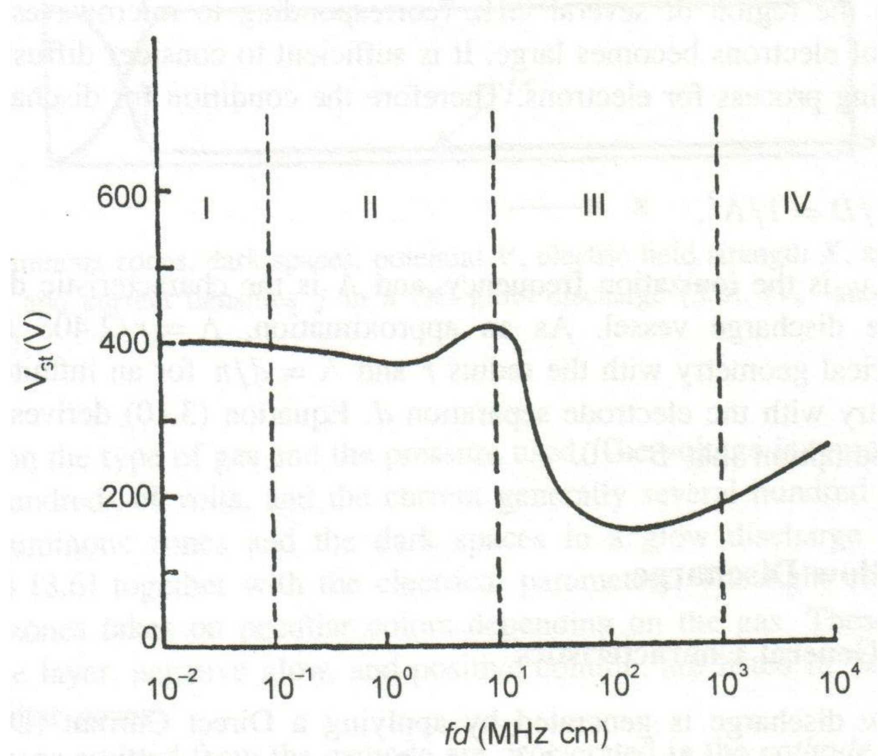


**Figure 2.8** Plot of breakdown voltage as a function of applied frequency [19].

At low frequency both electrons and ions can respond to the AC field. Secondary electrons, sustaining plasma, are produced by ion bombardment of the cathode (*Townsend mechanism*). The difference from DC plasma is that the cathode and anode alternate in each half cycle of the wave as shown in Fig. 2.9. So the breakdown voltage is not different from DC discharge.

As the frequency is increased, the ions responding to the AC field slowly ($x_i \ll L/2$) due to their mass while electron still responds almost instantaneously

$(x_e > L/2)$. So the ion current to the cathode sharply decreases and the electron loss becomes more severe then both ion bombardment and secondary electron production are reduced. This increases the breakdown field as the wavelength is reduced.

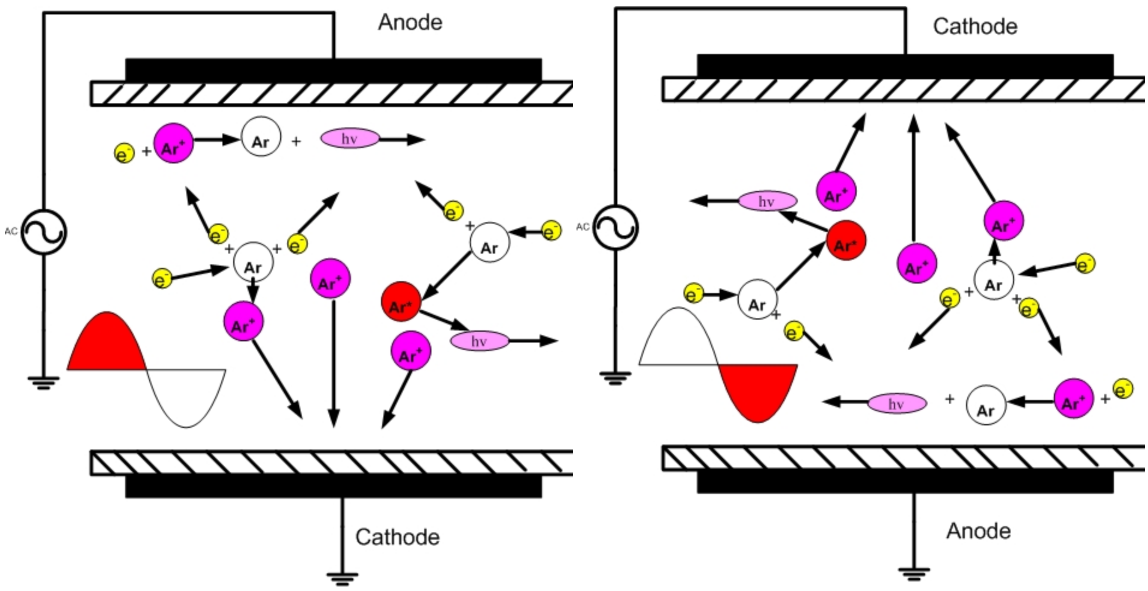


**Figure 2.9** Schematic of cathode and anode supplied by low frequency AC field which alternate periodically each half cycle.

As the frequency is raised further or in the other word, wavelength is reduced further, the oscillation of electron will go below the limit $(x_e < L/2)$. At this point, the heavy loss of electron will stop which causes the breakdown voltage drops by a large value as seen in Fig. 2.8. *Secondary electron emission* is no longer needed for sustaining plasma at this frequency range.

## 2.4 Dielectric Barrier Discharge (DBD)

### 2.4.1 DBD Overviews

Dielectric barrier discharges (DBD), also known as *silent discharges*, were invented by W. Siemens in 1857 for the purpose of ozonizing air [6, 7]. They are stable high pressure gas discharges capable of producing large densities of radical atomic and molecular species. Several typical DBD configurations are shown in Fig. 2.10.

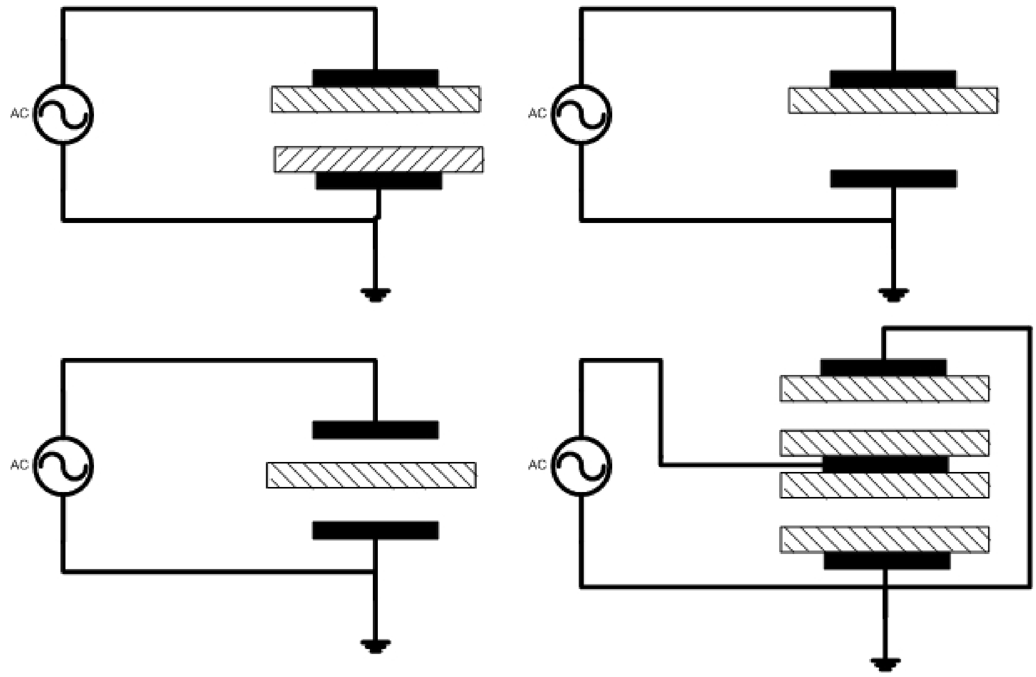


**Figure 2.10** Common dielectric barrier discharge configurations.

The dielectric material can be made from glass, quartz, epoxy, alumina or PTFE [15, 20-23]. General specifications of dielectric barrier materials are high heat strength, low dielectric loss and high breakdown strength. Some researchers suggest that dielectric material and their thickness affect plasma properties through *the secondary electron emission process* which occur at dielectric surface [21, 23, 24].

Due to the presence of the dielectric, DBDs cannot be operated as DC discharges. Typically, it requires AC driving frequency in range of 50 Hz to several MHz [6, 8, 11, 12, 15, 20, 25]. The DBDs of air consists of a number of independent transient filaments or microdischarges or streamers randomly distributed across the electrode surfaces. The filaments ignite when the breakdown field is reached and are extinguished due to electron attachment and recombination when the field falls slightly, due to space charge buildup, and the conductivity is reduced. Charge build up at the location of the filament on the dielectric terminates the microdischarge a few nanoseconds after breakdown. Fig. 2.11 shows the relationship between the formation time of microdischarges and the phase of an applied sinusoidal voltage.

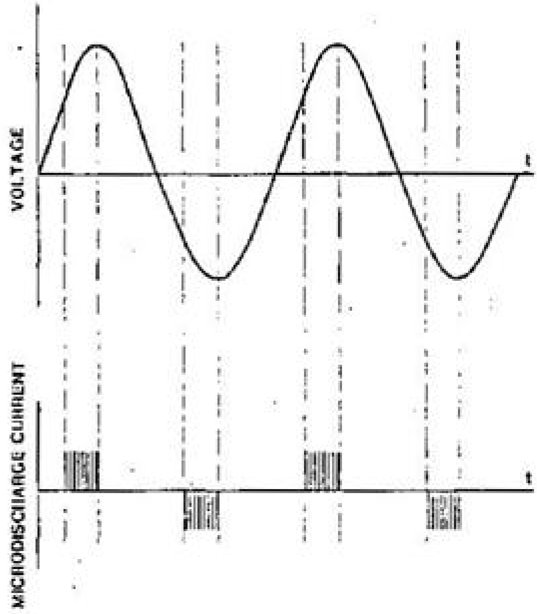


**Figure 2.11** Schematic diagram of bursts of microdischarges during application of sinusoidal voltage [26].

The microdischarge may be viewed from the point of streamer theory [11, 12]. The electrons in streamer is loss when reaching the anode while the ions remain for several microseconds. Deposition of electrons at anode (dielectric anode) resulting in charge accumulation that prevent a new avalanche. When the polarity reverses, the negative accumulation forces the new avalanche and then be the streamer at the same spot. At this point, a number of streamers occur that can be observed by naked eyes as a bright filament connecting either electrodes or dielectric barrier. The properties of filament are shown in Table 2.3. However, the meaning of filament and microdischarge are a bit difference. A microdischarge occurs after the avalanches reach anode and leave some of positive ions in the gap and when the polarity change the charge accumulation facilitates current or new microdischarges to flow through remaining ionic space charge at the same spot. Thus the filament is a bundle of microdischarge.

**Table 2.3** Typical parameters of a microdischarge [12].

| Lifetime | 1-20 ns | Filament radius | 50-100 μm |
|---|---|---|---|
| **Peak current** | 0.1 A | **Current density** | 0.1-1 $kAcm^{-2}$ |
| **Electron density** | $10^{14}$-$10^{15}$ $cm^{-3}$ | **Electron energy** | 1-10 eV |
| **Total dissipated energy** | 0.1-1 nC | **Gas temperature** | 300 K |
| **Total transported charge** | 5 μJ | **Overheating** | 5 K |

Typically, microdischarge formation not only depends on operating frequency but also gas composition, pressure, and electrode configuration. Increasing power will generate more microdischarges per unit time and area.

### 2.4.2 Homogenous Discharge

In recent decades atmospheric plasma has been developed, many plasma research laboratories can generate DBD plasma in homogeneous mode by using rare gases instead of air. However the full explanation of this mode is still yet to develop. The generation of atmospheric plasma in this mode is attractive to many applications which are not only surface treatment, thin films deposition but also other plasma processing because it has many advantages over filamentary mode such as operation at lower voltage without streamer or spark-relate phenomena, higher power density and etc.

Atmospheric pressure homogenous discharge is first developed by Okazaki *et al* using 50 Hz power source with mesh electrodes style [20] and further improved and theorized by many plasma research groups. According to J. R. Roth *et al* [15], the proper driving frequency should be chosen to generate homogenous plasma by considering equation of charged particle in electric field (see Section 2.3.2)

$$x(t) = x_0 sin(\omega t + \delta) \qquad 2.16$$

where $$x_0 = \frac{qE_0}{m\omega\sqrt{\omega^2 + \psi^2}} \qquad 2.17$$

where $\psi$ is charge collision frequency. The root mean square of displacement of charge motion during a half cycle is given by

$$x_{rms} = \sqrt{\frac{2}{T}\int_0^{T/2} [x_o sin(\omega t + \delta)]^2 dt}$$
$$x_{rms} = \frac{2eE_0}{\pi m\omega\sqrt{\omega^2 + \psi^2}} \qquad 2.18$$

For example, the collision frequency of argon and electron are $6.8\times10^{9}$ and $1.8\times10^{12}$ respectively which are much more than driving frequency (<1 MHz). So Eq. (2.17) can be reduced into $qE_0/m\omega\psi$. As discussed in Section 2.3.2, electrons or ions are lost from the system when $x_{rms} > d/2$. Then critical frequency $\upsilon_0$ is calculated from this relation;

$$\frac{d}{2} = \frac{qV_{rms}}{2\pi m\upsilon\psi d}$$
$$\upsilon_0 = \frac{qV_{rms}}{\pi m\psi d^2} \qquad 2.19$$

If the driven frequency is below the critical frequency then ions reach and heat up cathode resulting in filamentary formation. In range of the narrow band of frequency, ions oscillate between electrodes but electron still strike both electrodes, homogenous plasma can occur. If applied frequency is still higher so both ions and electrons are trapped causing filamentary discharge. To achieve homogenous discharge the operating frequency should lie between the limits as follow;

$$\frac{qV_{rms}}{\pi m_i \psi_i d^2} \leq \upsilon_0 \leq \frac{qV_{rms}}{\pi m_e \psi_e d^2} \qquad 2.20$$

where the upper limit is electron trapping frequency and the lower limit is ion trapping frequency. However, there are other factors involving with producing homogenous plasma such as gap width, pressure, dielectric thickness, gas combination and etc.

In fact the homogenous discharge mode can be classified into glow-like mode and Townsend-like mode [27-30]. High speed photographing reveals the different light distribution between two modes as shown in Fig. 2.12. The former mode has the same structure as glow discharge while the latter mode has a luminous layer near the anode that is the characteristic of Townsend discharge. Atmospheric helium plasma can ignite in glow-like mode but nitrogen plasma mostly ignites in a Townsend-like mode [27-30].

A study of optical emission spectra of helium and nitrogen by Massines *et al* reveals the role of metastable He and $N_2$ in their discharge [28]. The numerical simulation that had been done by this group [28] show that homogenous plasma in helium is maintained by *Penning ionization process* [31] with nitrogen impurity as follow;

$$He + e^- \Rightarrow He^* + e^-$$

$$He^*(2\ {}^3S) + N_2 \Rightarrow N_2^+(B^2\Sigma_u^+) + He + e^-$$

This process decreases the rate of ionization from electron avalanche that satisfy Meek criterion to avoid streamer formation. However, for $N_2$ metastable, the role of this specie in atmospheric nitrogen plasma is different. In $N_2$ Townsend-like plasma, the light is bright at the anode as seen in Fig. 2.12. The explanation is proposed by the same group that electron density is highest at anode that excite the metastable $N_2$ generation near anode then the light intensity is maximum at anode. The metastable $N_2$ cannot make *Penning ionization* in $N_2$ but can induce the secondary electron emission from dielectric surface to sustain the plasma when the voltage polarity is reverse [28, 29]. However, this discharge has not enough ionization level so it cannot transit to glow region.

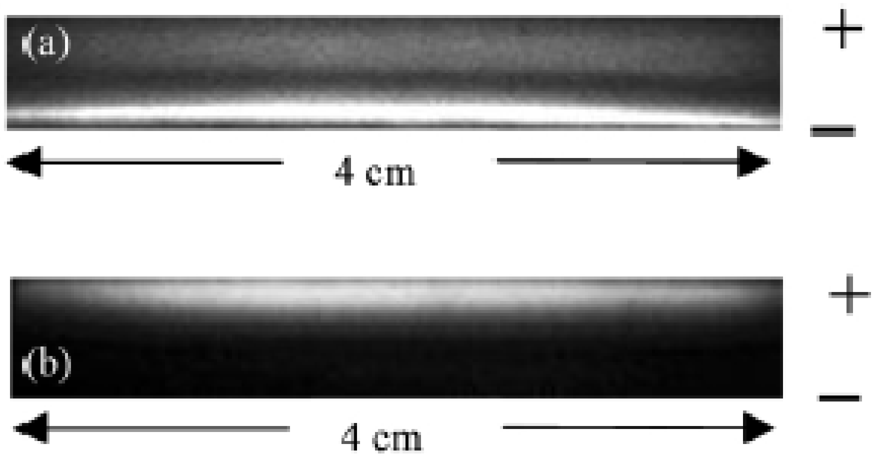


**Figure 2.12** Ten nanosecond exposure time photographs of the homogenous discharge in (a) He (b) $N_2$ [28].

## 2.5 Surface Modification

Several decades ago atmospheric plasma by dielectric barrier discharge technique is widely used for generating ozone as shown in Fig. 2.13. To produce this gas the uniformity of plasma was ignored so mostly it was operated in filamentary mode. In 1990s Okazaki *et al* [20] were able to generate the uniform atmospheric plasma by DBDs technique and still develop by many research groups till the present.

To modify surface properties it is important that the plasma has to have uniformity of effect to avoid local damage and heating which lead to the destruction of workpiece. So the homogenous plasma can solve this problem and give more advantages over original low pressure plasma treatment in large area operation.

### 2.5.1 Type of Modification

- ***Ablation***; the ability of plasma to break material bond at surface by high energy particle bombardment.
- ***Cross-linking***; Plasma with inert gas can be used to create chemical link between long molecular chains that produce a stronger and harder surface.
- ***Activation***; Plasma radical species, such as, OH, O, $NH_2$ and etc depending on process gas, can replace surface functional group that change the surface energy.

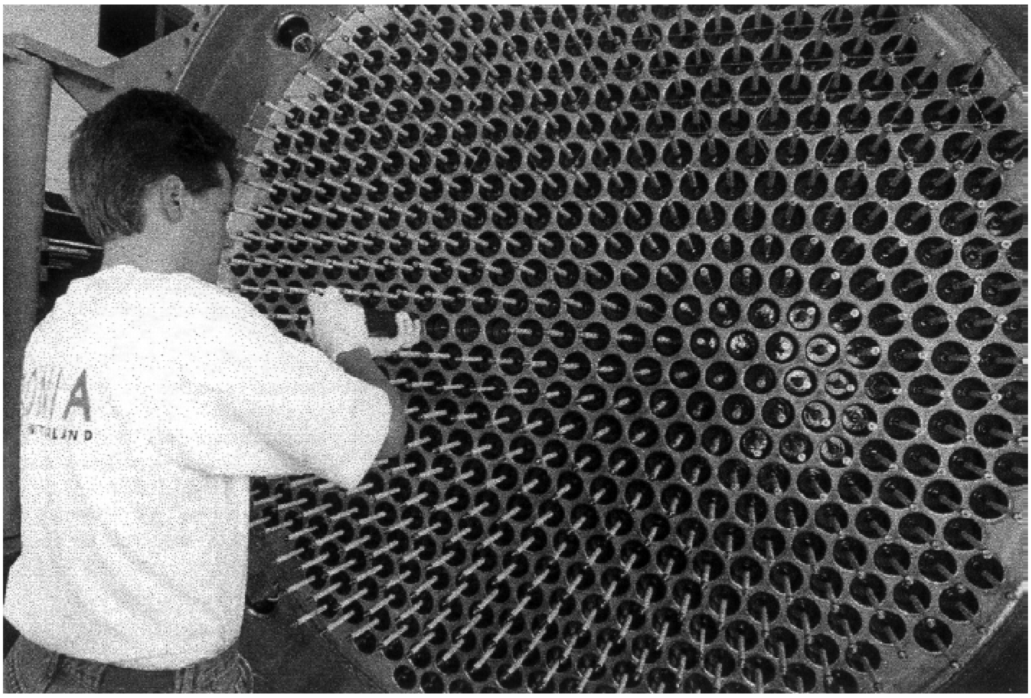

**Figure 2.13** Advanced ozone generator producing 60 kg/h with non-glass dielectrics [6].

### 2.5.2 Applications

#### a) Plasma Cleaning

One such alternative method for organic removal is plasma cleaning. Nowadays, plasma cleaning is very useful and popular dry cleaning process. Many applications, mostly semiconductor and thin film, employ plasma to clean substrate surface [9, 32-38], as the last step of surface preparation technique. The organic contaminant and some weak chemical bond are removed from the surface. Typically, oxygen-containing plasma is selected to clean surface. For pure oxygen, first, electron collides $O_2$ to breaks into two oxygen atoms following this process;

$$e + O_2 \Rightarrow e + O_2(A^3\Sigma_u^+) \Rightarrow e + O(\,^3P) + O(\,^3P)$$

$$\Rightarrow e + O_2(B^3\Sigma_u^-) \Rightarrow e + O(\,^3P) + O(\,^1D)$$

with energy thresholds of 6.0 eV and 8.4 eV respectively. The oxygen radicals are very reactive then they can react with hydrocarbon to form $H_2O$ or $CO_2$. Ozone can be also formed as well. Due to ozone is an active gas so it can break hydrocarbon chain very rapidly.

#### b) Adhesion Improvement

Some of polymer materials such as polypropylene, polyethylene, PTFE and etc, have low surface energy. This character makes it difficult to apply adhesive or coating on their surface. By using oxygen or oxygen-containing plasma producing some radical species such as O and OH that will replace surface functional group or chemically react with surface atom as shown in Fig. 2.14, so surface energy will increase [39-42]. A higher surface energy provides better water wetting and greater chemical reaction.

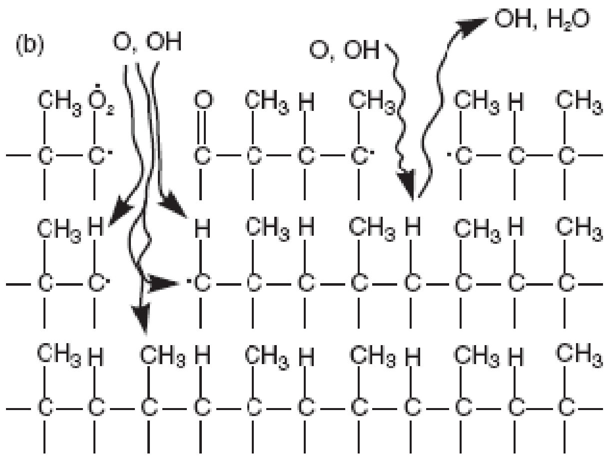

**Figure 2.14** Surface reaction mechanisms in PP [39].

### c) Hydrophilic and Hydrophobic properties

The relationship between contact angle and surface energy is inverse, the contact angle reduce with increasing surface energy. Rare gases and also oxygen-containing plasma can be used to increase hydrophilic property that these plasmas generate some radical or change surface molecular weight, thus increasing surface energy [39-42]. However, process gases such as fluorocarbon and fluorosulfur provide lower surface energy or hydrophobic property by replacing the abstracted hydrogen with either F or $CF_3$ radicals to form a fluorocarbon surface called fluorination process [43]. This application can be found in textile industries and medical applications.

# CHAPTER III
# EXPERIMENTAL SETUP

## 3.1 High Voltage Medium Frequency Power Supply

### 3.1.1 Power Supply Requirements

Atmospheric plasma gains its energy from a power supply, preferably AC or RF one [6, 8, 11, 12, 15, 20, 25], because it is difficult to stabilize plasma in non-thermal region by DC electric field. Requirements to generate atmospheric plasma by dielectric barrier discharge technique have already been mentioned in the previous chapter so the power supply should have these properties;

#### a) AC High Voltage Generation

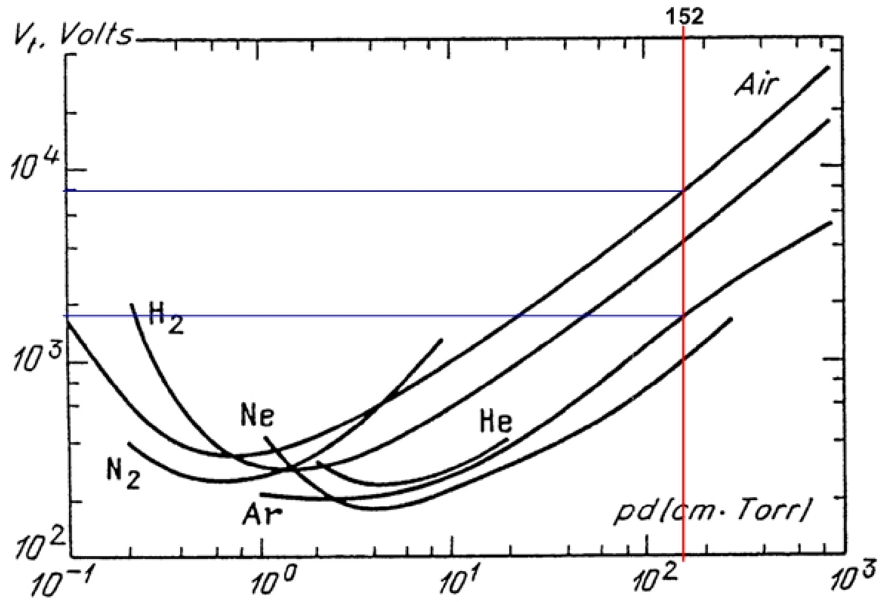


**Figure 3.1** The breakdown voltage of argon and air at $pd$ $= 152$ Torr.cm.

At low to medium frequency, of the order of several kHz, the AC breakdown voltage of each gases are slightly different from DC breakdown voltage

[11]. Consider the *Paschen's curve* in Fig. 2.6. To ignite argon and air in 2 mm gas gap at atmospheric pressure ($pd$ = 760×0.2 = 152), the power supply has to raise DC voltage to be approximately 1.8 kV and 8 kV respectively as seen in Fig. 3.1 where the vertical line represents $pd$ = 152 Torr.cm and the horizontal lines represent breakdown voltage.

#### b) Input Power Range and Control

Plasma power and ion density can be controlled by changing input power. The operating power depends on the applications, purposes, electrode size and gas.

#### c) Ground Isolation

A power supply must deliver very high voltage. Ground isolation is indeed very important to prevent damage to the power supply and user in case of malfunction.

In the present day, technology in solid state components is rather well developed; MOSFET, IGBT and also integrated circuit, can readily meet these demanding requirements.

### 3.1.2 The First Prototype

From fundamental physics of electrical resonant of *RLC* circuit, the voltage across capacitor is very high. Assume that driving voltage is ideal square wave [44] then a Fourier series of square wave can be written in form;

$$V(t) = \frac{4V_p}{\pi}\left[sin\omega t + \frac{sin3\omega t}{3} + \frac{sin5\omega t}{5} + \frac{sin7\omega t}{7} + \cdots\right] \quad 3.1$$

where $V_p$ is the peak voltage. From fundamental physics that the electric resonant frequency of *RLC* circuit is $f = 1/2\pi\sqrt{LC}$. At the resonant frequency, the *RLC* circuit allowed only fundamental frequency of square wave to pass through circuit. This technique is readily employed in radio or television tuner. Let $V_c$ is the peak voltage across capacitor and $I_p$ is the peak current of series circuit as follow;

$$V_c = I_p X_c = \frac{I_p}{\omega_0 C}$$
$$I_p = \frac{4V_p}{\pi R} \qquad 3.2$$

Then the voltage across capacitor can be calculated by

$$V_c = \frac{4V_p}{\pi \omega_0 RC} \qquad 3.3$$

However, this configuration has some drawbacks; e.g., step up transformer and ferrite cores of 0.14 Henry inductors become hot and then varnish oil melt because of high circulating energy in *LC* circuit when plasma is not ignited. This diagram is called series resonance with parallel load which plasma chamber acts as variable impedance (See Fig. 3.2) [27-29, 45, 46].

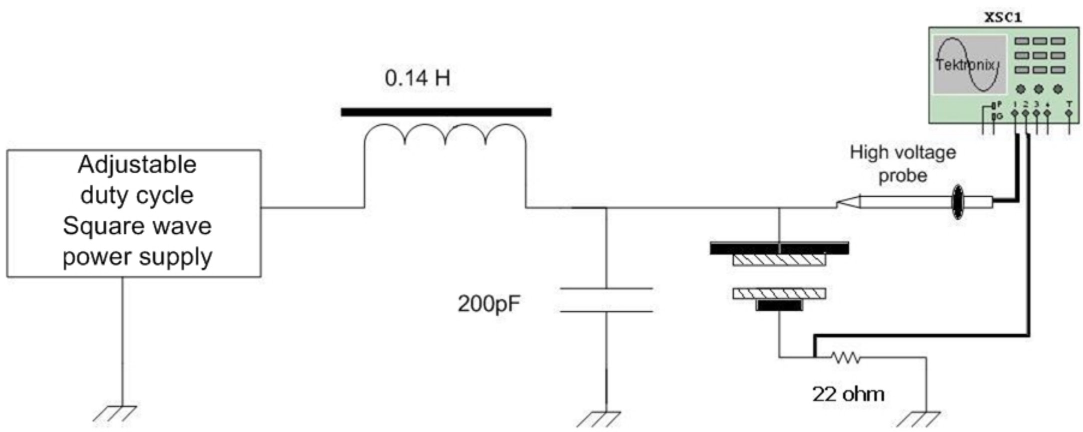


**Figure 3.2** The first experimental setup.

The operating frequency of power supply is near a resonant frequency which generates high voltage across 200 pF capacitor as calculated from Eq. (3.3) and removes high harmonic of square wave. The output voltage is controlled by varying duty cycle of square wave. Out of this frequency the voltage across this capacitor becomes low and is not sinusoidal. Unfortunately, plasma acts as variable impedance which always changes resonance frequency. Since the load is parallel connected, even at no load or light load conditions (before plasma ignites), the power source will see a very small impedance at resonance frequency [45, 46] which the power source has to supply a large amount of energy to generate high voltage. The output voltage of this topology depends on capacitance of a system and series inductor which the latter part has to be custom made. The aim of this power supply is to operate at low frequency (<30 kHz). A very large inductor of several hundred mH or more is necessary to couple with the capacitance of about 40-50 pF from the plasma chamber. If an external capacitor were used instead, the total capacitance is increased; an adverse effect on lower output voltage and higher circulating current is expected.

### 3.1.3 High Voltage Medium Frequency Power Supply Design

Fig. 3.3 shows diagram that generate high voltage at 17 kHz. It consists of four main parts which are 1) Isolation transformer with bridge diode and filter 2) Power controller (variable DC power supply) 3) DC–AC inverter and 4) Step-up transformer. The first and the second parts may actually be replaced by a conventional variac at the expense of heavy weight and large size, it is thus difficult to add all component into a single box and the protection by fuse alone cannot prevent the damage of other parts from overload.

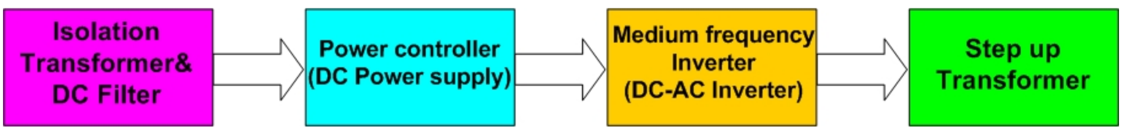


**Figure 3.3** The diagram of high voltage medium frequency power supply.

#### a) Power Controller (DC Power Supply)

The diagram in Fig. 3.4 shows important parts of power controller which the controller generates a couple of square wave signals which are buffered by the gate driver to drive H-bridge converter. The 220 VAC main line is step down to 90 VAC by isolation transformer and then filter AC voltage into 130 VDC by bridge diode and capacitor. A full bridge or H-bridge converter switches at frequency of 60 kHz that converts 130 VDC into 260 $V_{p\text{-}p}$ with 0-47% duty cycle of square wave and drives the voltage to 1:1 high frequency transformer. Then transformer output is filtered by Butterworth $\pi$ low pass filter into variable DC voltage. The output voltage can be calculated following Eq. (3.4). The output voltage is used to supply load or inverter. Feedback circuit senses output DC current and sends signal back to controller to reduce or increase duty cycle.

$$V_{out} = \left(\frac{N_s}{N_p}\right) \times D \times 2V_{in} \qquad 3.4$$

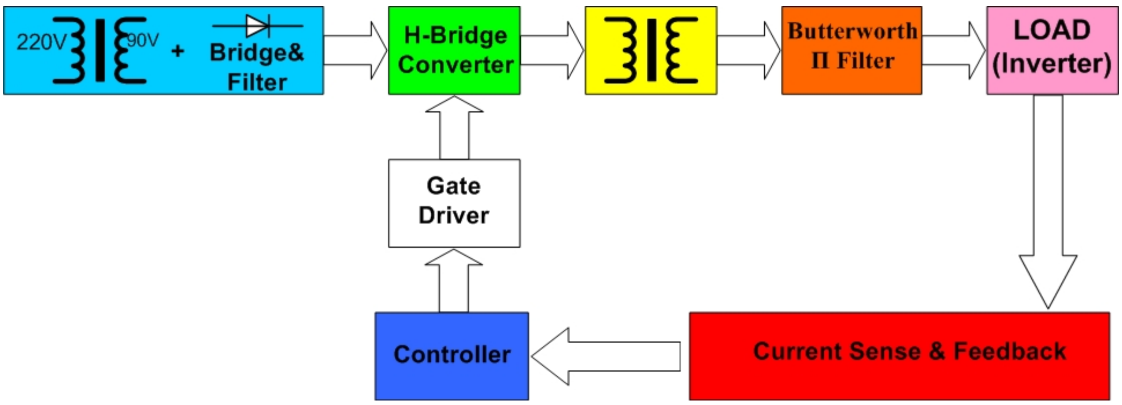


**Figure 3.4** Block diagram of power controller in a DC power supply.

**Controller**

IC TL494 is widely used in many types of commercial switching power supply and has many useful build-in functions integrated in this IC so this IC is chosen due to its relatively low price and its availability locally.

TL494 is fed with 12 V regulated from IC 7812 and generates two square wave signals at pin 9 and 10 which can be parallel or push-pull style depending on the input at pin 14 as shown in Table 3.1. In this power supply the push-pull style is chosen. The frequency of oscillator is programmed by the selection of timing components which are capacitor and resistor connected at pin 5 and 6 respectively. For push-pull operation, the frequency is defined by this equation;

$$f = \frac{1}{2R_T C_T} \tag{3.5}$$

**Table 3.1** Output function of TL494.

| **Input to Output Control** | **Output Function** |
|---|---|
| **$V_i$ = GND** | Single-ended or parallel output |
| **$V_i = V_{ref}$** | Normal push-pull operation |

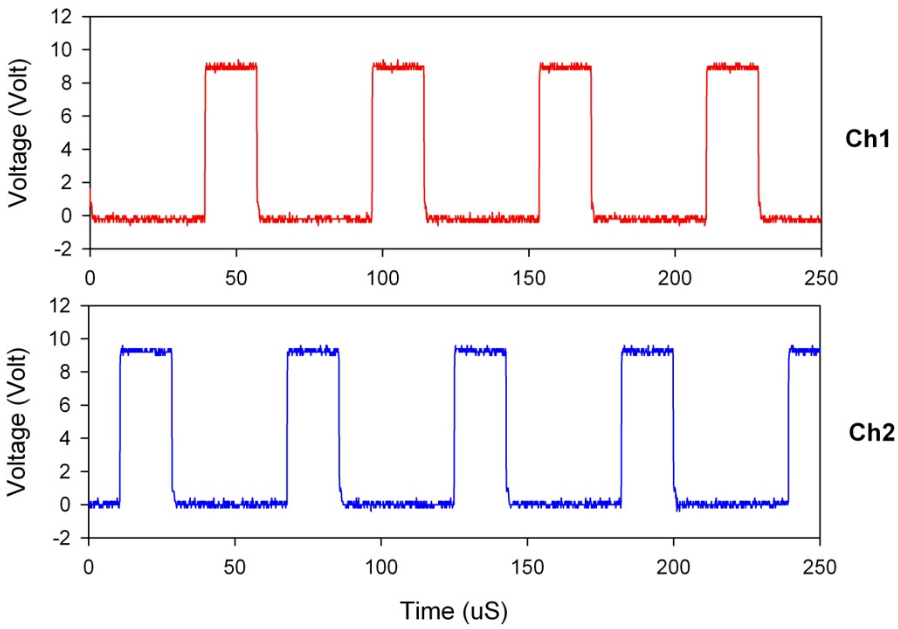


**Figure 3.5** Output signal at pin 9 (top) and 10 (bottom) of TL494.

The square wave generator circuit is shown in Fig. A1 (see Appendix A). By fixing capacitor at 10 nF, the frequency can be adjusted by varying resistor 20 kΩ and tuned to be 60 kHz. Signals from pin 9 and 10 are shown in Fig. 3.5. They are fed to a gate drive circuit as input signals.

## Gate Driver

The gate driver circuit consists of a couple of TC4427 which each IC is a buffer of each signal, gate drive transformer or pulse transformer driven by signal from both TC4427, and four isolated channels for driving full bridge converter. The input signals from TL494 is fed into IC TC4427 supplied by 12 V from LM317T which can drive high peak current up to 1.5 Amp. Pulse transformer is custom made by wiring a copper wire for 16 turns around toroidal ferrite core as a primary winding and wiring four copper wires for 24 turns as a secondary winding. The advantages of using pulse transformer to drive MOSFET are not only galvanic isolation between controller and power section but also able to drive several MOSFET by one pulse transformer [47]. Toroidal transformer is chosen to minimize the leakage inductance [47]. Other shapes of transformer can also be used at the expense of more leakage inductance which consequently make the signal delay and decrease the rise time of square wave [47]. Fig. 3.6 shows signal at a primary winding and secondary winding of pulse transformer. Because pulse transformer is wiring with turn ratio of 1:1.5 so the expected output voltage will be 18 V. Typically, the recommend voltage to drive MOSFET is about 10-15 V and Gate-Source legs has absolute maximum rating at ±20 V then to ensure that the driven voltage will not exceed maximum rating, it is limited by 1N4742 zener diodes which cut the any exceed and spike voltage. The 2N2907A PNP transistors Q1, Q6, Q7 and Q10 in Fig. A2 are used to increase turn off speed of MOSFET [47] to make sure that MOSFET in each legs of full bridge converter will not turn on at the same time that lead to the destruction of the converter and gate drive circuit.

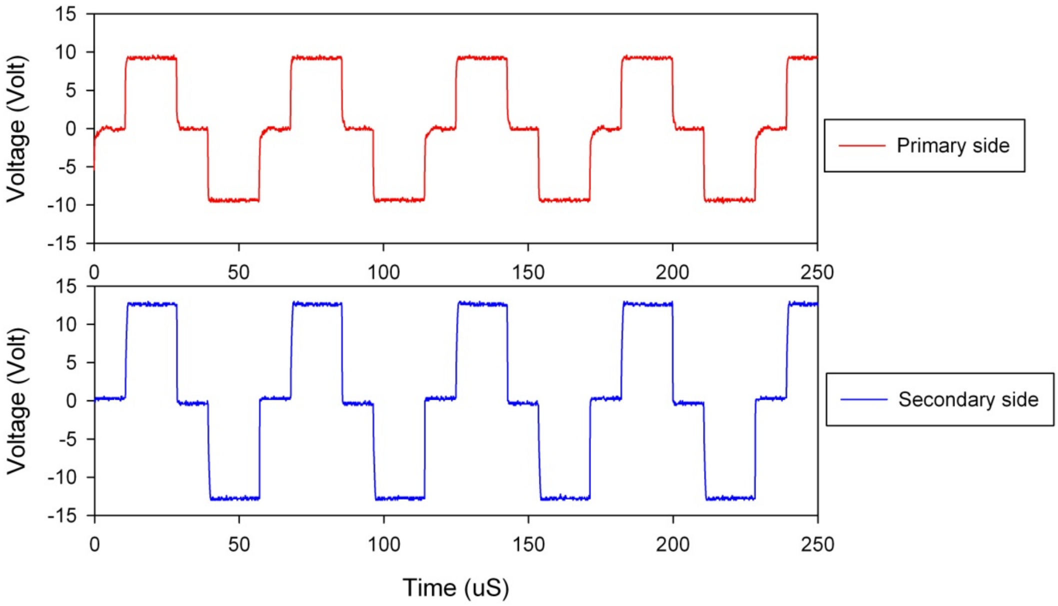


**Figure 3.6** Signals at primary winding (top) and secondary winding (bottom) of gate drive transformer.

**Full Bridge Converter**

The configuration of full bridge converter is shown in Fig. A2, consisting of four electronic switches, and supplied by 130 VDC. To drive the full bridge converter, four isolated channels driver are necessary. IRFP460 MOSFET is chosen. Its absolute maximum rating is shown in Fig. B1.

IRFP460 has a very high breakdown voltage so it can tolerate spike voltage from hard switching which can be 2-3 times supply voltage without using snubber. An internal diode is made to connect anti-parallel between Source and Drain legs [47]. This diode provides the free wheel diode function. Unfortunately, for operating at high frequency this diode has long reverse recovery time which limits the frequency of operation [47]. External fast recovery diode has to be anti-parallel connected with MOSFET to provide the necessary path to reverse current from inductive path [45-47].

As shown in Fig. A2, Q3 and Q9 conduct current for half cycle during which Q4 and Q8 are off. Next half cycle Q4 and Q8 will are on while Q3 and Q9 are off. So the voltage across load or transformer will be alternate square wave at switching frequency of 60 kHz. The 2N2222 NPN transistor Q2 and Q5 are used to limit the maximum current that provide short circuit protection in each bridge legs and give time to a fuse to blow to open circuit. The maximum current in each legs are defined by;

$$I_{max} = \frac{V_{BEsat}}{R_{SENSE}} \tag{3.6}$$

If the voltage across R5 and R6 (0.1 Ω) are 0.65 V which means current will be 6.50 Amp, the Q1 and Q6 begin to turn on and then reduce the duty cycle.

The transformer is wired onto a ETD-49 ferrite core, with an effective area core of 221 mm$^2$ and with 1:1 turn ratio. To reduce core loss and avoid core saturation, the minimum turn is required for primary winding [48, 49]. The minimum turn can be derived from Faraday's law as following [48, 49];

$$\begin{aligned}
|E| &= \left|-N\frac{d\Phi_B}{dt}\right| \\
E &= NA\frac{dB}{dt} = NA\frac{2B}{T/2} \\
N &= \frac{E}{4A_cB_Mf} \\
N &= \frac{130}{4 \times 221 \times 10^{-6} \times 0.2 \times 60{,}000} \\
&= 12.84 \approx 13
\end{aligned} \tag{3.7}$$

Typically, ferrite core has a saturation flux density around 0.2-0.4 Tesla, to avoid core saturation $B_M$ must not exceed maximum flux density [48, 49]. Assuming the maximum flux density of ferrite core is 0.2 Tesla and driven voltage is 130 V, the primary winding must be at least 13 turns to operate at 60 kHz. In practice, the primary winding is wired for 20 turns and also the secondary winding. At the secondary winding the square wave voltage is filtered by high speed recovery bridge diode and Butterworth $\pi$ network where $LC$ components are arranged in a $\pi$ shape as shown in Fig. 3.7. The variable DC voltage output will be fed though DC-AC inverter which converts DC voltage into 17 kHz sinusoidal voltage.

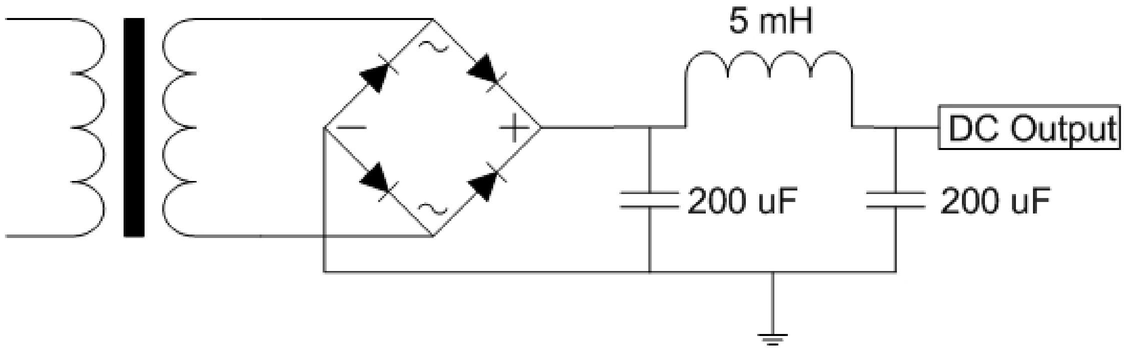


**Figure 3.7** Butterworth $\pi$ low pass filter.

**Feedback Controller**

The power delivered to plasma is controlled by detecting DC current, converted to be the feedback control signal, and send back to TL494 to increase or reduce duty cycle. HCPL7840, an opto-isolated operational amplifier with fix gain at 8, is used to provide galvanic isolation between output section and the controller. DC current is sensed by 0.1 ohm resister and HCPL7840 amplify the signal, and the differential outputs of the isolation amplifiers is buffered to 0-5 V which corresponds to DC current 0.0-1.2 Amp. Then the signal is fed to differential amplifier to compare with variable reference voltage (Set point) which is used to control power. The output from differential amplifier is added with 2.5 V and sent back to TL494 at pin 3. If current is higher than the set point, the signal goes high, reducing duty cycle. If the current is lower, the opposite operation is performed. Because plasma impedance is not constant, the current control ensures the safety operation by not allowing current to exceed the setting value. Or else substrate and also dielectric barrier are damaged. The circuit of feedback controller is shown in Fig. A3. However, feedback circuit is not included in PCB due to it is developed after power control problem was observed. This problem is the impedance of plasma decrease under long operating time due to dielectric barrier are heat up which lead to higher thermionic electrons emission and consequently to the destruction of the dielectric barriers.

#### b) Medium Frequency Inverter (DC-AC Inverter)

The block diagram of a medium frequency inverter is shown in Fig. 3.8. The square wave generator generates a couple of 17 kHz square wave signals which is just above audible noise from electronic switching and then are buffered by gate driver to drive H-bridge converter. This inverter gets DC voltage from the power controller and converts DC voltage into AC square wave signal at 17 kHz. Then 2.4 mH inductor is added to filter out other higher harmonic except first harmonic by means of resonant circuit [50-52]. The remaining signal is fed to step up transformer and the secondary output is connected with blocking capacitor and plasma chamber.

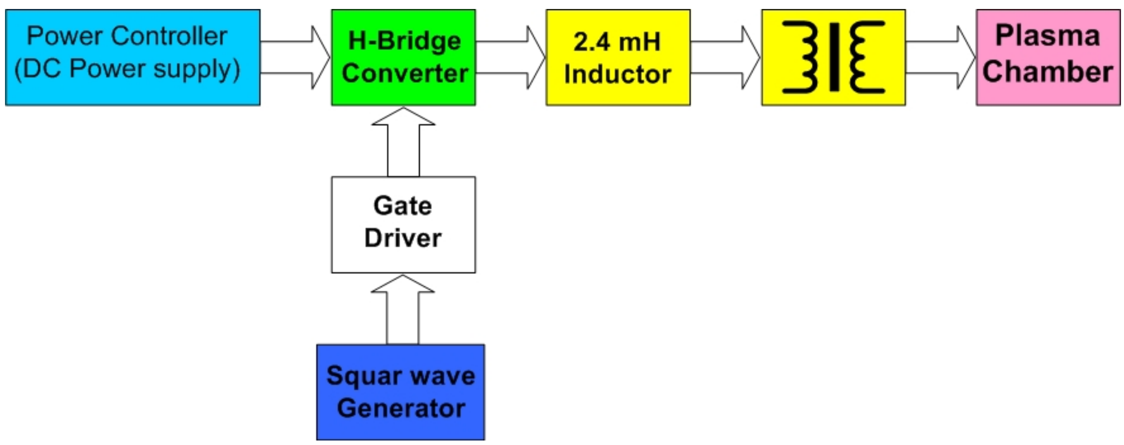


**Figure 3.8** Block diagram of medium frequency inverter.

A construction of this inverter has the same circuit as power controller circuit with variable frequency by resistor connected at pin 6 of TL494 but with the duty cycle fixed at maximum. The output of inverter at load of 50 Ω is shown in Fig. 3.9. The waveform is not perfect square wave but rather has two dead time regions in one cycle.

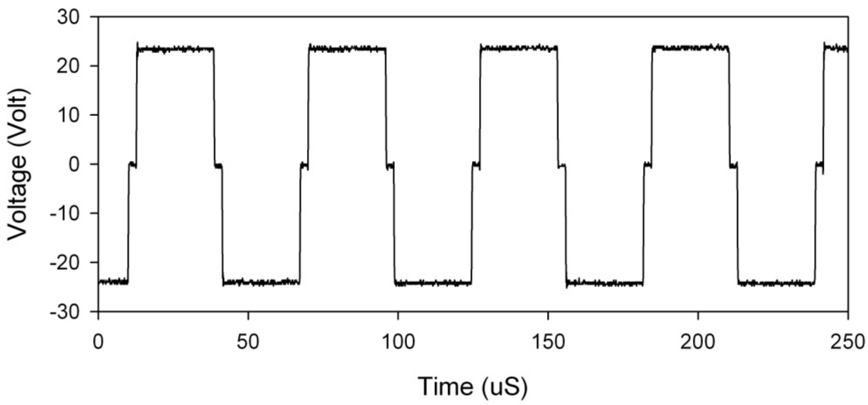


**Figure 3.9** The signal across 50 Ω load fixed at 17 kHz and maximum duty cycle.

### c) Step up Transformer

A compromise has to be made when operating at both high voltage and high frequency. Dielectric breakdown can be occurred in high voltage operation. To prevent this requires a very good insulation between primary and secondary winding. Then UU core can solve the insulation problem that provides very high insulation between each leg. High frequency operation requires a proper material for the transformer core, which in our case, is a ferrite core and tight winding [49, 53].

The winding design is limited by two main constraints as said in power controller part, namely;

1. The magnetic flux density must not exceed core saturation value.
2. Core loss must be minimized to avoid excessive temperature rise.

These mean the minimum primary turn is required and the transformer core must be pre-determined for suitable operation. However, instead of calculating the characteristic of required core, the largest available core is purchased so its properties are verified. The UU 93/152/30 ferrite core from EPCOS is selected and its characteristic is shown in Fig. B2. The minimum turns of primary winding is;

$$N = \frac{E}{4A_cB_Mf}$$

$$N = \frac{130}{4 \times 840 \times 10^{-6} \times 0.2 \times 17{,}000} = 11.38 \approx 12 \qquad 3.8$$

However, the primary winding is wired for 20 turns to increase the input voltage beyond 130 V. To reach the output voltage of 2.5 kV without resonant effect then the secondary winding can be calculated.

$$N_2 = N_1 \frac{V_2}{V_1}$$

$$= 20 \times \frac{2500}{130} = 384.6\, turns \qquad 3.9$$

In practice, the secondary winding has to be wired in single layer to avoid inter-winding corona discharge and is wired for 400 turns to compensate the ratio loss. As usable core window winding length is about 88 mm so the suitable diameter of wire must not exceed

$$d = \frac{88}{400}$$

$$= 0.22\, mm \qquad 3.10$$

Copper wire AWG 32 or 33 with respective diameter of 0.202 and 0.180 mm were chosen to wire a single layer of a secondary winding. Transformer bobbins are used for wiring the copper wire on the both primary and secondary side. Both bobbins are made from acrylic with 3 mm thick to prevent the breakdown between the core and the copper wire as shown in Fig. 3.10. Fig. 3.11 shows the schematic of wiring secondary winding.

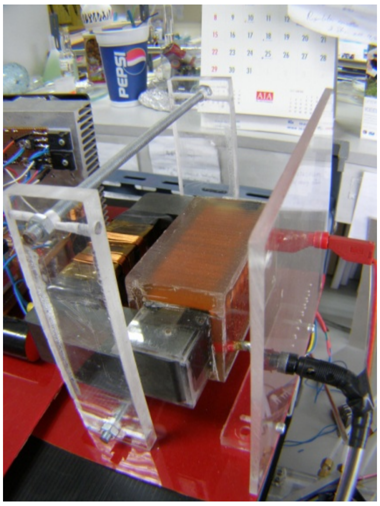

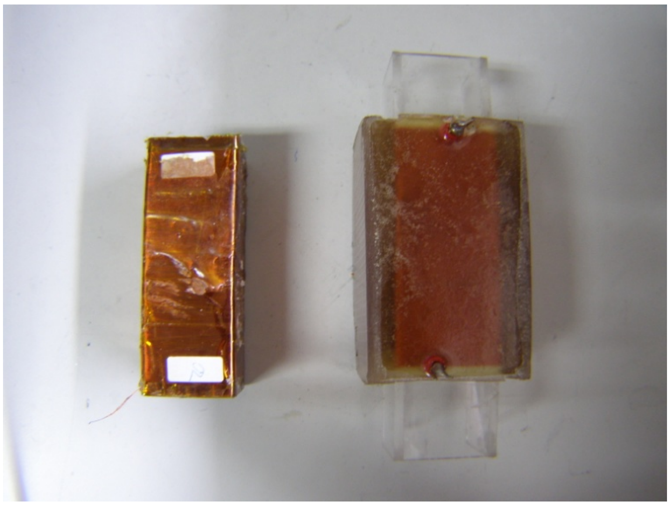

**Figure 3.10** Secondary winding of step up transformer including with acrylic bobbin which is covered by transformer-grade epoxy resin.

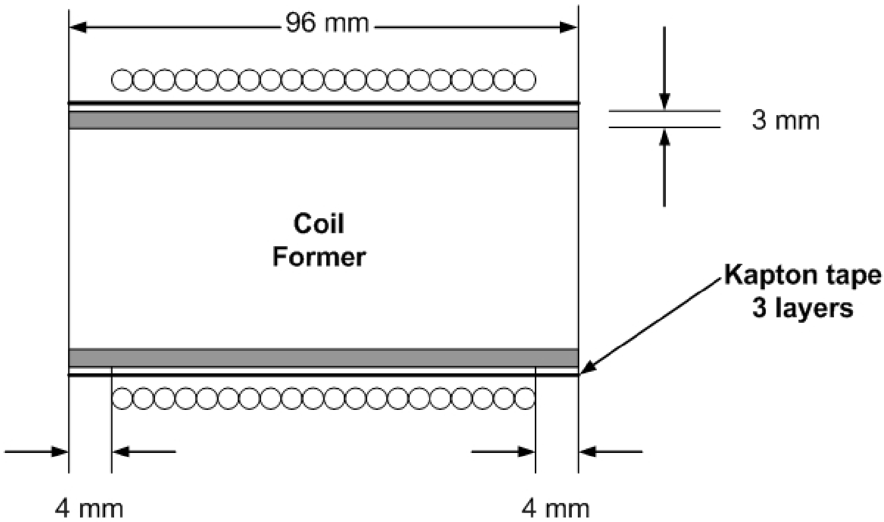


**Figure 3.11** Schematic of wiring secondary winding of step up transformer.

The transformer-grade epoxy resin is used to cover all air-contact part for secondary winding (see Fig. 3.10) to prevent corona breakdown at the surface of conductor otherwise, heat, which is dissipating, can cause destruction of the secondary winding under a high power operation. The important parameters of step up transformer are measured and shown in Table 3.2

**Table 3.2** Measured parameters of step up transformer.

| Parameters | Value |
|---|---|
| **Primary leakage inductance** | 432 µH |
| **Secondary leakage inductance** | 128 mH |
| **Winding stray capacitance** | 30 pF |
| **Magnetizing inductance** | 3.74 mH |

The equivalent circuit of this topology including the step up transformer and the plasma chamber is shown in Fig. 3.12.

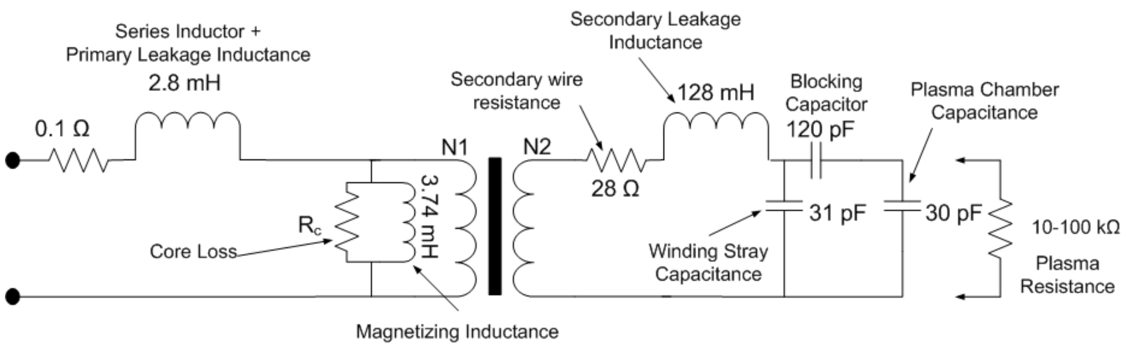


**Figure 3.12** The DBDs equivalent circuit.

The circuit in Fig. 3.12 is simulated by using MICROSIM with real parameters measuring from every components to predict how the power supply operate and improve the circuit with adding proper value of components. The plasma resistance is approximately 10-100 kΩ calculated from reflecting load to DC power supply. The core loss is negligible [45, 46]. The circuit prior to the discharge, shown in Fig. 3.13, is used for simulating; the result is shown in Fig. 3.14. The circuit, during the ignition process is shown in Fig. 3.15; the result is shown in Fig. 3.16.

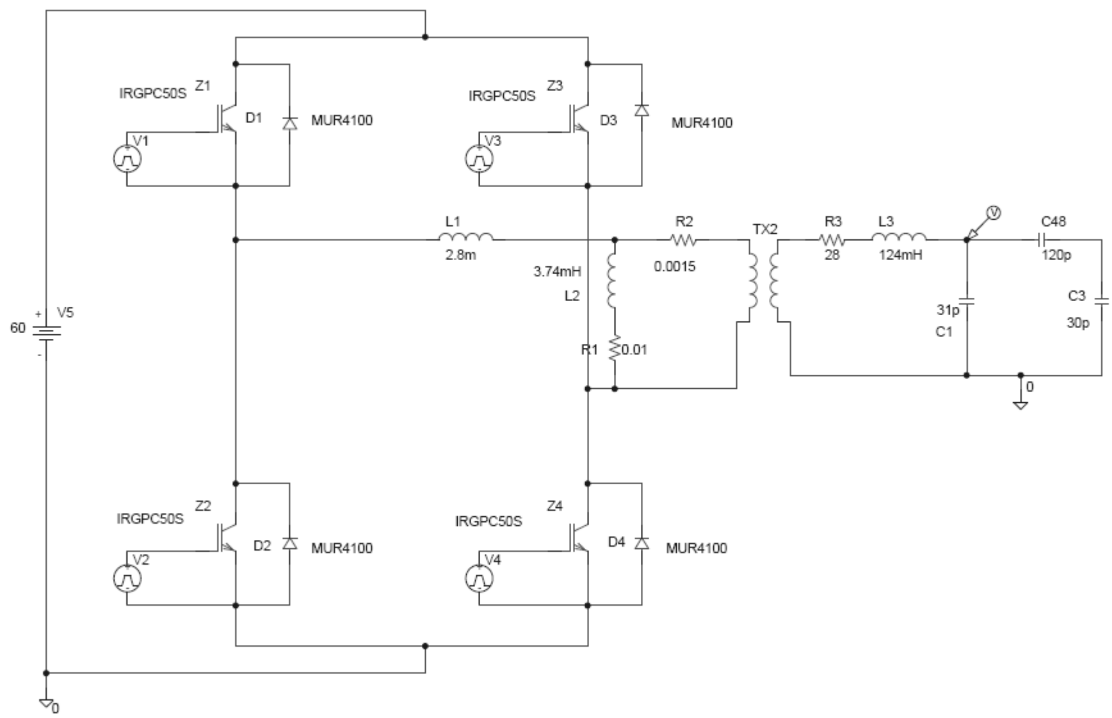


**Figure 3.13** Schematic of simulation circuit before discharge.

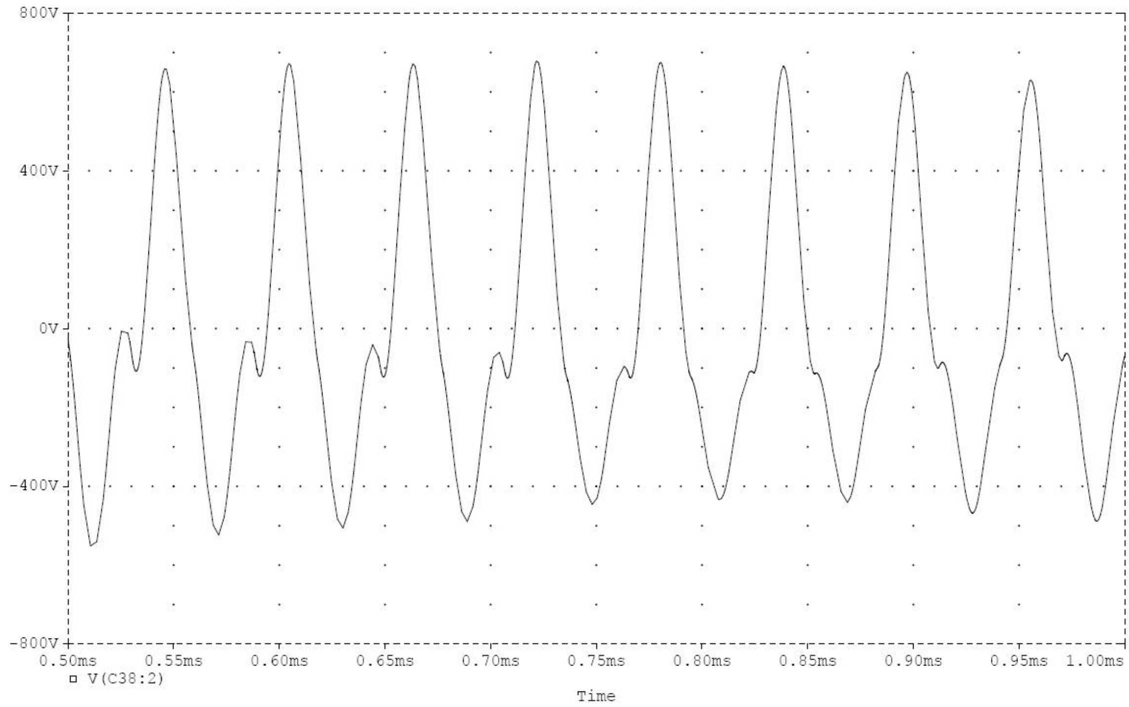


**Figure 3.14** Simulation result before discharge.

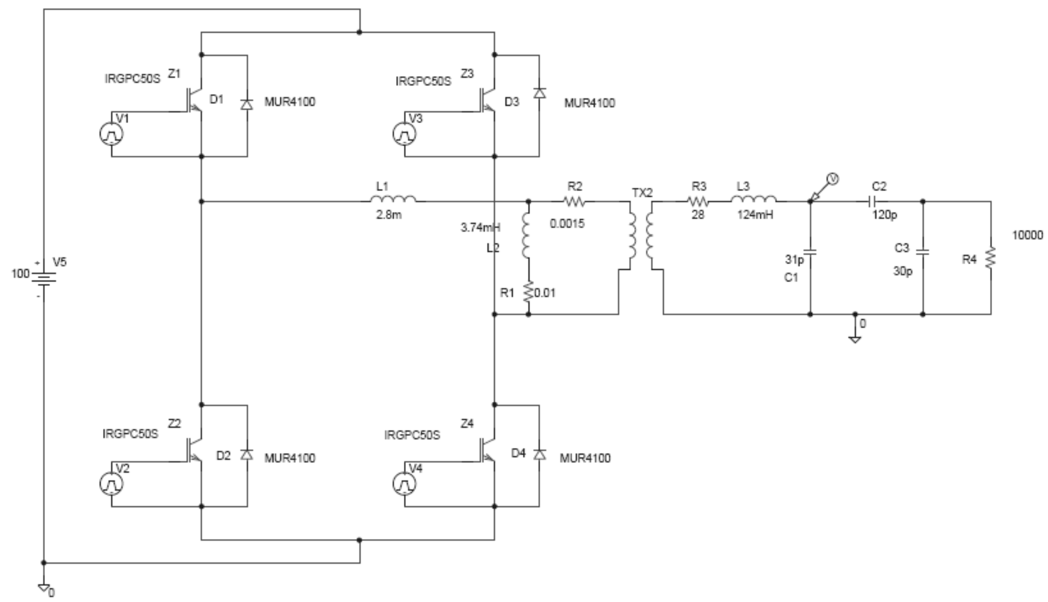


**Figure 3.15** Schematic of simulation circuit when plasma ignites.

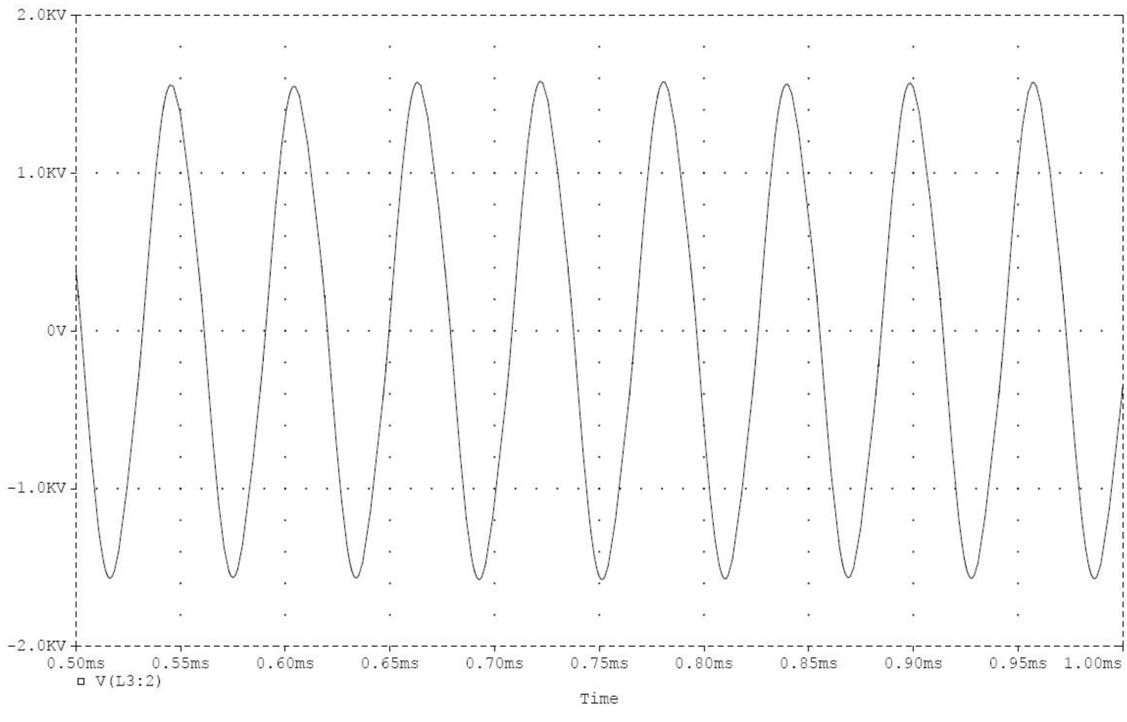


**Figure 3.16** Simulation result when plasma ignites.

### 3.1.4 Completed Work and PCB Circuit

Power controller and frequency inverter circuits are assembled in 5" × 10" single-sided PCB and full bridge MOSFETs are mounted with a heat sink. The PCB trace of circuit is shown in Fig. A4. All parts are installed in a custom-made

30×60×20 acrylic box as seen in Fig. 3.17. A voltmeter and an ammeter are also installed to indicate the power consumption of plasma by a DC product of voltage and current which are fed to frequency inverter (see Fig. 3.17). The step up transformer is placed in insulation box made from acrylic with thickness of 10 mm to ensure safety operation for a user.

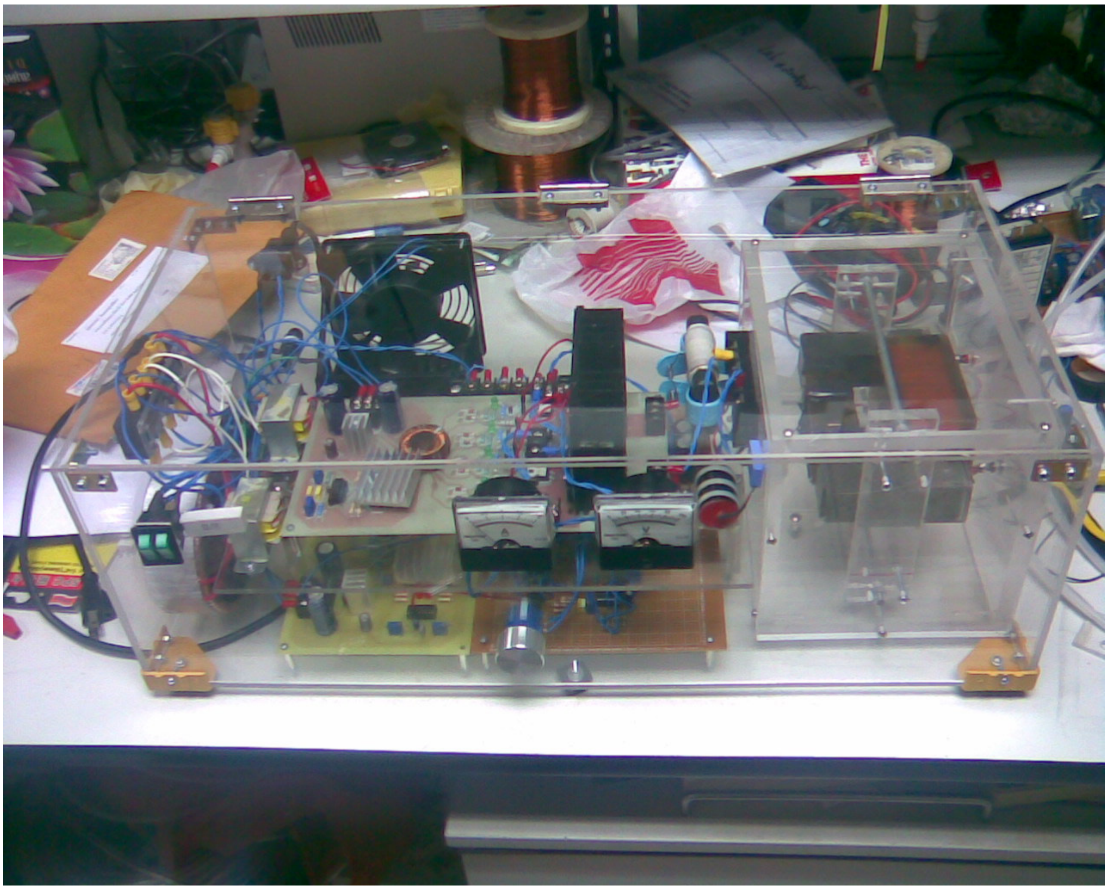

**Figure 3.17** The completed work of high voltage medium frequency power supply.

## 3.2 Dielectric Barrier Discharge System

As discussed in chapter 2, dielectric barrier discharge is one of the technique used to generate plasma at atmospheric pressure. This technique requires AC high voltage generator and specific designed plasma chamber to stabilize plasma in non-thermal equilibrium state. Certain specific properties of plasma chamber are required to facilitate both an investigation of plasma properties and the applications.

For plasma characterization; the properties of atmospheric plasma are characterized by; Optical Emission Spectroscopy (OES) and voltage-current measurement. The transparency of plasma chamber also helps observing plasma inside the chamber by naked eyes. For plasma applications; atmospheric plasma is used to modify surface properties of several materials, the large gas gap is required. Unfortunately, increasing gas gap will result in non-uniform or filamentary plasma. When the gas gap is deliberately extended, an operation at higher voltage is needed to restore the uniformity of the plasma.

### 3.2.1 The First Plasma Chamber

This plasma chamber is made from acrylic to provide clear view for an observer. The 4-mm in diameter power and ground electrode are placed inside the plasma chamber and covered with a couple of 2 mm thick rectangular glasses. The gas gap between glasses is about 2 mm provided by spacer. This chamber can be used to ignite many gases such as helium, argon and air. The plasma chamber and plasma ignition in this chamber are photographed and shown in Figs. 3.18 and 3.19 respectively.

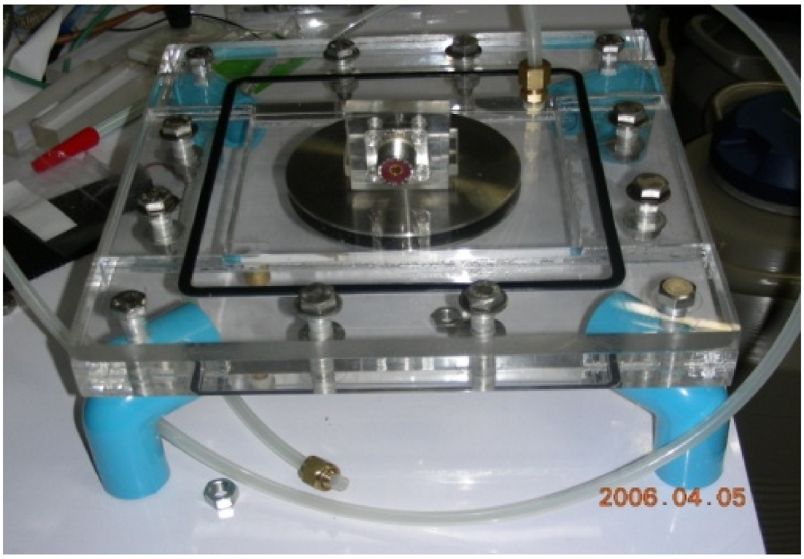


**Figure 3.18** The first plasma chamber.

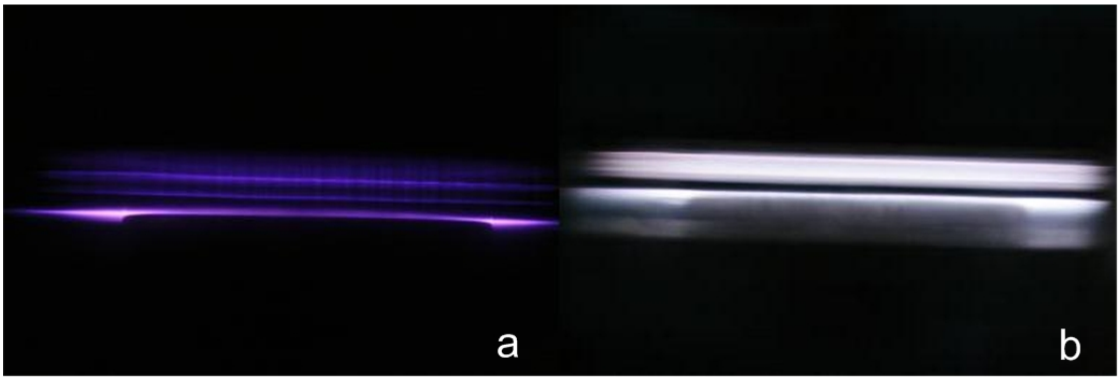


**Figure 3.19** The photographs of (a) air plasma and (b) argon plasma from the first plasma chamber.

### 3.2.2 Problems of The First Plasma Chamber

Some problems are observed when operating this chamber. For example;

1. Argon plasma cannot gain energy more than 20 watts. If power is higher, the plasma short-circuit the power electrode to the ground electrode and thus initiate an arching.
2. Because no cooling attached, the electrodes become very hot under long time operation could also cause a destruction of the dielectric barriers.
3. Voltage-current measurements are the only mean for plasma characterization.
4. Assembly time of the plasma chamber is too prolonged.

### 3.2.3 The Requirements of Plasma Chamber Characteristics

- ***Visible light transparency***; to understand and investigate effect of plasma, the common method is by naked-eye viewing which help to roughly separate uniform plasma from other patterns.
- ***Cooling system attachment***; to provide long time operation, the electrodes must be cooled to avoid a destruction of the dielectric barrier and an arching.
- ***Dielectric barrier replacement***; at developing stage, the destruction of dielectric barrier may occur so often that the replacements are necessary.
- ***OES channel measurement***; the effects of plasma are involved with radical species and metastable atom or molecule created by plasma. OES is used to

detect atomic or molecular spectral lines associated with the active species present in the plasma.

- ***Simple Assembling***; If assemble time is reduced so more experiment can be done.

#### 3.2.4 Design of The Second Plasma Chamber

The plasma chamber consists of two pieces of acrylic which the cover acrylic is 10 mm thick and the body is 30 mm thick. The cover and body acrylic are machined to insert petri dishes as dielectric barrier. The petri dishes are bought from a local science instrument supplier. The body is drilled to make 5-mm diameter hole from the side to provide OES measurements, gas inlet and outlet while the cover is grooved for O-ring. All the details drawing of chamber are shown in Figs. C1-C4. The 96-mm diameter electrodes are made from aluminum in hat shape as shown in Figs. C5-C6. They are installed outside the plasma chamber to avoid argon plasma short circuit and mounted with heat sink and cooling fan (see Figs. 3.20-3.21). The gas gap between dielectric is about 2 mm.

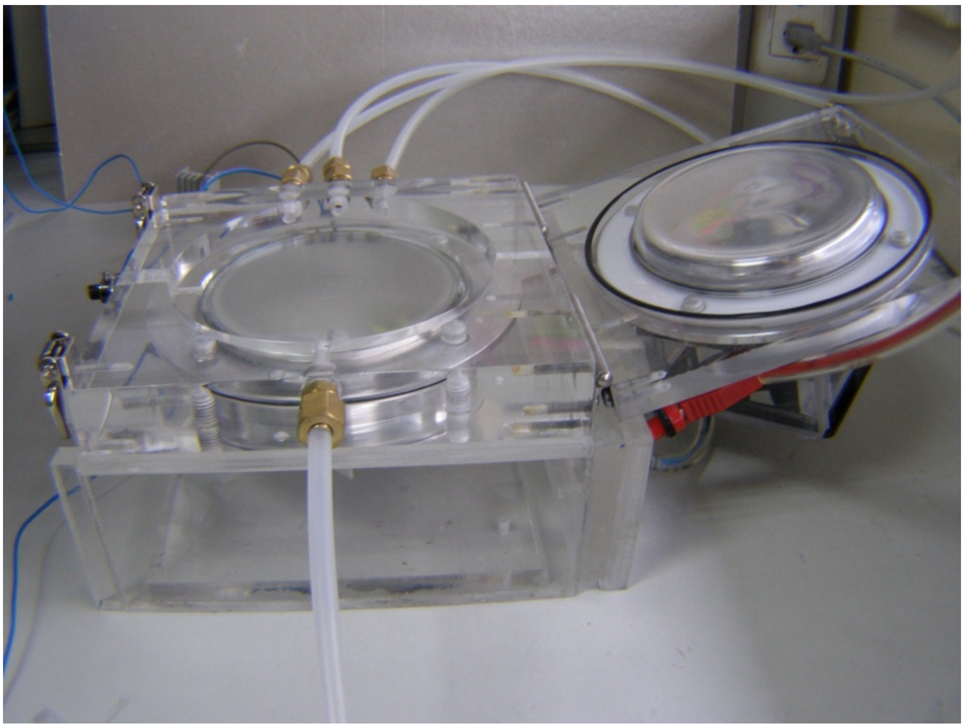

**Figure 3.20** Photograph of the second plasma chamber.

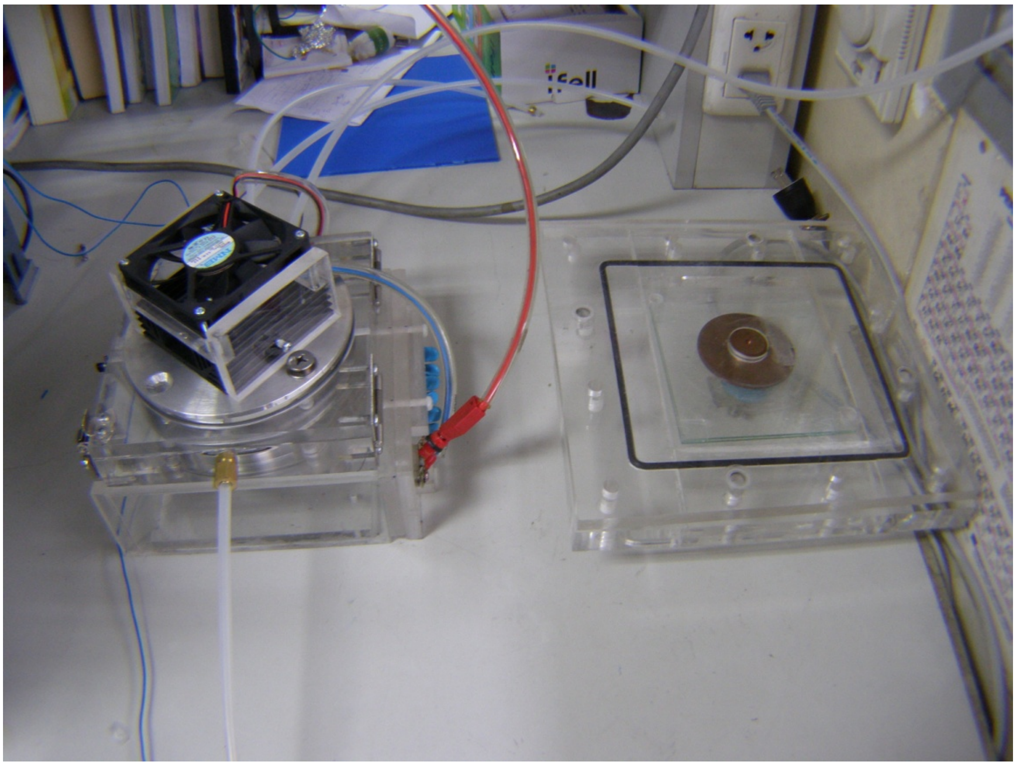

**Figure 3.21** The second plasma chamber with cooling system and the first chamber.

## 3.3 Power Supply Testing

### a) Open Circuit Testing

The secondary winding of the step up transformer is left open-circuited while a full rated voltage (130 VDC) is applied to the primary winding. The voltage is measured though 1:1000 Fluke high voltage probe and monitored by an oscilloscope TEKTRONIK TDS 200. The signal is captured by WAVESTAR FOR OSCILLOSCOPE though its RS-232 serial port. The result is shown in Fig. 3.22. The output voltage is 2.86 $kV_{p-p}$ and looks like sinusoidal with a bit distortion. The leakage current is 0.018 A.

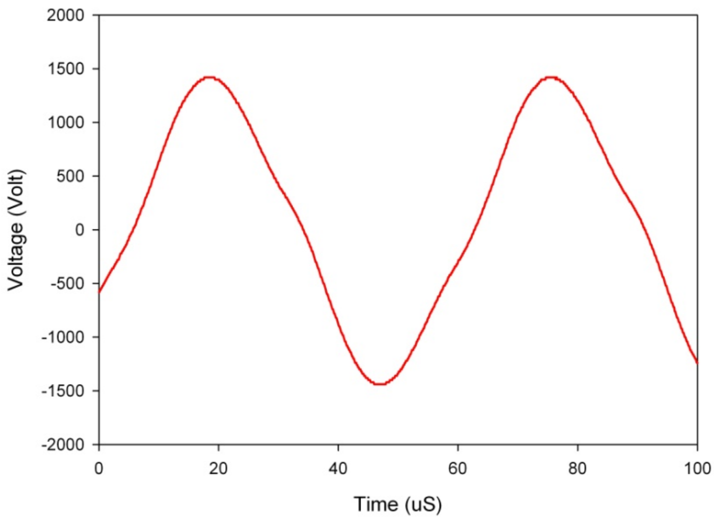


**Figure 3.22** The open circuit voltage waveform.

#### b) Testing with air-filled Chamber (Empty Chamber)

The plasma chamber is connected to the power supply. The output voltage across chamber is measured as a function of input voltage as seen in Fig. 3.23a. The output voltage rises from 2 $kV_{p-p}$ to 10.7 $kV_{p-p}$. Air is ignited when this voltage is more than 14 $kV_{p-p}$. The output voltage is linearly proportion to the input voltage. The power supply has to deliver substantial amount of current because the chamber act as the capacitance of about 30 pF (see Figs. 3.13 and 3.15). A product between the input voltage and the input current is the input power. The input power and the input current are plotted as a function of input voltage in Fig. 3.23b. Because plasma is not ignited, so only internal impedance of chamber and power supply is the load. The input voltage and input current relation is almost linearly proportion and the area under this plot, the input power, increases exponentially. The output voltage is also plotted as a function of input power as seen in Fig. 3.23c which is curve at the beginning and becomes linearly proportion at more than 20 watts.

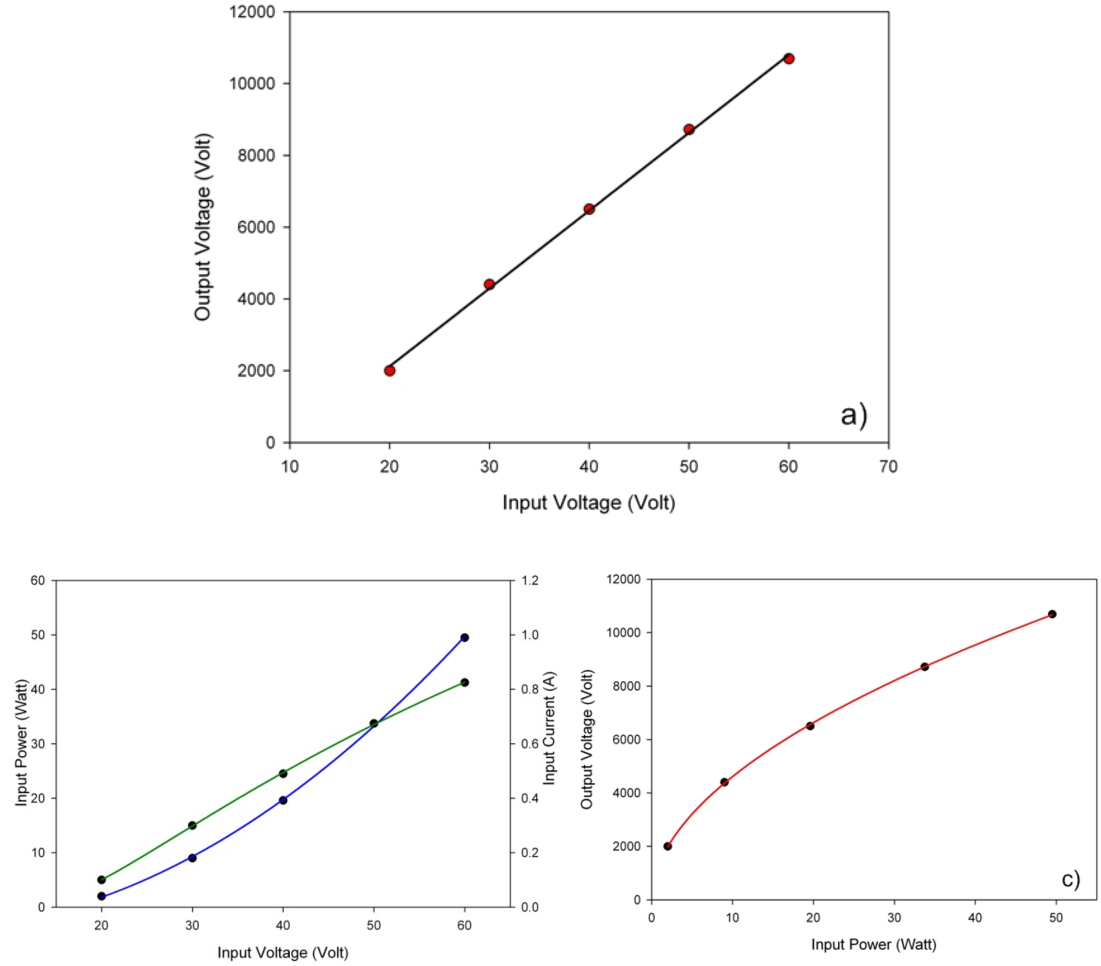


**Figure 3.23** The characteristics of power supply testing with empty chamber; a) output voltage as a function of input voltage b) Input power as a function of input voltage and c) output voltage as a function of input power.

**c) Testing with gas-filled Chamber**

Argon and helium are fed into plasma chamber. Characteristics of power supply are examined using the same method as in the air-filled chamber testing. The respective breakdown voltage of argon and helium plasma are 4.5 $kV_{p\text{-}p}$ and 1.6 $kV_{p\text{-}p}$. The characteristics of power supply in this experiment are different from those in air-filled chamber as shown in Figs. 3.24a-3.24c for argon-filled chamber and Figs. 3.25a-3.25c for helium-filled chamber. Due to plasma is ignited so the plasma impedance is included. As seen in Figs 3.24b and 3.25b, the input voltage and the input current relation is not linearly proportion which may be resulted from unsteady plasma impedance in their discharge regimes.

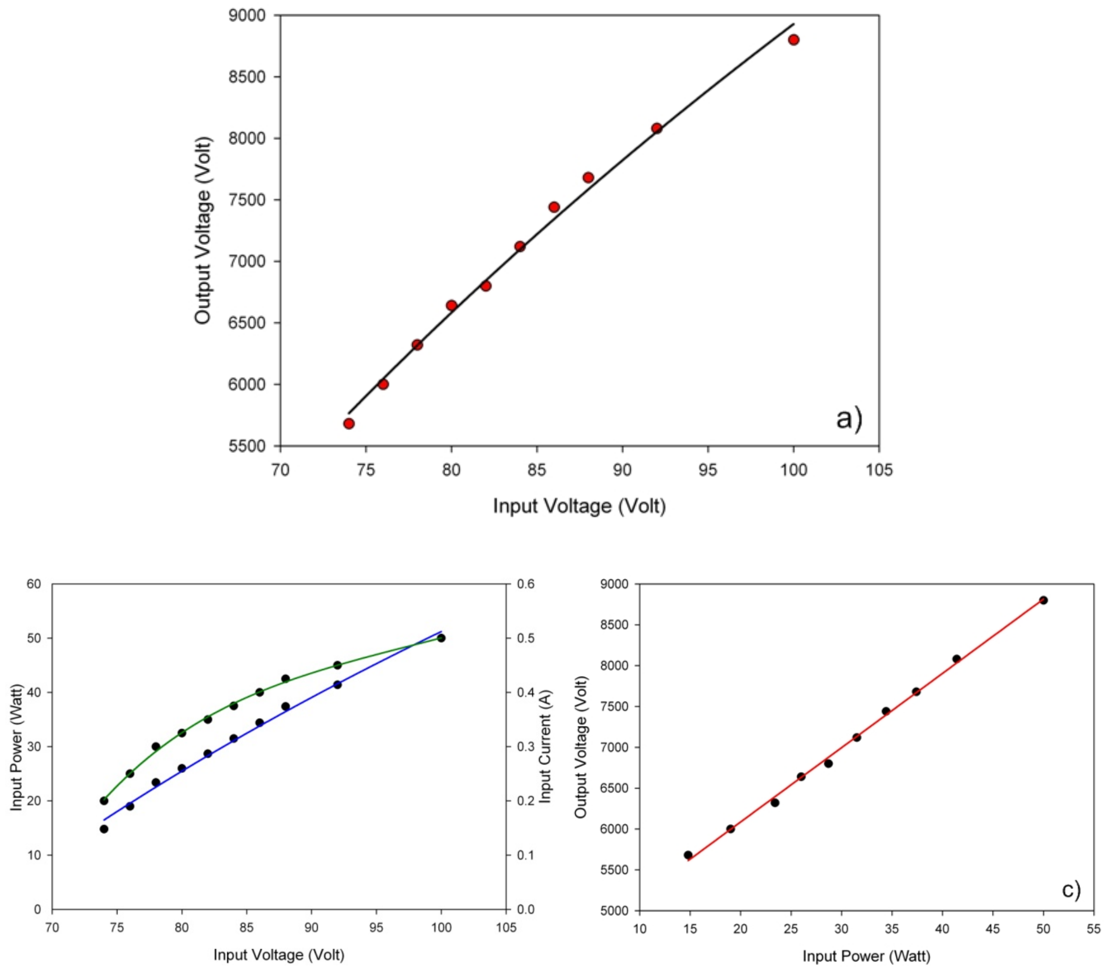


**Figure 3.24** The characteristics of power supply testing with argon-filled chamber; a) output voltage as a function of input voltage, b) input power as a function of input voltage, and c) output voltage as a function of input power.

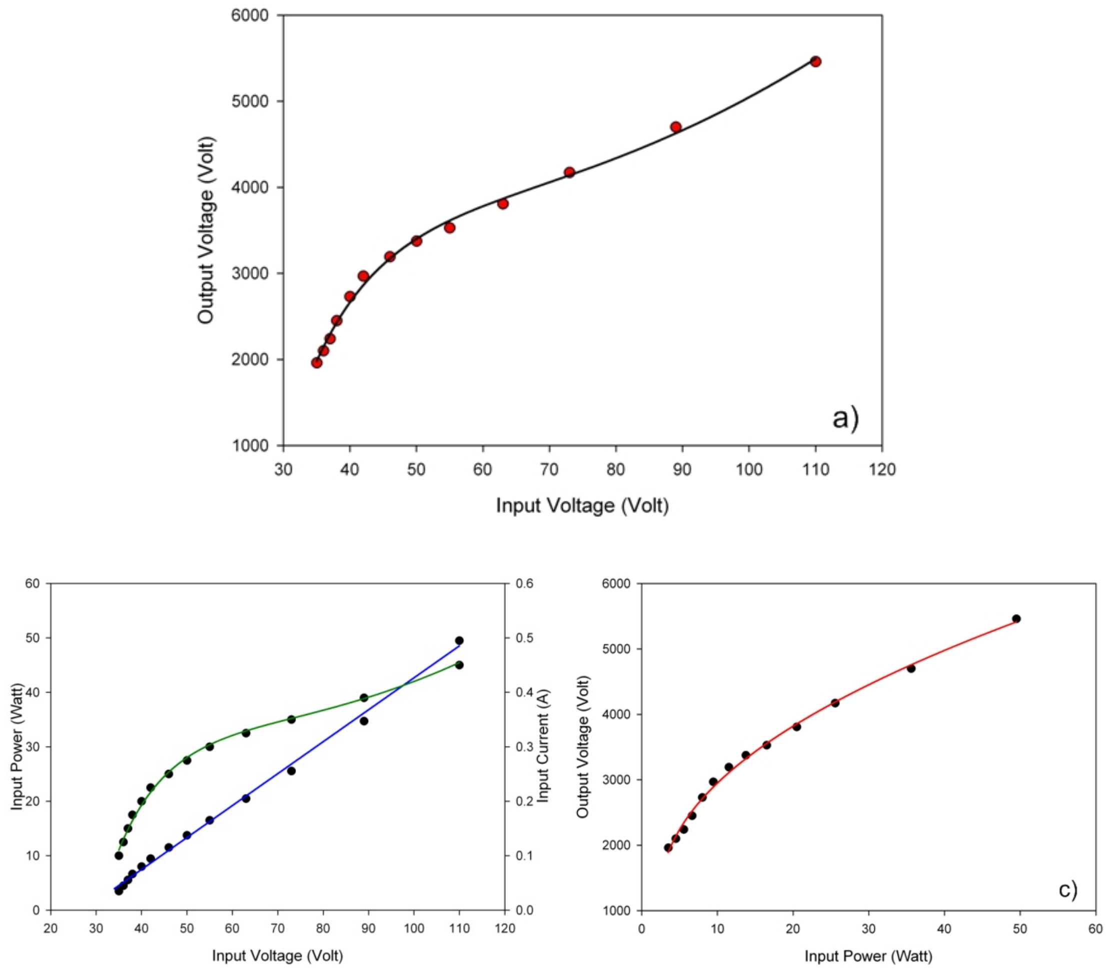


**Figure 3.25** The characteristics of power supply testing with helium-filled chamber; a) output voltage as a function of input voltage, b) input power as a function of input voltage, and c) output voltage as a function of input power.

# CHAPTER IV
# EXPERIMENTAL RESULTS AND DISCUSSION

Atmospheric plasma properties, generally, are very different from typical low pressure plasma; these differences properties include current waveform, discharge duration, optical emission spectrum and etc. Beside pressure, these properties also vary with the working gases; different gases generate plasma of different properties. Typical properties to be characterized are, for example, optical observation, voltage-current characteristic, optical emission spectrum and voltage-charge relation (*Lissajous Figure*). This chapter reports experimental observations of plasma generated at atmospheric pressure from different working gases including argon, helium, nitrogen, and air.

## 4.1 The Investigation Methods

### a) Optical Observation

This is a simple method to roughly investigate plasma properties. The atmospheric plasma is operated and observed though transparent acrylic plasma chamber wall. Several gases are fed into chamber and ignited by dielectric barrier discharge technique. Several plasma are photographed by KODAK Z650 digital camera. The camera parameters are set that exposure time is 0.1 second, F-number is 3.2 and ISO-number is 800.

### b) Voltage-Current characteristics and Lissajous Figure

The experimental setup is shown in Fig. 4.1. Gas flow controller is also set to one liter per minute flow. Fifty ohm resistor and 0.1 μF capacitor are used to measure total current and total charge transfer respectively. And voltage is measured though 1:1000 Fluke high voltage probe. All signals are monitored by an oscilloscope TEKTRONIK TDS 200 and captured by WAVESTAR FOR OSCILLOSCOPE though its RS-232 serial port. The equivalent electronic circuit is shown in Fig. 4.2. This equivalent circuit is based on a model proposed by F. Massines *et al* [27, 29, 54, 55]. In such a model, both dielectric barriers forms a capacitor connected in series with a gas capacitor. Plasma itself is assumed to be a variable impedance added in parallel with the gas capacitor.

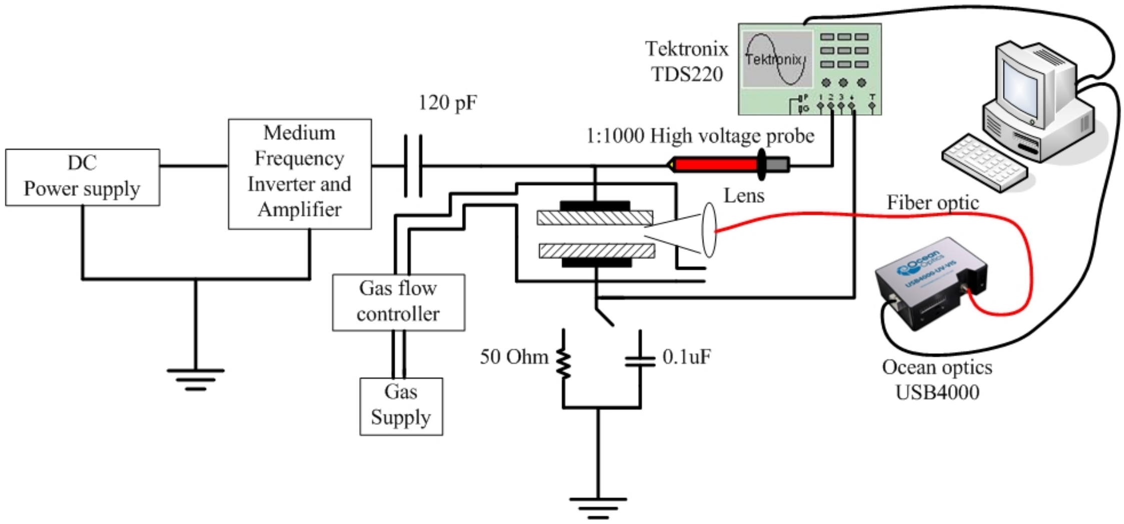


**Figure 4.1** The experimental setup.

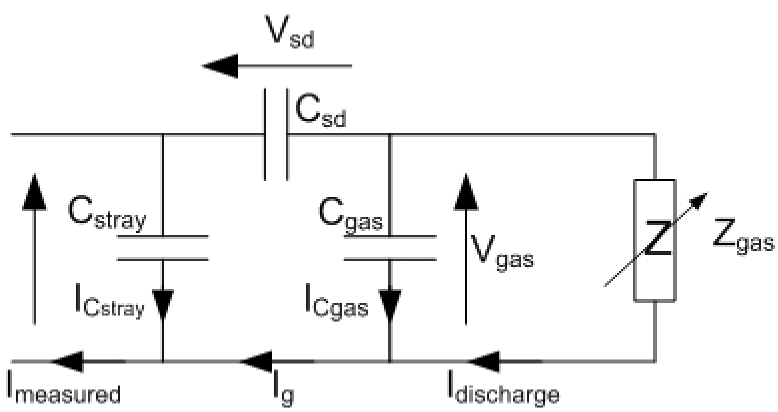


**Figure 4.2** Electrical model in plasma operation [54].

The total current has two components: a capacitive one which equal to $C_{gas}dV_{gas}/dt$ and discharge current which can be extracted from total current by these relations;

$$I_{measured} = I_g + I_{Cstray} \qquad 4.1$$

$$I_g = I_{measured} - C_{stray}\frac{dV_{app}}{dt} = C_{gas}\frac{dV_{gas}}{dt} + I_{discharge} \qquad 4.2$$

$$V_{gas}(t) = V_{app}(t) - V_m(t) \qquad 4.3$$

$$V_m(t) = \frac{1}{C_{sd}}\int_{t_0}^{t} I_g(t')dt' + V_m(t_0) \qquad 4.4$$

$V_m$ is the memory voltage calculated from Eq. (4.4) and $C_{sd}$ is a capacitance of solid dielectric. $V_m(t_0)$ is the voltage due to charge accumulating on both solid dielectrics during previous discharge which is adjusted so that the mean value of gas voltage $V_g$ is equal to 0 V to ensure no auto-polarization condition. However, the signal data is discrete; numerical method is employed to analyze the data. Before differentiation, data have been smoothed by 20-points smoothing method under ORIGIN PRO 8. The integration is defined by the trapezoidal rule;

$$V_{m_k} = \frac{I_{g_k} + I_{g_{k-1}}}{2C_{sd}}(\Delta t) + V_{m_{k-1}} + V_m(t_0) \qquad 4.5$$

where $$V_{m_0} = 0 \text{ and } I_{g_0} = 0$$

*Lissajous Figure* is the plot between charge and applied voltage. In our case, the charge is calculated from the voltage across 0.1 μF capacitor as shown in Eq. (4.6)

$$Q(t) = CV(t) \qquad 4.6$$

An example of *Lissajous Figure* is shown in Fig. 4.3 called parallelogram. The parallelogram brings us about the mechanism of discharge [20, 23, 24]. The left hand

and the right hand flanks of a *Lissajous Figure* represent the on-discharge process, while the top and the bottom flanks represent off-discharge state [56-58].

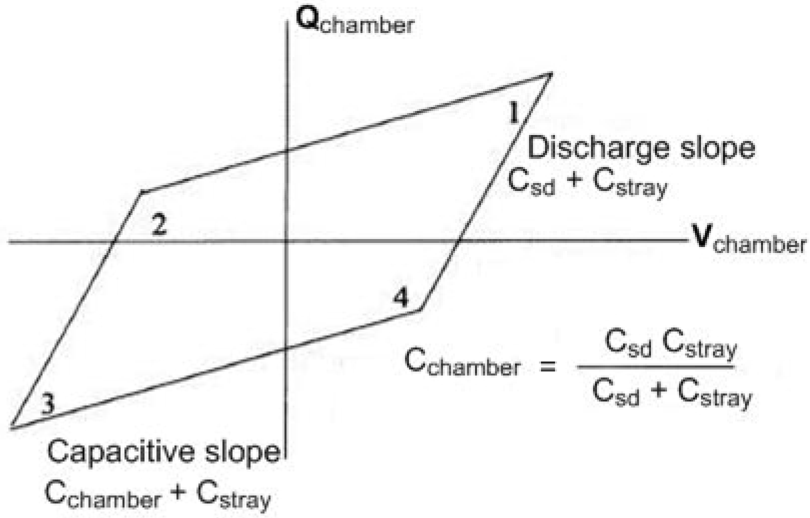


**Figure 4.3** *Lissajous Figure* including stray capacitance [57].

Slope of horizontal parallel lines, i.e., 1-2 and 3-4 lines are equal to the total capacitance of the system and other lines, i.e., 2-3 and 4-1 lines indicate the number of discharge peaks [20, 23, 24]. There are two curves in the line, corresponding to two respective discharge peaks. If plasma is not ignited yet, the *Lissajous Figure* becomes a straight line. On the other hand, many discharge pulses as found in filamentary discharge, result in many small wavy lines in series and look as if it was a straight line. In this case, slope of these lines equals to a solid dielectric capacitance.

### c) Optical Emission Spectroscopy

Optical emission spectroscopy is one of typical method to characterize atmospheric plasma. In atmospheric plasma, there are many species of ions, atoms and molecules. From Fig. 4.1, USB4000 from Ocean Optics is used to measure emission spectrum of gases. Identifications of species in plasma associated with emission peak are indicated by using *NIST atomic spectrum database* and comparing with other previously published work.

## 4.2 Argon Discharge Experiment

### a) Optical Observation

Argon plasma has bluish pink color and nearly uniform. However when the power increases up to 40-50 watts, the argon plasma exhibits filamentary discharge or arc current around the edge of an electrode. The argon plasma is shown in Fig. 4.4.

**Figure 4.4** Photograph of homogenous argon plasma with bluish pink color.

### b) Voltage-Current characteristics and Lissajous Figures

The result is shown in Fig. 4.5 which the voltage and current is the same as monitored from oscilloscope. At voltage of 5 $kV_{p-p}$ in argon, the voltage signal seem to look like sinusoidal shape but it has two necks located at both negative and positive side. Fig. 4.5 shows the voltage and current waveforms before waveform analysis and Fig. 4.6 shows both waveforms and also calculated gas voltage after waveform analysis

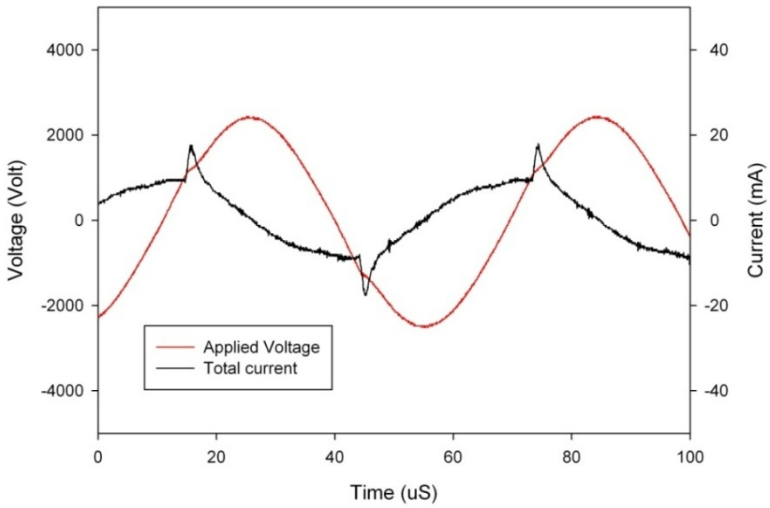


**Figure 4.5** Applied voltage (red) and measured current (black) of argon plasma as measured.

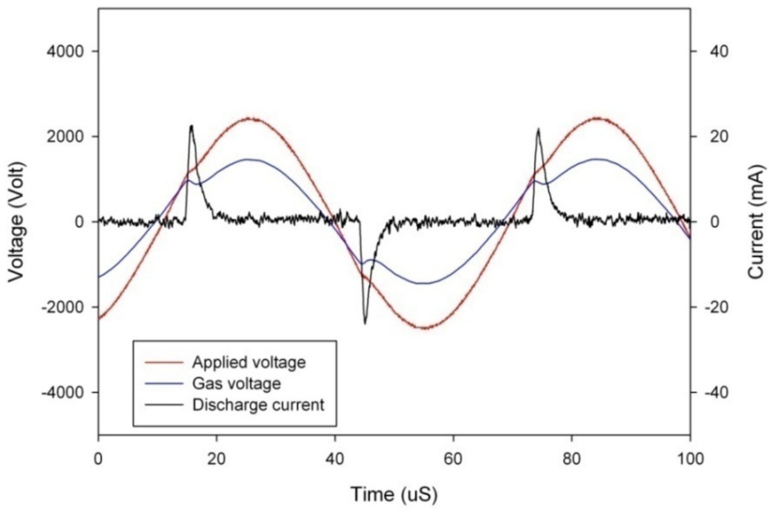


**Figure 4.6** Applied voltage (red), discharge current (black) and gap voltage of argon plasma after waveform analysis.

At the beginning the discharge current develops a single discharge peak and gas voltage drop over discharge duration (see Figs. 4.7a-4.9a). As the applied voltage increases, the discharge current exhibits more additional discharge peaks which are wider in their discharge duration but lower in amplitude as seen in Figs. 4.10a-4.12a. The corresponding gas voltage of the wider peaks seems to be constant.

The narrower discharge peaks have the discharge duration about five µS while the wider ones have the discharge duration more than 10 µS.

*Lissajous Figures* of atmospheric argon plasma at various voltages are also shown in Figs. 4.7b-4.12b which have one to three curvatures on the left or the right flanks, corresponding to number of discharge peaks. The slope of the top and the bottom lines correspond to the total capacitance of about 32-34 pF.

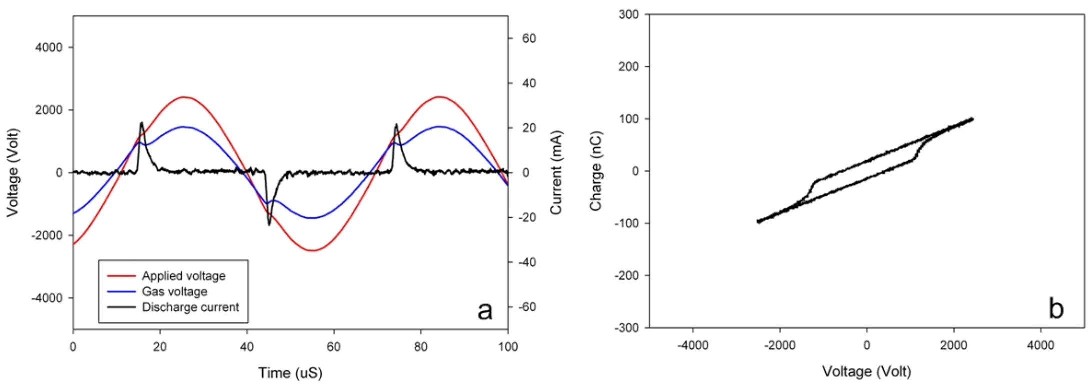


**Figure 4.7** (a) Analyzed waveforms of argon plasma at 5 $kV_{p-p}$ and (b) the corresponding *Lissajous Figure*.

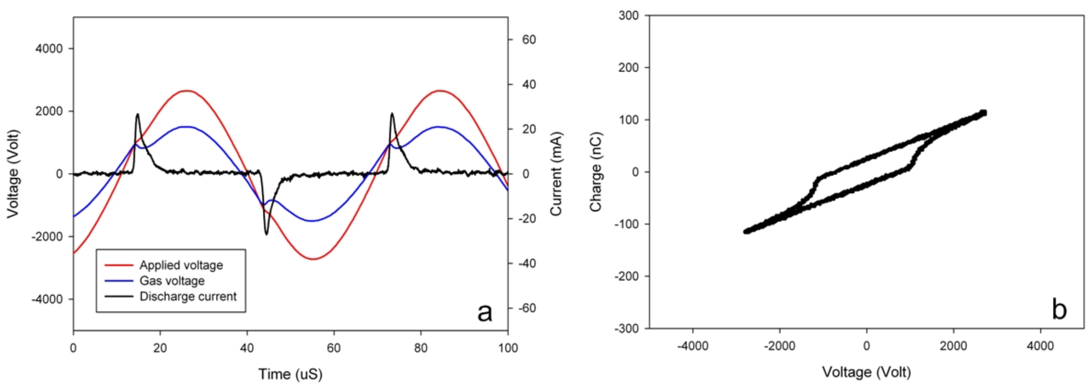


**Figure 4.8** (a) Analyzed waveforms of argon plasma at 5.5 $kV_{p-p}$ and (b) the corresponding *Lissajous Figure*.

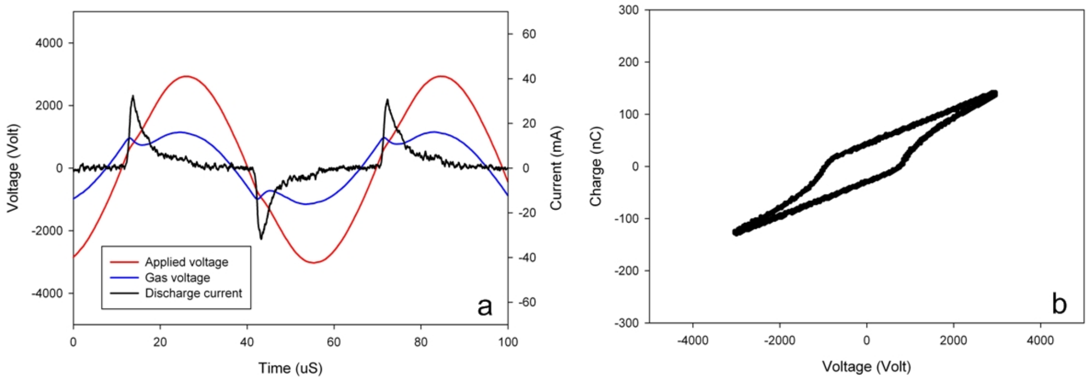


**Figure 4.9** (a) Analyzed waveforms of argon plasma at 6 $kV_{p\text{-}p}$ and (b) the corresponding *Lissajous Figure*.

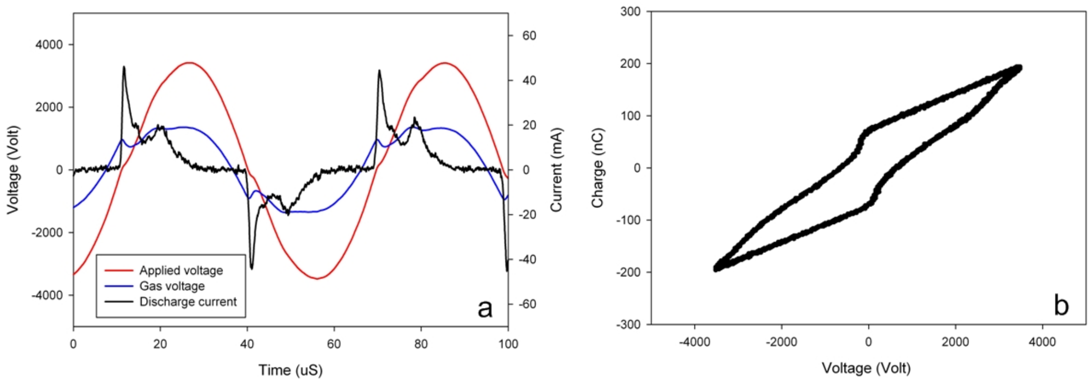


**Figure 4.10** (a) Analyzed waveforms of argon plasma at 7 $kV_{p\text{-}p}$ and (b) the corresponding *Lissajous Figure*.

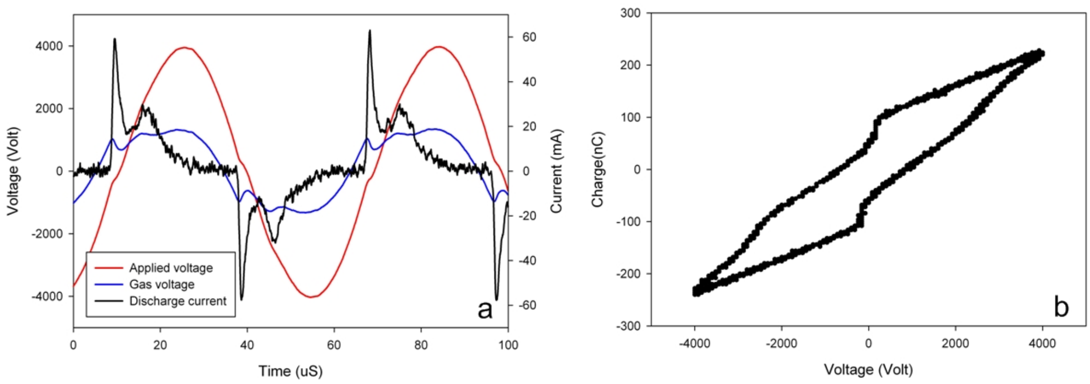


**Figure 4.11** (a) Analyzed waveforms of argon plasma at 8 $kV_{p\text{-}p}$ and (b) the corresponding *Lissajous Figure*.

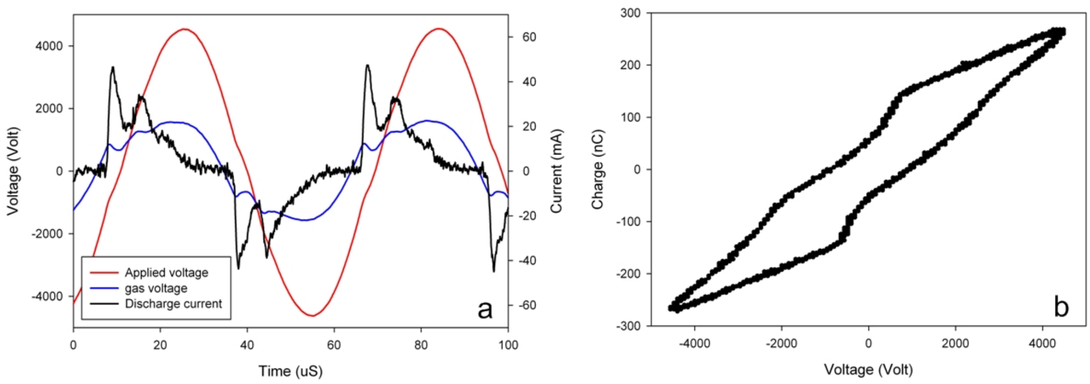


**Figure 4.12** (a) Analyzed waveforms of argon plasma at 9 $kV_{p-p}$ and (b) the corresponding *Lissajous Figure*.

### c) Optical Emission Spectroscopy

Fig. 4.13 shows the emission spectrum of atmospheric argon plasma. Their identifications are listed in Table 4.1. All argon peaks locate in red and NIR region. Residual air was not completely removed from the chamber due to insufficient purging time so its emission peaks can still be observed. The strongest peak found in the UV region at 309.0 nm is identified as OH radical, which is believed to come from water vapor in air. Some peaks in argon spectrum were identified to belong to nitrogen emission; these peaks were also found in nitrogen and air spectrum [25, 59]. After purging for two minutes, the nitrogen peak will decrease but its trace can still be observed. Minute oxygen peak is observed at 777.4 nm.

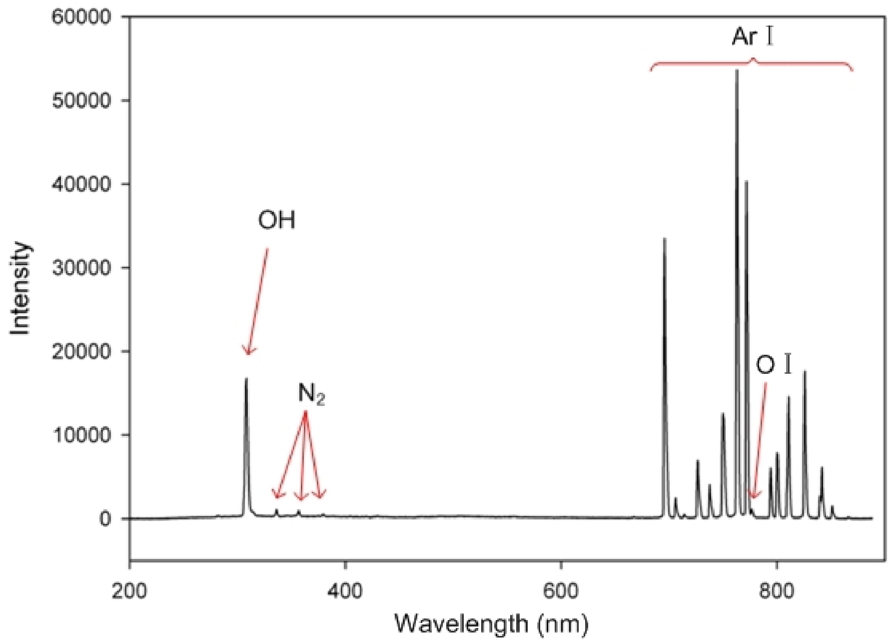


**Figure 4.13** OES of argon plasma with species identification.

**Table 4.1** Emission wavelength of species found in atmospheric argon plasma [25, 59-62].

| Species | Wavelength (nm) |
|---|---|
| **OH** | 283.3, 309.0 |
| **$N_2$** | 337.1, 357.7, 380.5 |
| **Ar** | 696.5, 706.7, 714.7, 727.3, 738.4, 750.4, 751.5, 763.5, 772.4, 794.8, 800.6, 801.5, 810.4, 811.5, 826.5, 840.8, 842.5, 852.1, 866.5 |
| **O** | 777.4, 844.6 |

## 4.3 Helium Discharge Experiment

### a) Optical Observation

Helium plasma is also investigated. It has the lowest breakdown voltage and plasma is very uniform without any filament or arc current even the power is increased up to 60-70 watts. Helium plasma has violet-blue color (see Fig 4.14).

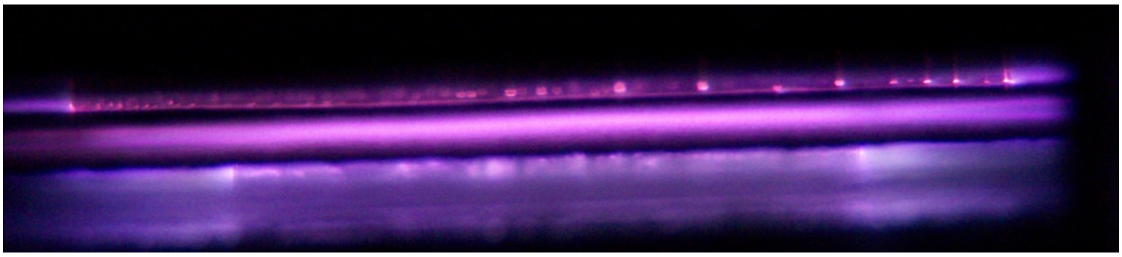

**Figure 4.14** Photograph of homogenous helium plasma with violet-pink color.

### b) Voltage-Current characteristics and Lissajous Figures

The discharge of helium occurs at lower breakdown voltage than argon and is very uniform. The discharge follows the same trend as in argon; a number of discharge peaks increase with increasing voltage or power and the discharge can be classified into two identical patterns. The marked differences are; helium discharge peaks are higher in amplitude and shorter in discharge duration than those of argon (see Figs. 4.15a-4.20a). Helium plasma can discharge up to four peaks of different discharge durations per a half cycle of different widths as found in the case of argon. The gas voltage over the narrower peak has dropped significantly while the gas voltage over the wider peaks slightly increase.

*Lissajous Figures* are also shown in Figs. 4.15b-4.20b matching with the discharge waveforms. The curvatures of parallelogram of helium are easily identified than those of argon. The slope of the top and the bottom lines are the same as that of argon; indicating the total capacitance of about 32-34 pF.

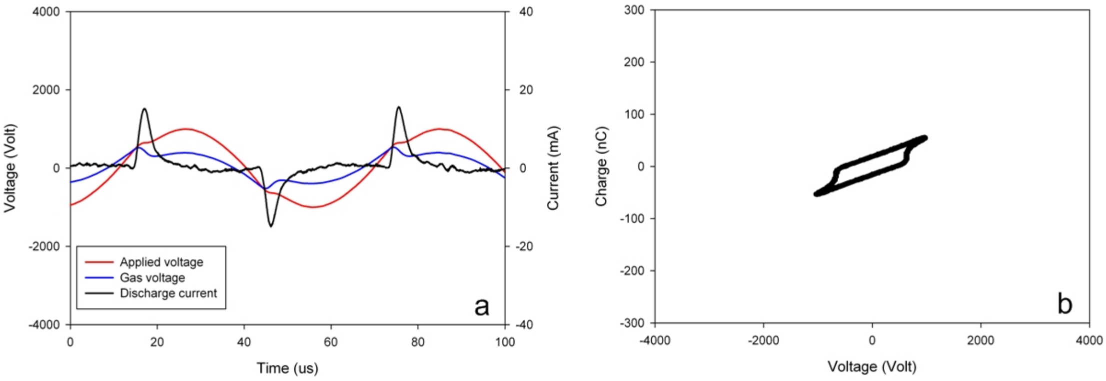


**Figure 4.15** (a) Analyzed waveforms of helium plasma at 2 $kV_{p\text{-}p}$ and (b) the corresponding *Lissajous Figure*.

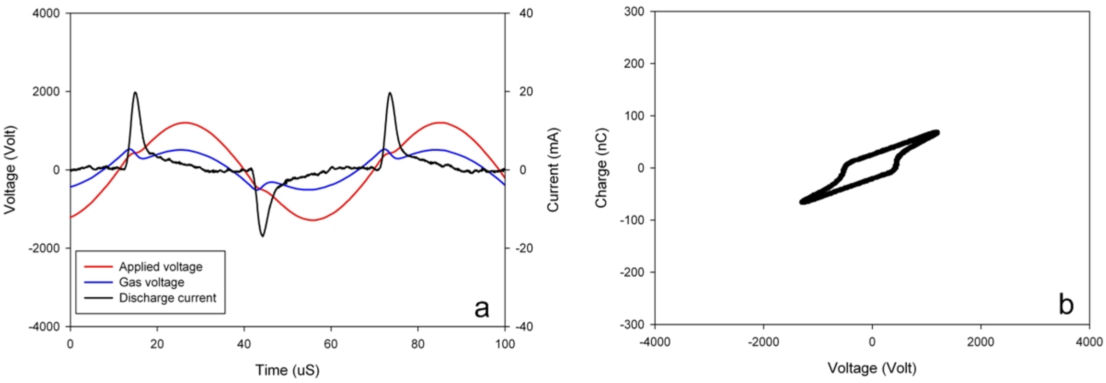


**Figure 4.16** (a) Analyzed waveforms of helium plasma at 2.5 $kV_{p\text{-}p}$ and (b) the corresponding *Lissajous Figure*.

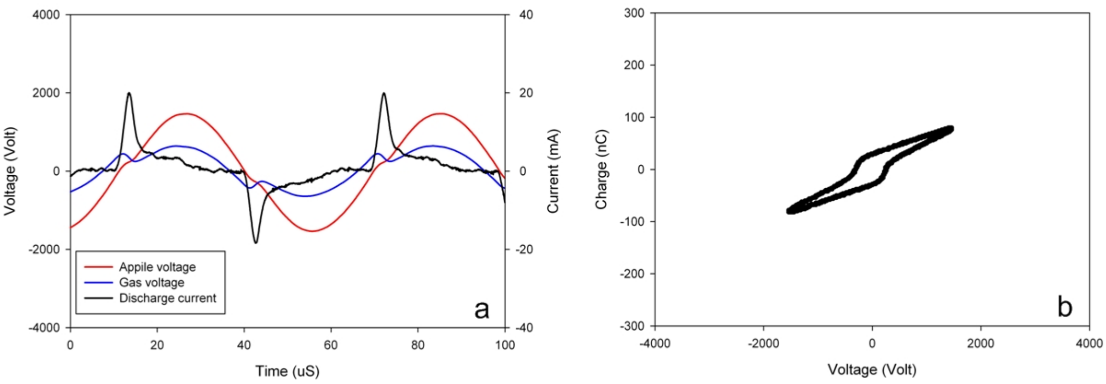


**Figure 4.17** (a) Analyzed waveforms of helium plasma at 3 $kV_{p\text{-}p}$ and (b) the corresponding *Lissajous Figure*.

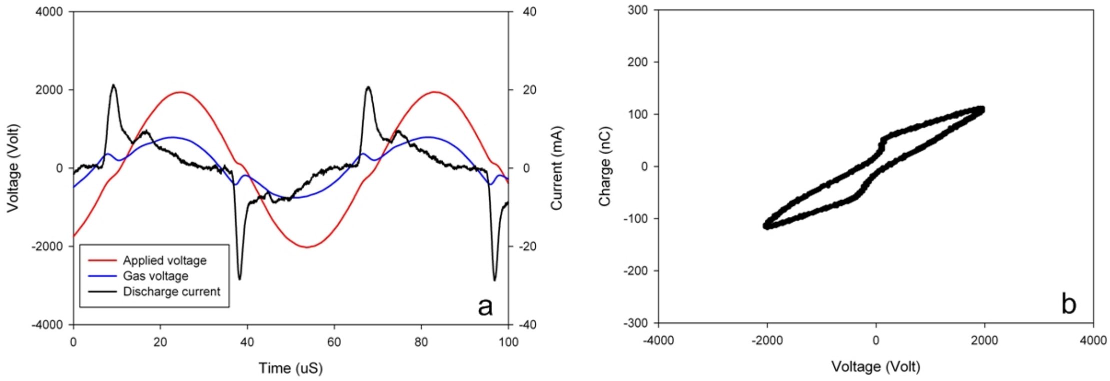


**Figure 4.18** (a) Analyzed waveforms of helium plasma at 4 $kV_{p\text{-}p}$ and (b) the corresponding *Lissajous Figure*.

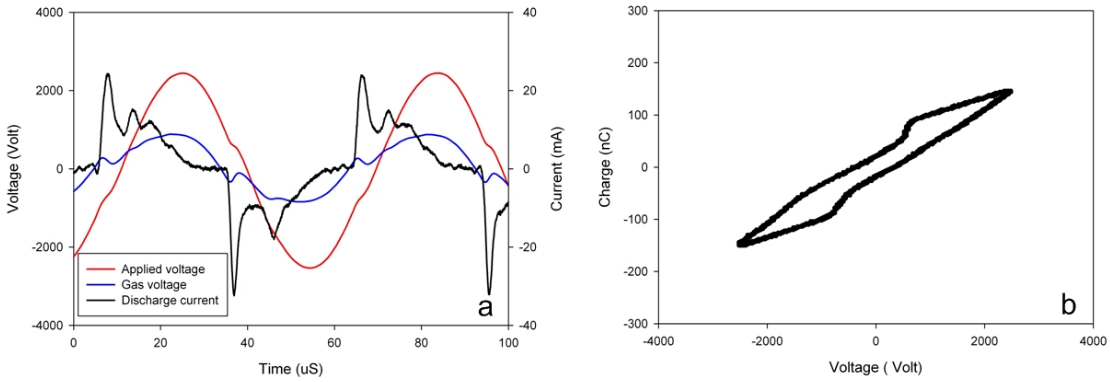


**Figure 4.19** (a) Analyzed waveforms of helium plasma at 5 $kV_{p\text{-}p}$ and (b) the corresponding *Lissajous Figure*.

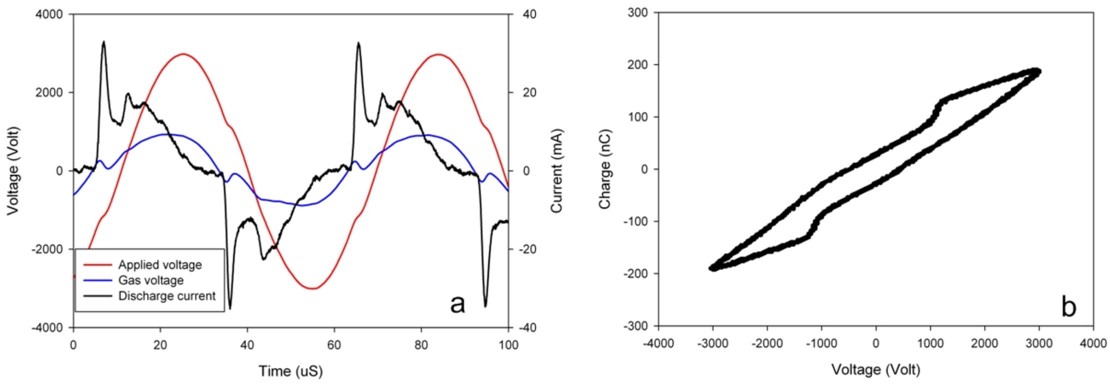


**Figure 4.20** (a) Analyzed waveforms of helium plasma at 6 $kV_{p\text{-}p}$ and (b) the corresponding *Lissajous Figure*.

### c) Optical Emission Spectroscopy

Fig. 4.21 shows atmospheric helium plasma emission spectrum which dominates by those of helium and is mixing with those of other gases. This mixing may come from inadequate purging time; therefore, residual air in the chamber could not be completely suppressed so the OES of air (mainly nitrogen) can still be observed in helium spectrum. Furthermore the hydrogen-alpha and oxygen radical peaks also found in this spectrum. All the peaks are listed in Table 4.2. The strongest and highest peak in helium spectrum is found at 391.4 nm and identified to be from $N_2^+$ following the *Penning ionization* mechanism. Other $N_2^+$ peaks are found at 427.8 and 470.9 nm. OH radical peak at 309.0 nm is observed. Its relative intensity with respect to the nearest $N_2$ peak at 315.6 nm is lower than that observed in argon plasma (see Fig. 4.13 for comparison) under operation at the same power. The helium emission peaks are found at 587.5, 667.8, 706.5 and 728.1 nm.

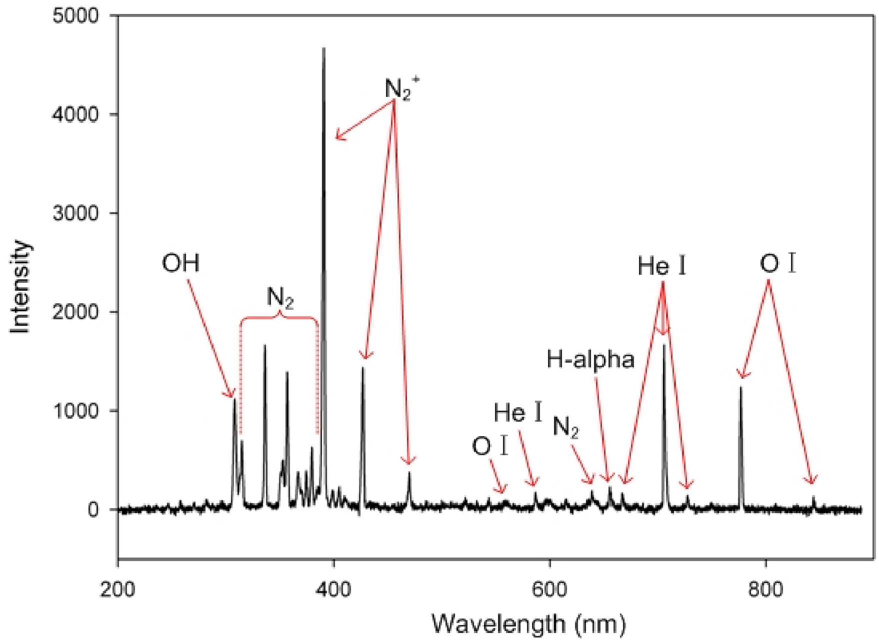


**Figure 4.21** OES of helium plasma with species identification.

**Table 4.2** Emission wavelength of species found in atmospheric helium plasma [28, 62-65].

| Species | Wavelength (nm) |
|---|---|
| **OH** | 283.3, 309.0 |
| **$N_2$** | 315.6, 337.1, 353.7, 357.7, 367.0, 375.4, 380.5, 399.7, 405.8, 640 |
| **$N_2^+$** | 391.4, 427.8, 470.9 |
| **H** | 656.3 |
| **He** | 587.5, 667.8, 706.5, 728.1 |
| **O** | 557.7, 777.4, 844.6 |

## 4.4 Air and Nitrogen Discharge Experiments

### a) Optical Observation

Air and nitrogen plasma is more difficult to generate; consists of many filaments following their very high breakdown voltage. The colors of air plasma and nitrogen plasma are slight different; air plasma has violet-blue color (see Fig. 4.22) while nitrogen has blue color as shown in Fig. 4.23. Some plasma research groups were able to operate uniform air or nitrogen plasma by using 50 Hz high voltage power supply with more specifically custom-designed electrode [20, 66].

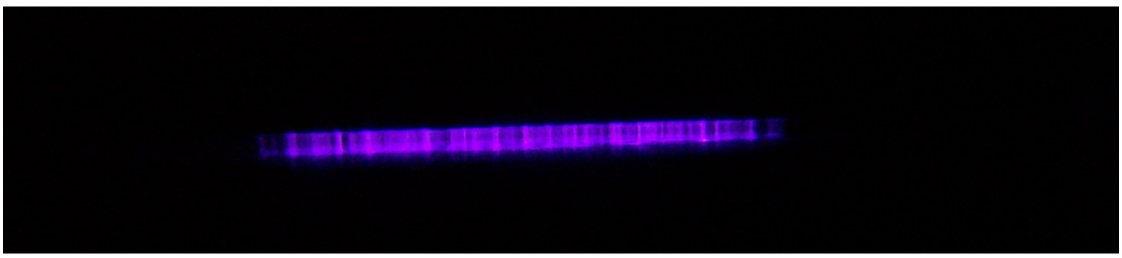

**Figure 4.22** Photograph of air plasma consisting of violet-blue filaments.

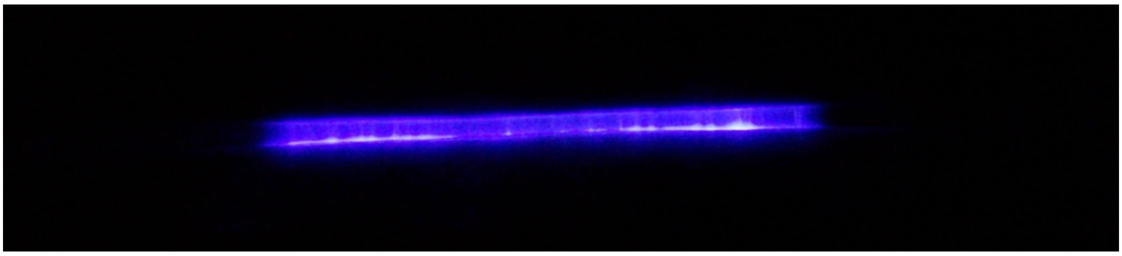

**Figure 4.23** Photograph of filamentary nitrogen plasma with blue color.

### b) Voltage-Current characteristics and Lissajous Figures

Air composes of nitrogen about 78%, oxygen 20%, and other gases 2%. The discharge of nitrogen and oxygen are obviously filamentary type. The breakdown voltage of both gases is very high (>17 $kV_{p-p}$) for the same gas gap. Besides, there is no narrow peak but only the wide peak consisting of many nanosecond duration discharge peaks (filamentary discharge) is observed. This is in contrast to what has been seen in case of argon or helium plasma. The voltage over discharge duration is almost constant as also found in case of argon and helium.

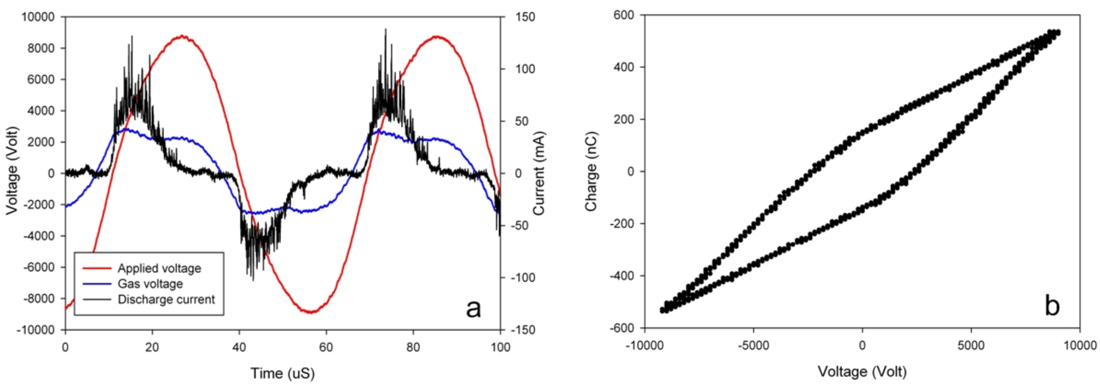


**Figure 4.24** (a) Analyzed waveforms of air plasma at 17 $kV_{p-p}$ and (b) the corresponding *Lissajous Figure*.

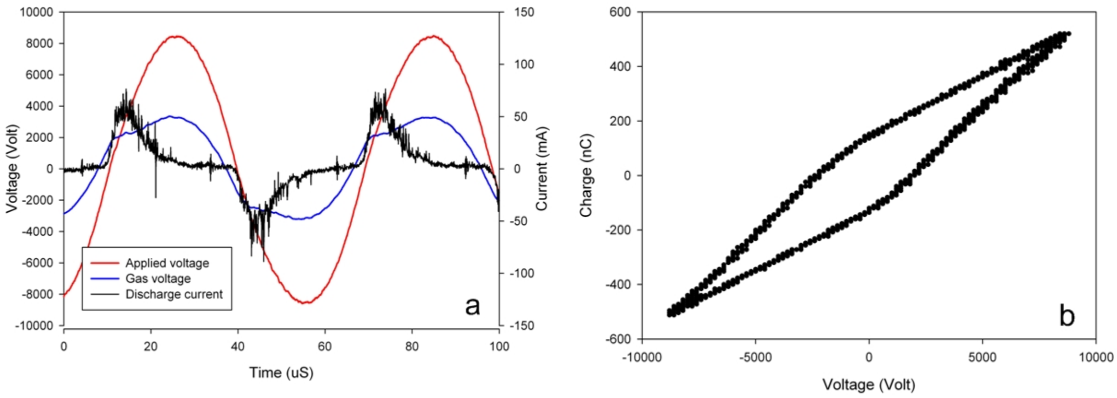


**Figure 4.25** (a) Analyzed waveforms of nitrogen plasma at 17 $kV_{p-p}$ and (b) the corresponding *Lissajous Figure*.

The waveform of air and nitrogen discharge are shown in Figs. 4.24a and 4.25a respectively. Due to the discharge mode of air and nitrogen are filamentary discharges so the *Lissajous Figure* of air and nitrogen plasma in Figs. 4.24b and 4.25b look like completed rhombus (see Fig. 4.3). The total capacitance of system and dielectric barrier are calculated from the slope of rhombus, are 34-36 pF and 80 pF respectively.

### c) Optical Emission Spectroscopy

The OES of air plasma are shown in Figs. 4.26 and 4.27. For air, the emission spectrum is almost identified to come from nitrogen due to the fact that nitrogen is the major composition in air (see Table 4.3). By extending the integration time of USB4000 to gain more intensity, the very small peak of O radical is observed at 777.4 nm as shown in Fig. 4.27.

In the case of nitrogen emission spectra (see Fig. 4.28), Identification of those peaks are summarized in Table 4.4. Our emission spectrum, sorted according to the previously published data [66-70], is identified as from $N_2$, $N_2^+$ and NO emission.

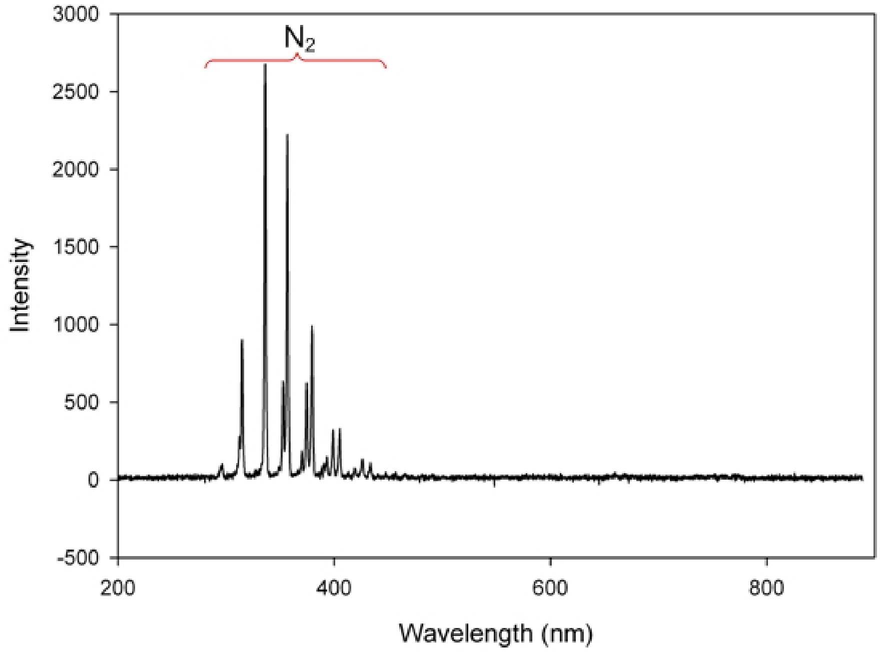


**Figure 4.26** OES of air plasma with species identification.

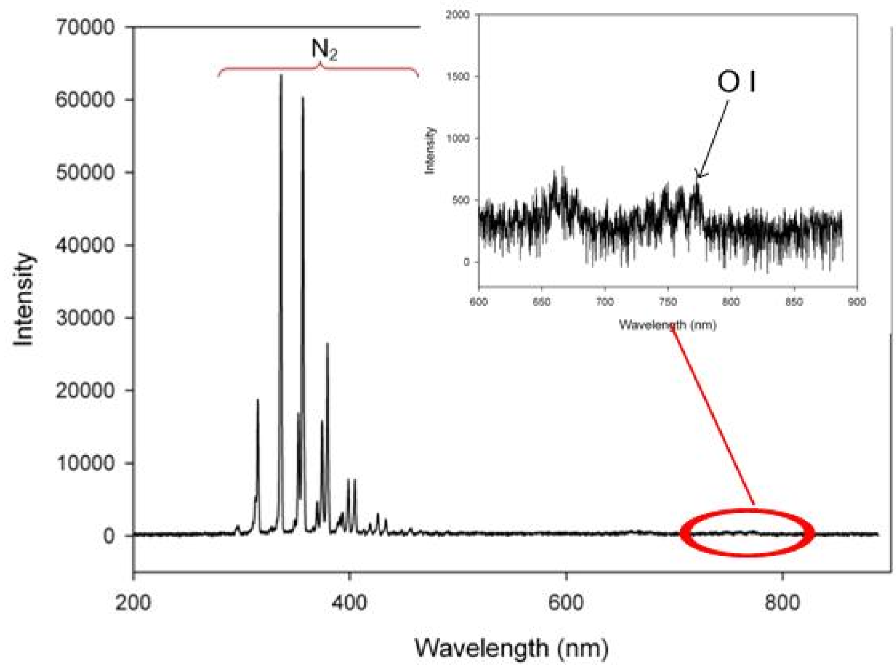


**Figure 4.27** OES of air plasma with extending integration time.

**Table 4.3** Emission wavelength of species found in atmospheric air plasma [66-70].

| Species | Wavelength (nm) |
|---|---|
| $N_2$ | 297.5, 313.4, 315.8, 337.1, 353.7, 357.7, 370.9, 375.4, 380.5, 394.1, 399.7, 405.8, 426.9, 434.4 |
| $N_2^+$ | 391.1, 419.9 |
| O | 777.4 |

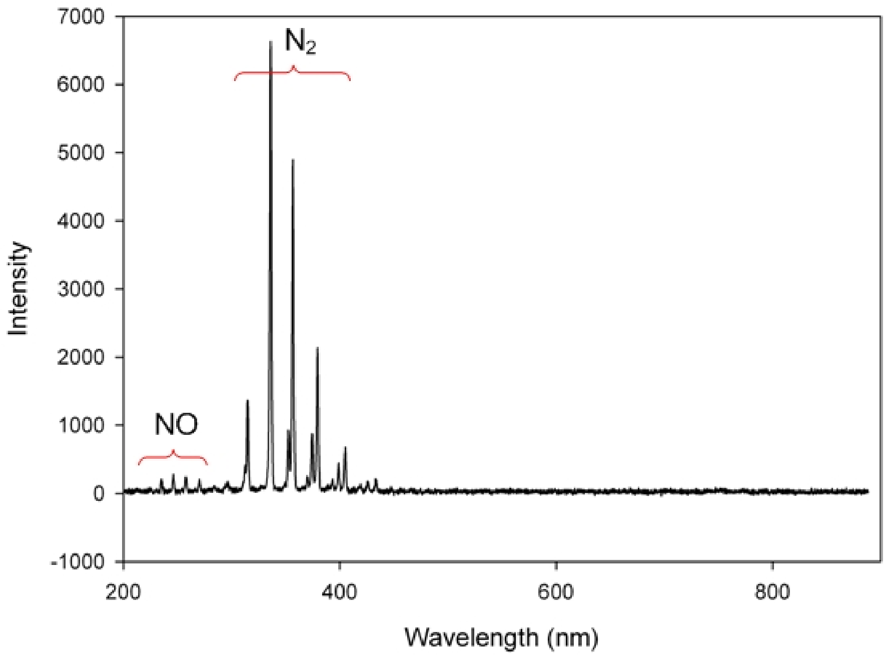


**Figure 4.28** OES of nitrogen plasma with species identification.

**Table 4.4** Emission wavelength of species found in atmospheric nitrogen plasma [66-70].

| Species | Wavelength (nm) |
|---|---|
| $N_2$ | 297.5, 313.4, 315.8, 337.1, 353.7, 357.7, 370.9, 375.4, 380.5, 394.1, 399.7, 405.8, 426.9, 434.4 |
| NO | 236.3, 247.1, 258.7, 271.3 |
| $N_2^+$ | 391.1, 419.9 |

## 4.5 Discussion

Atmospheric plasma can be classified into two modes which are 1) homogenous mode and 2) filamentary mode [17, 20, 23, 24, 54, 55, 65, 70-72]. The former mode is common in argon, helium or rare gas plasma while the latter mode is found in air or nitrogen plasma. This plasma mode is also affected by other parameters such as gas gap [22-24], pressure [17, 23, 70], power source frequency [15, 72, 73], dielectric barrier thickness [22-24], gas concentration [59, 74] and dielectric materials [22, 23].

Homogenous plasma has two patterns of discharge. The first pattern is higher in amplitude but shorter in discharge duration than the second pattern. In the past, all plasma researches group report both patterns as *Atmospheric Pressure Glow Discharge* (APGD). In 2005 F. Massines *et al* [29] purposed the term *Atmospheric Pressure Townsend Discharge* (APTD) to describe the second pattern which has lower amplitude and longer discharge duration. The gas voltage over the second pattern duration is almost constant and better suited to Townsend discharge [21, 28, 29, 75]. The Townsend discharge is taking place at the anode, while the glow discharge at the cathode. This difference is confirmed by high speed camera with very short exposure time. Glow discharge is the common discharge mode for low pressure plasma. After Massines group, other research teams also found and confirm this observation [21, 22, 28, 29, 73, 75]. The two modes cannot be distinguished by optical emission [15, 23] but only through the voltage-current.

Y.B. Golubovskii *et al* [21] experimentally investigated external parameters such as gap width and barrier thickness. They have found that only when the barrier capacitance is large, which can be achieved by using thin barrier and the wide gap, the glow-like mode can develop; otherwise the Townsend-like mode is taking place. Many groups [15, 22, 28, 70, 75] also investigate the effect of impurity gas in which the APTD is formed. Many processes, which may be induced by metastable nitrogen molecules, e.g., *secondary electron emission* from the dielectric barriers, can assist the transition to glow discharge. The APGD is formed when the ionization rate is highly efficient enough at a comparatively low electric field strength to assist the indirect ionization (*Penning ionization*) with metastable states of helium and compounds of nitrogen impurities [17, 22, 27-29, 54, 56, 63, 64, 70, 75]. Argon metastables (with excited energy of 11.6 eV) do not have enough energy to ionize $N_2$ ($E_{ion}$ = 15.5 eV) directly but helium metastables do ($E_{He*}$ = 20.0 eV). It is then clear that the *Penning ionization* is not seen in argon plasma which in turn makes argon discharge from glow to filamentary. The two-step process slows down the ionization rate from electron avalanche but rather enhances the formation rate of the streamer [19, 55]. Thus, at comparatively low electric field, relatively low ionization rate prevent ion multiplication from rapidly grow. Electrons have sufficient time to radially diffuse away. The electron avalanches can connect to each other. In such a case, space charges could not create large local field gradient [19, 22, 55]. R. Brandenburg *et al* [22, 64] suggest that if gas with ionization energy lower than 11.6 eV, e.g., $NH_3$ were mixed. The APGD can still be achieved.

Several cases in atmospheric plasma tend to be non-homogenous or filamentary plasma which form a narrow channel of plasma connecting the two electrodes together. This mode is well known and widely used to generate ozone in many industries [6, 7]. Air and nitrogen plasma mostly are ignited in filamentary mode. The homogenous-filamentary transition conditions have been examined by many groups [17, 22, 55, 65, 70, 71]. In 2009, Z. Fang *et al* [23, 24] investigated the effect of such parameters in air plasma. They studied the transition from homogenous to filamentary mode and found that with the increasing gap width reduce the transition pressure. Also, the range of pressure and gap width for obtaining homogenous plasma was larger if thickness of the barrier of given materials is thin. J. R. Roth *et al* [15] investigated atmospheric helium plasma with 2.5 cm gap width with varying power supply frequency. They have found filamentary occurred more often with the increasing frequency.

In this work, atmospheric helium plasma in a custom design chamber is found to be APGD at low voltage. This can be noticed from a single narrow current peak. Multiple current peaks started to appear when the applied voltage was given above 3 $kV_{p\text{-}p}$. The multiple peaks signify the APTD character in the plasma. Similar trend is also found in the case of argon. At low voltage the single narrow current peak occurs corresponding to APGD. Multiple current peaks occur as well with the increasing applied voltage. However, at high voltage about 8-9 $kV_{p\text{-}p}$, corresponding to 30-40 watts, filamentary plasma were observed which imply mixing plasma mode. Multiple discharge current peaks for both argon and helium are; the first peak is a decreasing gas voltage while the other peaks have a constant gas voltage. Both plasmas can be concluded to be homogenous plasma consisting both APGD and APTD. Their *Lissajous Figures* have curvy lines on the left and the right flanks. Number of curvatures indicates the number of discharge peaks. In the case of air and nitrogen, due to the rapid quenching of nitrogen metastables in nitrogen-oxygen mixtures [58], it is not possible to generate homogenous plasma without special technique [20, 66]. Their plasma was identified mainly as filamentary plasma. However, at a closer look, their discharge current has a wider current peak containing many nanosecond duration peaks inside; thus imply plasma mode was in mixed mode between APTD and filamentary discharge.

# CHAPTER V
# PLASMA EFFECTS AND APPLICATIONS

An atmospheric plasma system has been present in Chapter 3. This chapter focuses on its applications for plasma activation and starch modification. In this work only atmospheric argon plasma is investigated. The other gases can be applied to such applications however the plasma effects will be different depending on radical species in the plasma. Some gases may have difficulties to operate in open air due to the subsequent toxic species.

## 5.1 Contact Angle Measurement

The contact angle measurement is the gross way to show the effect and application of plasma. The contact angle can be measured immediately by measuring the size of water droplet on the substrate surface. This effect involves the surface energies of at the interface between the substrate and the tested liquid. The substrate under this investigation is Indium Tin Oxide (ITO) thin film. ITO thin film is common for optoelectronics applications due to its high electrical conductivity and visible light transparency. In such application, ITO with and without plasma treatment can be used as anode and cathode of different work-function energy. ITO thin films were cleaned by methanol and dried by purging nitrogen gas before treated. The plasma chamber was purged with pure argon gas for two minutes. ITO samples treated by argon plasma were exposed to ambient air for two minutes before measuring contact angle. Each ITO samples were treated and inspected under various conditions such as applied power and treatment time. The contact angle was measured from and a photograph taken by Sanyo CCD camera model vcc-5775p. An average value of four drops is used for comparison. The result of contact angle measurement is shown in Figs. 5.1-5.4 and plotted as the function of applied power and treatment time respectively.

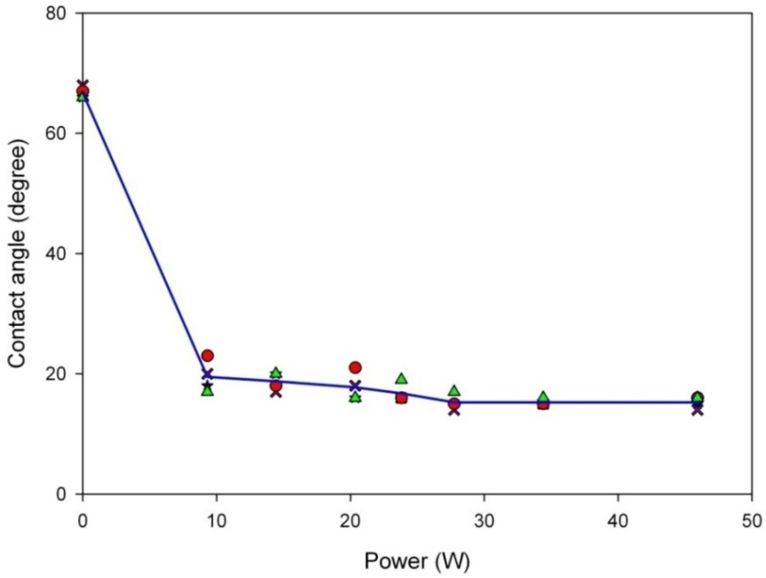


**Figure 5.1** Water contact angles on ITO surface as a function of applied plasma power.

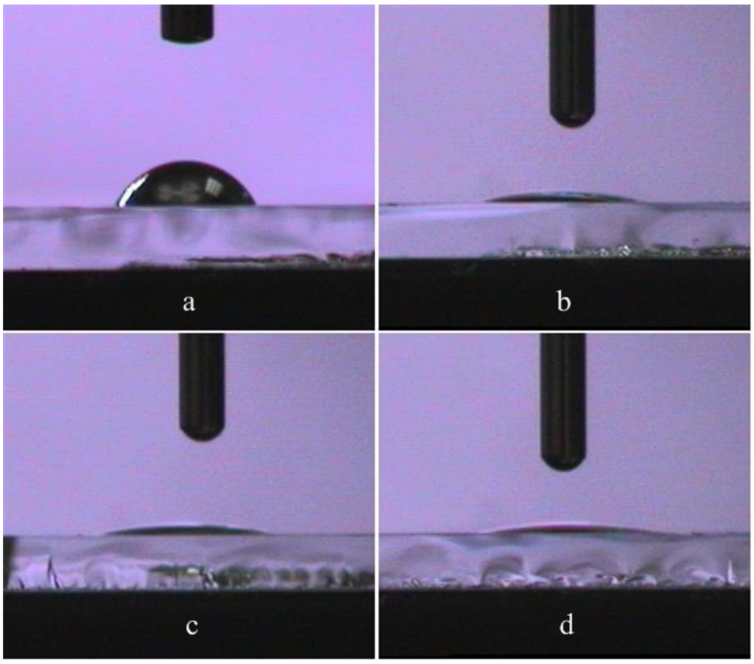


**Figure 5.2** Photographs of water drops after plasma treatment at (a) 0 W (b) 10 W (c) 20 W (d) 45 W.

Fig. 5.1 shows experimental results of plasma power affecting contact angle. The initial contact angle of water on ITO surface is 66.0 degree and then steeply decreases to 19.5, 18.8, 17.8, 16.8, 15.3, 15.3 and 15.3 by fixing treatment time of 20 seconds at the respective applied power of 9, 14, 20, 24, 27, 34 to 46 watts (see Fig. 5.2). Plasma treatment increases ITO surface energy dramatically as can be seen from the sharp drop from 66.0 degree in untreated samples to 19.5 degree in the treated ones. Reduction in water contact angle is only a slight function of an applied power which reflects the plasma process and its saturation. The contact angle slightly decreases when treating with power more than 20 watts.

The effect of treatment time is also investigated and plotted as a function of treatment time at fixed applied power of 30 watts (see Fig. 5.3). The contact angle of water on ITO decreases from 66.0 degree to 38.0, 26.0, 15.0, 14.0, 14.3, 11.0, 11.8 and 11.0 degree under the respective treatment time of 5, 10, 15, 20, 25, 30, 40, 60, 90 and 150 seconds (see Fig. 5.4). The effect of increasing treatment time follows the same trend of increasing applied power.

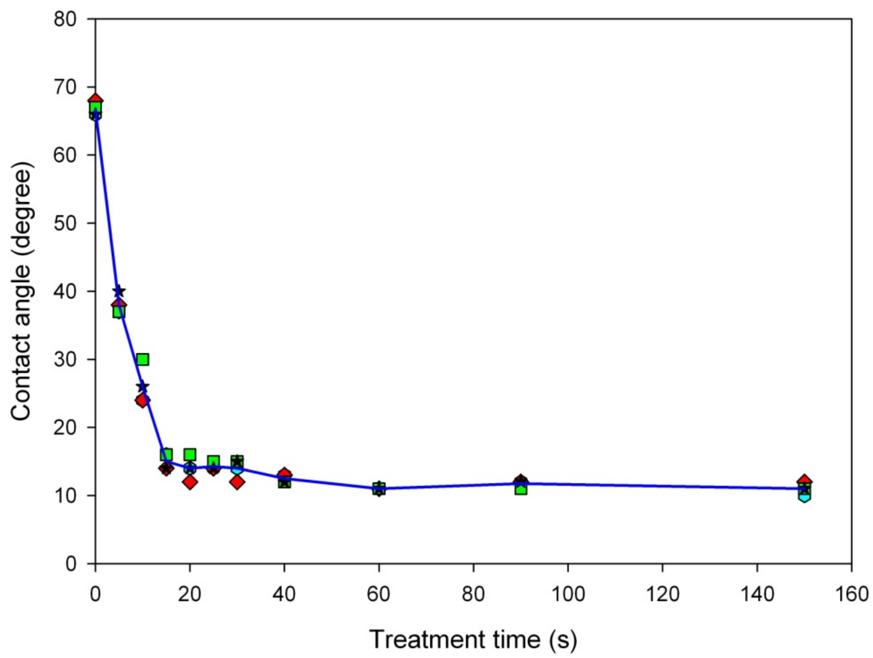


**Figure 5.3** Water contact angle on ITO surface as a function of treatment time.

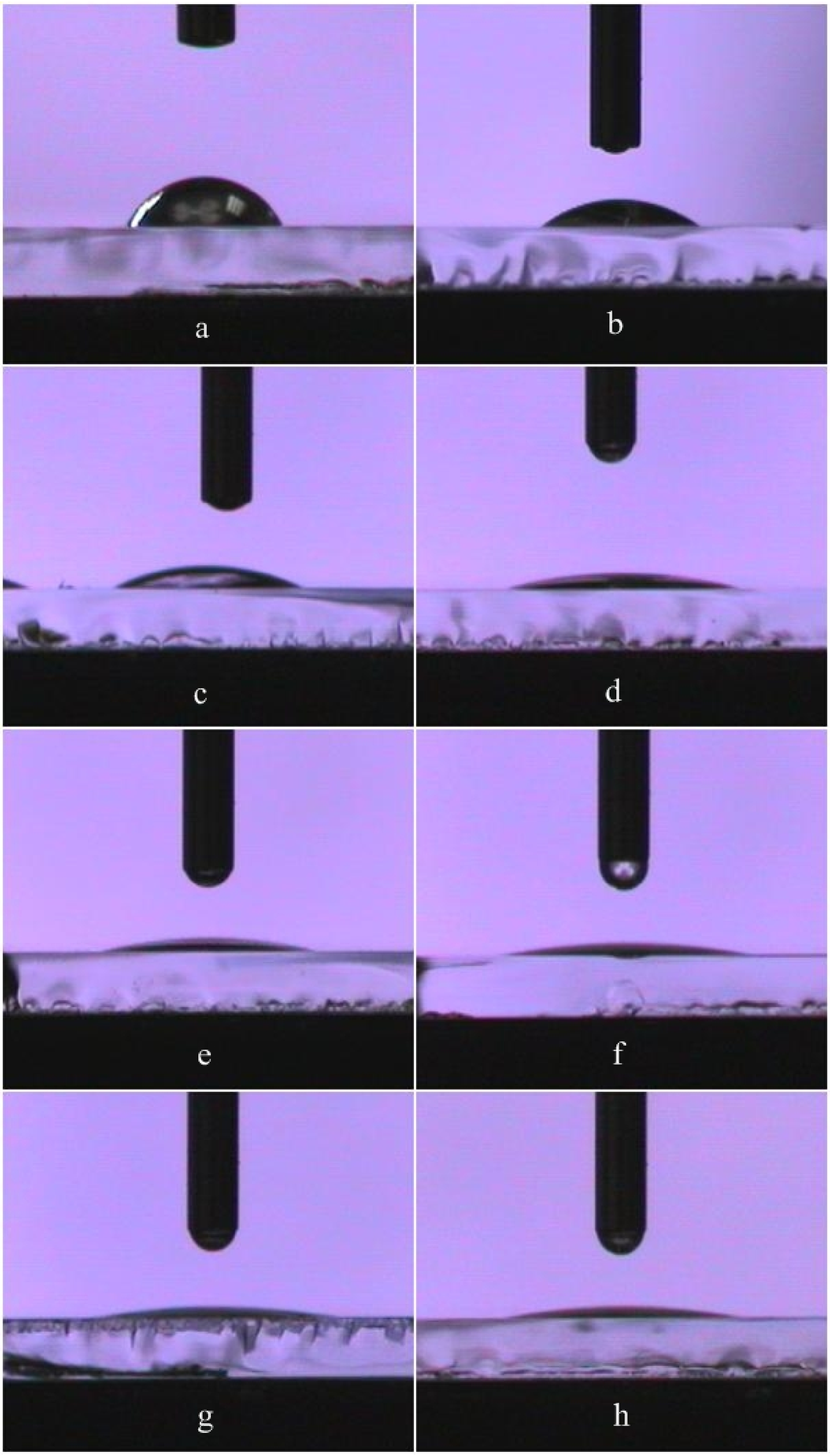


**Figure 5.4** Photographs of water drop after plasma treatment for (a) 0 s (b) 5 s (c) 10 s (d) 15 s (e) 20 s (f) 40 s (g) 90 s (h) 150 s.

This effect of plasma on ITO thin films surface is believed to result from the removal of hydrocarbon contaminants on ITO surface [9, 35, 36, 38] and the attachment of radical species present in our argon plasma system [39]. One of the radical species is OH radical as suggested by the OES of argon.

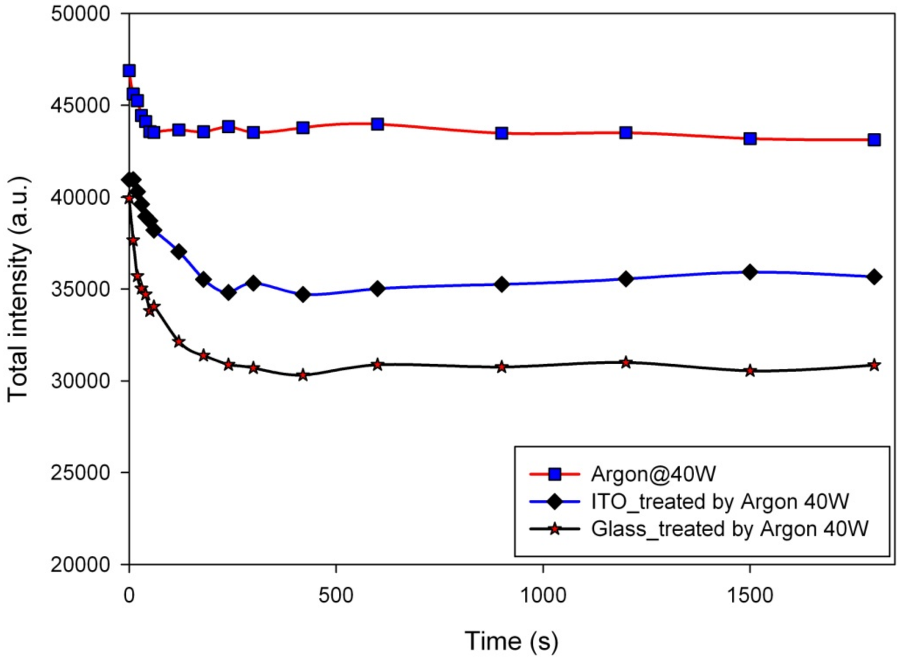


**Figure 5.5** OH peak intensities during the 40 W argon plasma treatment (top) without specimen, (middle) with ITO-coated glass specimen, (bottom) with glass specimen.

As already discussed under the OES result of argon in Chapter 5, the strong OH peak at 309.0 nm is from water vapor contaminating in the plasma. One percent of water vapor concentration by volume corresponds to relative humidity (RH) of approximately 30% at 300 K and 1 atm [39]. The OH peak is assumed to have Gaussian shape and fitted with ORIGIN 8.0. The areas under OH peak or its total intensity of all samples are shown in Fig. 5.5. Assuming ITO thin film does not chemically react with argon plasma, decrement of OH intensity during treating ITO with respect to the original thin film signifies the consumption of OH radical on surface of ITO thin film. This reaction consequently increases the ITO surface energy. The same effect is expected on the bare glass surface too. The reduction of OH peak under treatment with ITO or glass comparing to that of pure argon, implies that OH radicals are attached at ITO or glass surface. The OH peak at the presence of ITO or glass decrease exponentially at the first five minutes and become stable afterwards.

## 5.2 Tapioca Starch Modification

Starches can be modified to change their functionality. The common starch modification is using chemical agents. As a consequence, this chemical may be left in starch molecules and may be harmful if accumulated in human. Plasma treatment become of interest as an alternative to modify starch, especially atmospheric plasma due to its affordable cost, its flexibility to apply in several industrial scales and without involving any chemical agents.

Tapioca starch powder was pressed to a tablet of 16 mm in diameter and about 1 mm thick by hydraulic presser. Typical weight for a tablet is 270−280 mg. The starch tablets were treated under the atmospheric argon plasma. In this work, the starch tablets were treated at 40 watts of plasma power and for 30 minutes. Before treating, plasma chamber is purged by argon flow for two minutes with the same reason of ITO treatment. The OES of starch treated by atmospheric argon plasma is also measured as a first investigation (see Fig. 5.6). The interesting peak is also OH peak at 309.0 nm but in this case this peak of starch treated by argon is more than that of pure argon. The area under OH peak is also calculated as seen in Fig. 5.7 and also compare with that of ITO treated by argon. The additional OH is believed to come from plasma-induced cross linking process as follow;

$$Starch - OH \ + \ OH - Starch \xrightarrow{Plasma} Starch - O - Starch \ + \ H_2O$$

For each cross linking reaction, one hydrogen atom (H) and one OH radical are extracted from two carbohydrate chains [76]. However, both species quickly recombine to form a water molecule. The height of OH peak can be used as a rough measure of cross-linking process. From Fig. 5.7, it can be concluded that the cross-linking rate is highest at the beginning and slowing down at the later stage. The result from cross-linking process can be investigated by scanning electron microscope (SEM Model S-2500 Hitachi, Japan). The granule size and their morphology are changed obviously as shown in Fig. 5.8. Each granule lost their edge sharpness and linked to the neighbor granules.

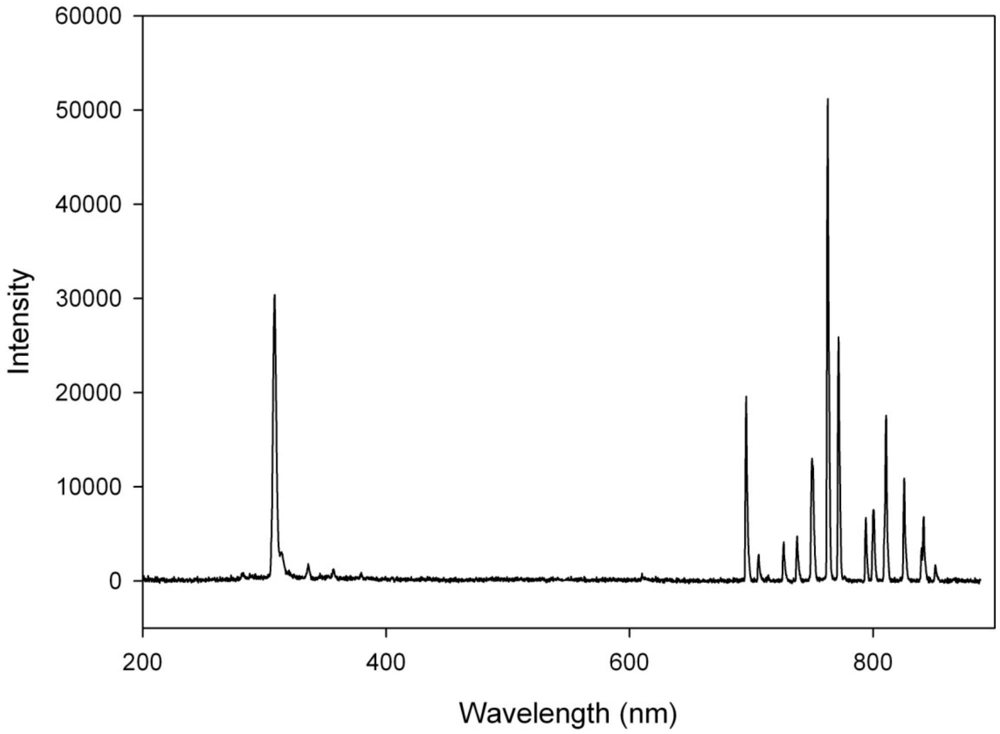


**Figure 5.6** OES of starch treated by argon 40W at the beginning.

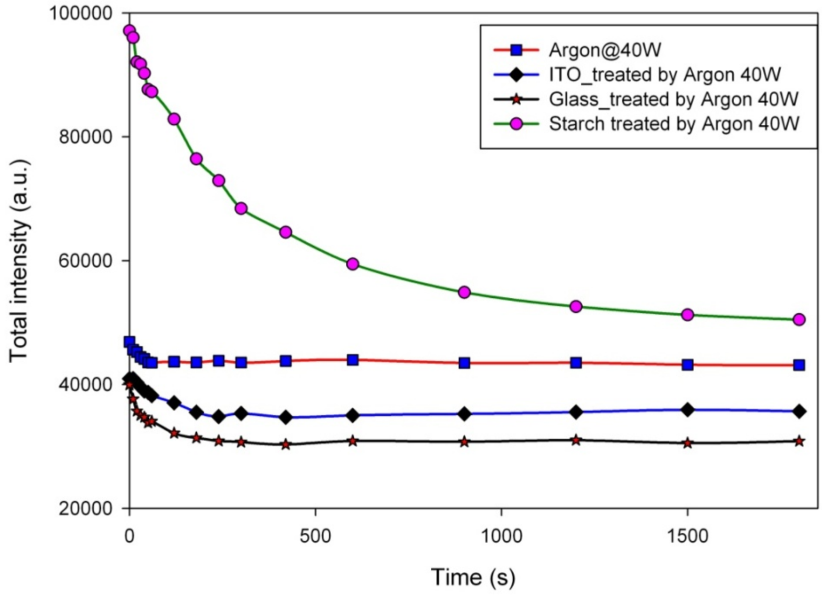


**Figure 5.7** Area under OH peak of starch treated by argon 40W comparing with result in Figure 5.5.

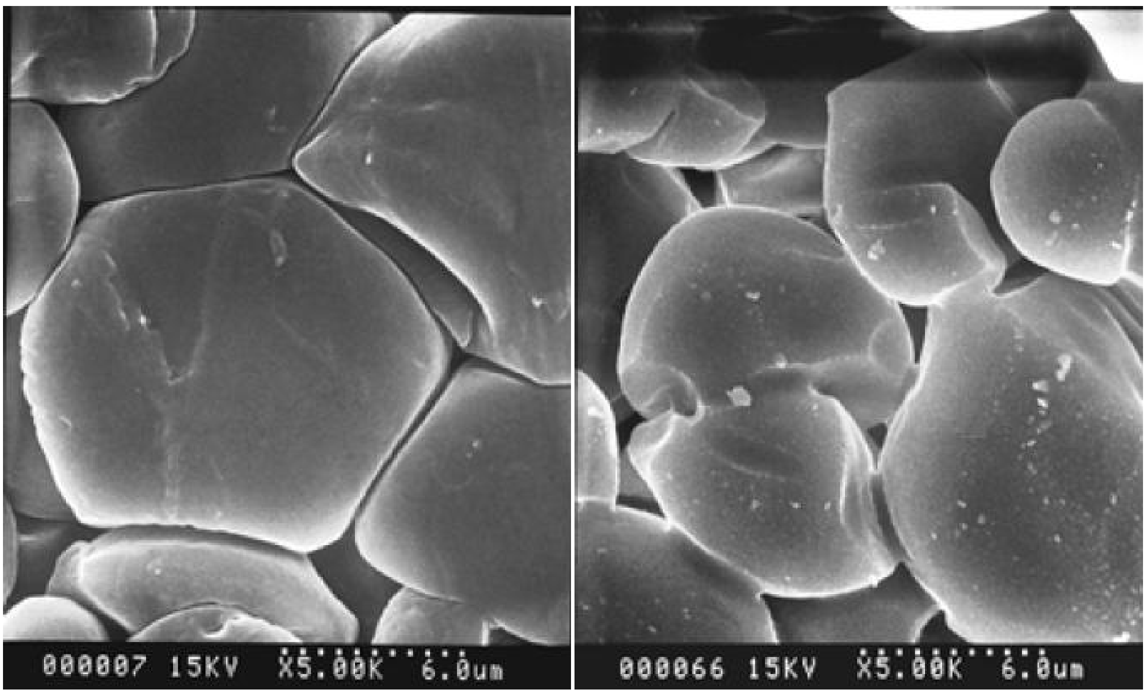


**Figure 5.8** Scanning electron micrographs (magnification 5,000×) of starch (left) before and (right) after atmospheric argon plasma treatment.

# CHAPTER VI
# CONCLUSION

As seen in this work, the atmospheric plasma system has been developed. The system consists of a high voltage medium frequency power supply, a plasma chamber and a gas flow controller. The power supply circuit and PCB layout are also design as a prototype. However, this circuit is designed for experimental purpose so it has many parts to ensure safety operation at wide range. The frequency of power supply is chosen at 17 kHz to avoid audible noise from electronic switching. This power supply can supply up to 17 $kV_{p-p}$. Argon and helium require only a few $kV_{p-p}$ for their breakdown voltage. The power supply is designed to supply DC power up to 150 watts (0-130 VDC and 0.0-1.2 Amp from DC power supply). The overcurrent protection is built-in in the converter. In case of malfunction, a fuse will be blown up. The power controller is designed to stabilize plasma power to not harm dielectric barrier. The plasma chamber with air cooling can be operated for several hours without any damage to the dielectric. Some test, e.g., starch treatment experiments have been come out to verify. The chamber is also equipped with OES channel for characterization purpose. Gas flow controller reduces the gas consumption rate. Two or more gas flow controllers maybe applied to mix different gases together.

In Chapter 4, the atmospheric plasma generation is demonstrated using several gases, e.g., argon, helium, air and nitrogen. Their properties are analyzed and characterized by voltage-current measurement, *Lissajous Figure* and OES. The first two characterizations are used to identify, i.e., the homogenous plasma type from the filamentary plasma one. The homogeneous plasma can be further classified into 2 modes as well which are APGD and APTD modes (see Chapter 4). OES is used to characterize and identify active species presenting in each atmospheric plasma.

Chapter 5 shows the plasma effects and some applications. ITO thin films are used as test samples to investigate the effects of plasma treatment time on contact angle of water on ITO surface. The treatment, which may lead to the removal hydrocarbon contaminants and the attachment of OH radical onto ITO surface, causes the contact angle to decrease. In addition, tapioca starch has been used to demonstrate the modification by atmospheric argon plasma. The cross-linking between carbohydrate chains is initiated by argon plasma. The increasing of OH peak of starch treatment comparing to pure argon plasma at the same power is believed to come from water vapor extracting from cross-linking process.

**Outlook**

- To achieve homogenous plasma, thickness of dielectric barrier has to be reduced. The electrode coated with high *k* dielectric film may give better plasma properties and give wider space gap.
- Some radicals from $SF_6$, $O_2$ and some hydrocarbon gases can better improve material properties. However, in atmospheric plasma operation, adding such gases can cause filamentary discharge or plasma extinction.
- Atmospheric nitrogen plasma can be ignited in homogenous mode [28, 29, 54, 55]. Argon and helium can be replaced by nitrogen which its cost is lower.
- Many applications are well suited for AP, e.g., cell treatment [77], textile improvement [40-43], flat material activation [33-36], and etc. AP can be applied to these applications in industrial level by using moving conveyor or moving electrode for large area treatment.

# REFERENCES

1. D.L. Smith (1995). Thin-Film Deposition Principle and practice. *McGraw-Hill, Inc.*
2. S.C. Tang, S.Y.R. Hui, & H. Chung. (1999). A Naturally Soft-switched High-Frequency Gate Drive Circuit for Power MOSFETs/IGBTs. *IEEE 1999 Inter. Conf. on Power Electronics and Drive Systems,* PEDS'99, Hong Kong.
3. G. Ivensky, L. Zeltser, A. Kats, & S.B. Yaakov. (1996). Reducing IGBT Losses in ZCS Series Resonant Converters. *IEEE Appl. Power Elect. Conf. (APEC'96),* 475-481.
4. M. Qiu, P.K. Jain, & H. Zhang. (2004). An APWM Resonant Inverter Topology for High Frequency AC Power Distribution Systems. *IEEE Trans. on Power Elect.*, **19**, 121-129.
5. J. Park, I. Henins, H.W. Herrmann, & G.S. Selwyn. (2001). Gas breakdown in an atmospheric pressure radio-frequency capacitive plasma source. *J. Appl. Phy*, **89**, 15-19.
6. U. Kogelschatz. (2003). Dielectric-barrier Discharges: Their History, Discharge Physics, and Industrial Applications. *Plasma Chemistry and Plasma Processing*, **23**, 1-46.
7. U. Kogelschatz. (2004). Atmospheric-pressure plasma technology. *Plasma Phys. Control. Fusion*, **46**, B63–B75.
8. H. Conrads, & M. Schmidt. (2000). Plasma generation and plasma sources. *Plasma Sources Sci. Technol*, **9**, 441–454.
9. E.S. Lee, J.H. Choi, & H.K. Baik. (2007). Surface cleaning of indium tin oxide by atmospheric air plasma treatment with the steady-state airflow for organic light emitting diodes *Surface & Coatings Technology*, **201**, 4973–4978.
10. D.H. Shin, C.U. Bang, J.H. Kim, K.H. Han, Y.C. Hong, H.S. Uhm, D.K. Park, & K.H. Kim. (2007). Modification of metal surfaces by microwave plasma at atmospheric pressure. *Surface & Coatings Technology*, **201**, 4939–4942.

11. Y.P. Raizer. (1991). Gas discharge physics. *Springer-Verlag*, ISBN 3-540-19462-2.

12. A. Fridman, A. Chirokov. & A. Gutsol. (2005). Non-thermal atmospheric pressure discharges. *J. Phys. D: Appl. Phys*., **38**, R1–R24.

13. A. Mizuno. (2007). Industrial applications of atmospheric non-thermal plasma in environmental remediation. *Plasma Phys. Control. Fusion*, **49**, A1–A15

14. A.L. Peratt. (1966). Advances in Numerical Modeling of Astrophysical and Space Plasmas. *Astrophysics and Space Science*, **242**, 93–163.

15. J.R. Roth, J. Rahel, X. Dai, & D.M. Sherman. (2005). The physics and phenomenology of One Atmosphere Uniform Glow Discharge Plasma (OAUGDP™) reactors for surface treatment applications. *J. Phys. D: Appl. Phys.*, **38**, 555–567.

16. M.S. Naidu, & V. Kamaraju. (1995). High Voltage Engineering, 2nd edition, *McGraw Hill*, ISBN 007-62286-2.

17. M.R. Radjenovic, & J.K. Lee. (2005). Modeling of breakdown behavior in radio-frequency argon discharges with improved secondary emission model. *PHYSICS OF PLASMAS*, **12**, 063501.

18. L.X. Chen, L.Z. Hui, J.P. Ying, L.L. Chun, Y.Z. Qian & D.L. Fang. (2007). Study on the transition from filamentary discharge to diffuse discharge by using a dielectric barrier surface discharge device. *Chinese Phys.*, **16** (10), 3016-3021.

19. M. Konuma. (2005). Plasma techniques for film deposition, *Alpha Science Interenational Ltd*, Harrow, UK.

20. S. Okazaki, M. Kogoma, M. Uehara, & Y. Kimura. (1993). Appearance of stable glow discharge in air, argon, oxygen and nitrogen at atmospheric pressure using a 50 Hz source. *J. Phys. D Appl. Phys*, **26**, 889-892**.**

21. Y.B. Golubovskii, V.A. Maiorov, P. Li, & M. Lindmayer. (2006). Effect of the barrier material in a Townsend barrier discharge in nitrogen at atmospheric pressure. *J. Phys. D: Appl. Phys.*, **39**, 1574–1583.

22. R. Brandenburg, Z. Navrátil, J. Jánskỳ, P. St’ahel, D. Trunec, & H-E. Wagner. (2009). The transition between different modes of barrier discharges at atmospheric pressure. *J. Phys. D: Appl. Phys.*, **42**, 085208.

23. Z. Fang, J. Lin, X. Xie, Y. Qiu & E. Kuffel. (2009). Experimental study on the transition of the discharge modes in air dielectric barrier discharge. *J. Phys. D: Appl. Phys.*, **42**, 085203.

24. Z. Fang, Y. Qiu, C. Zhang & E. Kuffel. (2007). Factors influencing the existence of the homogeneous dielectric barrier discharge in air at atmospheric pressure. *J. Phys. D: Appl. Phys*., **40**, 1401-1407.

25. S.Y. Moon, & W. Choe. (2004). A uniform glow discharge plasma source at atmospheric pressure. *Appl. Phys. Lett.*, **84** (2), 188-190.

26. B. Eliasson, & U. Kogelschatz. (1991). Non-equilibrium volume plasma chemical processing. *IEEE Trans. Plasma Sci,*, **19**, 1063.

27. F. Massines, A. Rabehi, P. Decomps, R.B. Gadri, P. Ségur, & C. Mayoux. (1998). Experimental and theoretical study of a glow discharge at atmospheric pressure controlled by dielectric barrier. *J. Appl. Phys*., **83**, 2950-2956.

28. F. Massines, P. Ségur, N. Gherardi, C. Khamphan, & A. Ricard. (2003). Physics and chemistry in a glow dielectric barrier discharge at atmospheric pressure: diagnostics and modeling. *Surface and Coatings Technology*, **174 –175**, 8–14.

29. F. Massines, N. Gherardi, N. Naudé, & P. Ségur. (2005). Glow and Townsend dielectric barrier discharge in various atmosphere. *Plasma Phys. Control. Fusion*, **47**, B577–B588.

30. P. Zhang, & U. Kortshagen. (2006). Two-dimensional numerical study of atmospheric pressure glows in helium with impurities. *J. Phys. D: Appl. Phys.*, **39**, 153–163

31. K.L. Bell, A. DALGARNO, & A.E. KINGSTON. (1968). Penning ionization by metastable helium atoms. *J. Phys. B: At. Mol. Phys.*, **1**, 18-22.

32. M. Araya, T.Yuji, T. Watanabe, J. Kashihara, & Y. Sumida. (2007). Application to cleaning of waste plastic surfaces using atmospheric non-thermal plasma jets. *Thin Solid Films*, **515**, 4301–4307.

33. Y. Chiba, K. Kashiwagi, & H. Kokai. (2004). Plasma surface treatment effect of $TiO_2$ thin film. *Vacuum*, **74**, 643–646.

34. G. Borcia, C.A. Anderson, & N.M.D. Brown. (2003). Dielectric barrier discharge for surface treatment: application to selected polymers in film and fibre form. *Plasma Sources Sci. Technol*, **12**, 335–344.

35. C.H. Yi, C.H. Jeong, Y.H. Lee, Y.W. Ko, & G.Y. Yeom. (2004). Oxide surface cleaning by an atmospheric pressure plasma. *Surface and Coatings Technology*, **177 –178**, 711–715.

36. Z.Z. You, & J.Y. Dong. (2006). Surface modifications of ITO electrodes for polymer light-emitting devices. *Applied Surface Science*, **253**, 2102–2107.

37. C. Wang, & X. He. (2006). Effect of atmospheric pressure dielectric barrier discharge air plasma on electrode surface. *Appl. Surf. Sci.*, **253**, 926–929.

38. K.S. Nam. H.J. Lee, S.H. Lee, G.H. Lee, Y.S. Song, & D.Y. Lee. (2006). The effect of an atmospheric pressure plasma treated MgO layer on the discharge performance of an AC plasma display panel. *Surface & Coatings Technology*, **201**, 2567–2572.

39. R. Dorai, & M.J. Kushner. (2003). A model for plasma modification of polypropylene using atmospheric pressure discharges. *J. Phys. D: Appl. Phys.*, **36**, 666-685.

40. T.H.C. Costa, M.C. Feitor, C. Alves Jr., P.B. Freire, C.M. de Bezerra. (2006). Effects of gas composition during plasma modification of polyester fabrics. *Journal of Materials Processing Technology*, **173**, 40-43.

41. J. J. Long, H.W. Wang, T.Q. Lu, R.C. Tang, & Y.W. Zhu. (2008). Application of Low-Pressure Plasma Pretreatment in Silk Fabric Degumming Process. *Plasma Chem Plasma Process*, **28**, 701-713.

42. N.D. Geyter, R. Morent, & C. Leys. (2006). Penetration of a dielectric barrier discharge plasma into textile structures at medium pressure. *Plasma Sources Sci. Technol.*, **15**, 78-84.

43. S. K. Hodak, T. Supasai, B. Paosawatyanyong, K. Kamlangkla, & V. Pavarajarn. (2008). Enhancement of the hydrophobicity of silk fabrics by $SF_6$ plasma. *Applied Surface Science*, **254**, 4744-4749.

44. M. Nisoa, D. Srinoum, & P. Kerdthongmee. (2005). Development of high voltage high frequency resonant inverter power supply for atmospheric surface glow barrier discharges. *Solid State Pheno.*, **107**, 81-85.

45. J. M. Alonso, J. Cardesín, E.L. Corominas, M.R. Secades, & J. García. (2004). Low Power High Voltage High Frequency Power Supply for Ozone Generation. *IEEE Trans. on Industry Applications*, **40** (2), 414-421.

46. J. M. Alonso, J. García, A.J. Calleja, J. Ribas, & J. Cardesín. (2005). Analysis, Design, and Experimentation of a High-Voltage Power Supply for Ozone Generation Based on Current-Fed Parallel-Resonant Push–Pull Inverter. *IEEE Trans. on Industry Applications*, **41** (5), 1364-1372.

47. http://focus.ti.com/lit/ml/slup169/slup169.pdf. August 11, 2006.

48. http://focus.ti.com/lit/ml/slup126/slup126.pdf. August 11, 2006.

49. http://focus.ti.com/lit/ml/slup127/slup127.pdf. May 16, 2006.

50. http://focus.ti.com/lit/ml/slup085/slup085.pdf. August 09, 2007.

51. http://focus.ti.com/lit/ml/slup089/slup089.pdf. August 09, 2007.

52. http://focus.ti.com/lit/ml/slup092/slup092.pdf. July 19, 2007.

53. http://focus.ti.com/lit/ml/slup123/slup123.pdf. August 11, 2006.

54. N. Naudé, J.P. Cambronne, N. Gherardi, & F. Massines. (2005). Electrical model and analysis of the transition from an atmospheric pressure Townsend discharge to a filamentary Discharge. *J. Phys. D: Appl. Phys.*, **38**, 530-538.

55. N. Gherardi, & F. Massines. (2001). Mechanisms Controlling the Transition from Glow Silent Discharge to Streamer Discharge in Nitrogen. *IEEE Trans. Plasma Sci*, **29** (3), 536-544.

56. G. Nersisyan, & W.G. Graham. (2004). Characterization of a dielectric barrier discharge operating in an open reactor with flowing Helium. *Plasma Sources Sci. Technol.*, **13**, 582-587.

57. Z. Falkenstein, & J.J. Coogan. (1997). Microdischarge behaviour in the silent discharge of nitrogen - oxygen and water - air mixtures. *J. Phys. D: Appl. Phys.*, **30**, 817-825.

58. H.E. Wagner, R. Brandenburg, K.V. Kozlov, A. Sonnenfeld, P. Michel, & J.F. Behnke. (2003). The barrier discharge: basic properties and applications to surface treatment. *Vacuum*, **71**, 417-436.

59. Y. Zhang, X.H. Wen, & W.H. Yang. (2007). Excitation temperatures of atmospheric argon in dielectric barrier discharges. *Plasma Sources Sci. Technol.*, **16**, 441-447.

60. D.L. Crintea, U. Czarnetzki, S. Iordanova, I. Koleva, & D. Luggenhölscher. (2009). Plasma diagnostics by optical emission spectroscopy on argon and comparison with Thomson scattering. *J. Phys. D: Appl. Phys*., **42**, 045208.

61. E. Wagenaars, R. Brandenburg, W.J.M. Brok, M.D. Bowden, & H.E. Wagner. (2006). Experimental and modeling investigations of a dielectric barrier discharge in low-pressure argon. *J. Phys. D: Appl. Phys*., **39**, 700–711.

62. O. Goossensa, E. Dekempeneer, D. Vangeneugden, R.V. de Leest, & C. Leys. (2001). Application of atmospheric pressure dielectric barrier discharges in deposition, cleaning and activation. *Surface and Coatings Technology*, **142-144**, 474-481.

63. H. Luo, Z. Liang, X. Wang, Z. Guan, & L. Wang. (2008). Effect of gas flow in dielectric barrier discharge of atmospheric helium. *J. Phys. D: Appl. Phys*., **41**, 205205.

64. Z. Navrátil, R. Brandenburg, D. Trunec, A. Brablec, P. St'ahel, H.E. Wagner, & Z. Kopeckỳ. (2006). Comparative study of diffuse barrier discharges in neon and helium. *Plasma Sources Sci. Technol*., **15**, 8–17.

65. F. Massines, & G. Gouda. (1998). A comparison of polypropylene-surface treatment by filamentary, homogeneous and glow discharges in helium at atmospheric pressure. *J. Phys. D: Appl. Phys.*, **31**, 3411–3420.

66. A.A. Garamoon, & D.M. El-zeer. (2009). Atmospheric pressure glow discharge plasma in air at frequency 50 Hz. *Plasma Sources Sci. Technol.*, **18**, 045006.

67. D. Staack, B. Farouk, A. Gutsol, & A. Fridman. (2005). Characterization of a dc atmospheric pressure normal glow discharge. *Plasma Sources Sci. Technol*., **14**, 700–711.

68. V. Zengina, A. Gökmen, S. Dincer, & S. Süzer. (1995). HIGH-VOLTAGE OPTICAL EMISSION IN BINARY GASEOUS MIXTURES OF $N_2$. *Journal of Molecular Structure*, **349**, 17-20.

69. F. Liu, W. Wang, S. Wang, W. Zheng, & Y. Wang. (2007). Diagnosis of OH radical by optical emission spectroscopy in a wire-plate bi-directional pulsed corona discharge. *Journal of Electrostatics*, **65**, 445–451.

70. J. H. Choi, T.I. Lee, I. Han, H.K. Baik, K.M. Song, Y.S. Lim, & E. S. Lee. (2006). Investigation of the transition between glow and streamer discharges in atmospheric air. *Plasma Sources Sci. Techno*l., **15**, 416–420.

71. T. Martens, W. J. M. Brok, J. V. Dijk, & A. Bogaerts. (2009). On the regime transitions during the formation of an atmospheric pressure dielectric barrier glow discharge. *J. Phys. D: Appl. Phys*., **42**, 122002.

72. J. Shin, & L.L. Raja. (2003). Dynamics of pulse phenomena in helium dielectric-barrier atmospheric-pressure glow discharges. *J. Appl. Phys*., **94** (12), 7408-7415.

73. I. Radu, R. Bartnikas, & M.R. Wertheimer. (2003). Frequency and Voltage Dependence of Glow and Pseudoglow Discharges in Helium Under Atmospheric Pressure. *IEEE Trans. Plasma Sci.*, **31** (6), 1363-1378.

74. L. Peng, Z. Ru-juan, W. Xiao-hui, Z. Xiao-dong, L. Ding. (2002). An Experimental Study on Atmospheric Pressure Glow Discharge in Different Gases. *Plasma Sci. Technol.*, **4**, 1323-1328.

75. Y.B. Golubovskii, V.A. Maiorov, J. Behnke, & J.F. Behnke. (2003). Modelling of the homogeneous barrier discharge in helium at atmospheric pressure. *J. Phys. D: Appl. Phys*., **36**, 39–49.

76. S. Förster, C. Mohr, & W. Viöl. (2005). Investigations of an atmospheric pressure plasma jet by optical emission spectroscopy, *Surfaces & Coatings Technology*, **200**, 827- 830.

77. http://plasma.mem.drexel.edu/announcements/documents/FRIDMAN-bioappsofplasma.pdf. October 12, 2009.

# APPENDICES

# APPENDIX A

# CIRCUITS

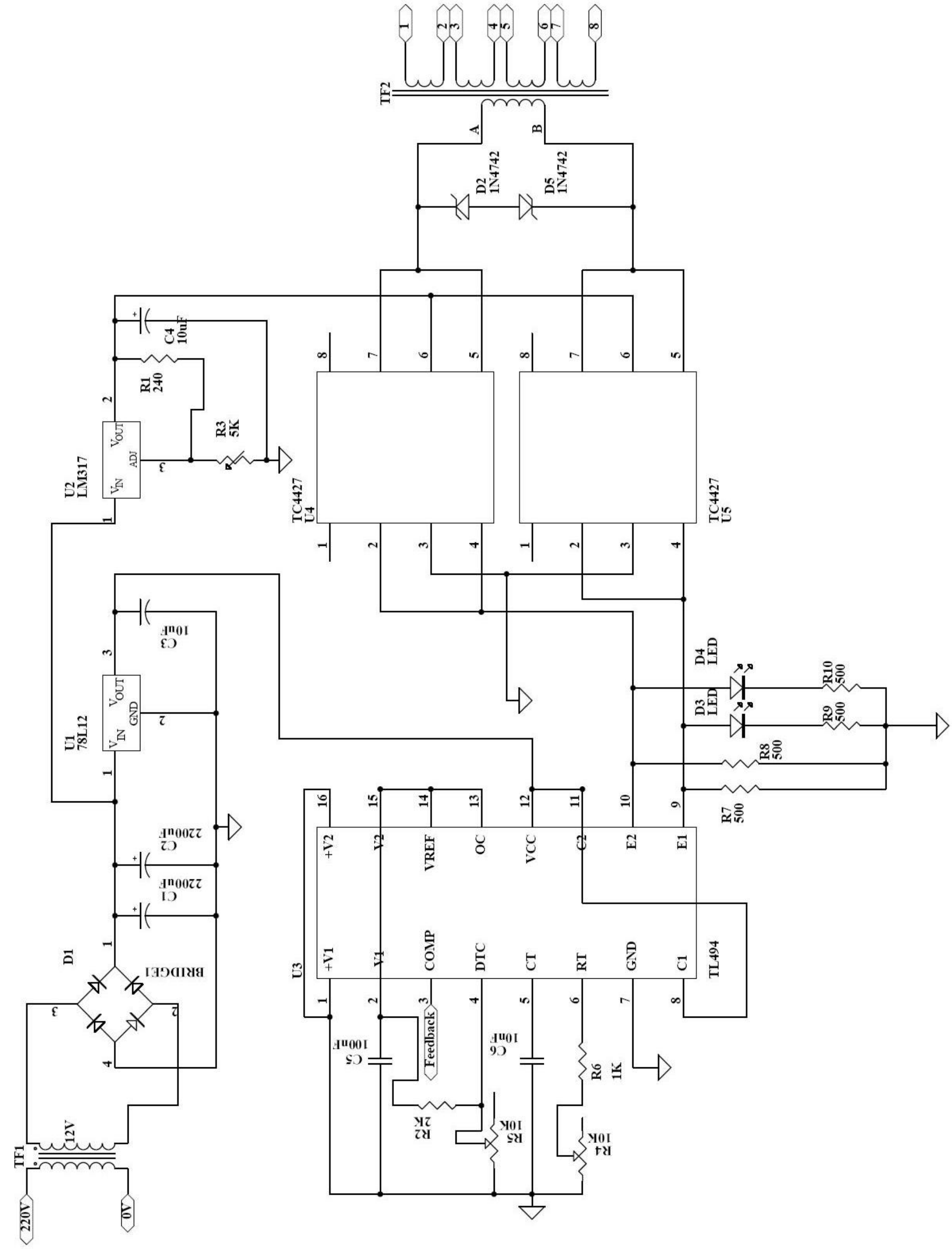


**Figure A1** TL494 controller circuit including TC4427 gate driver.

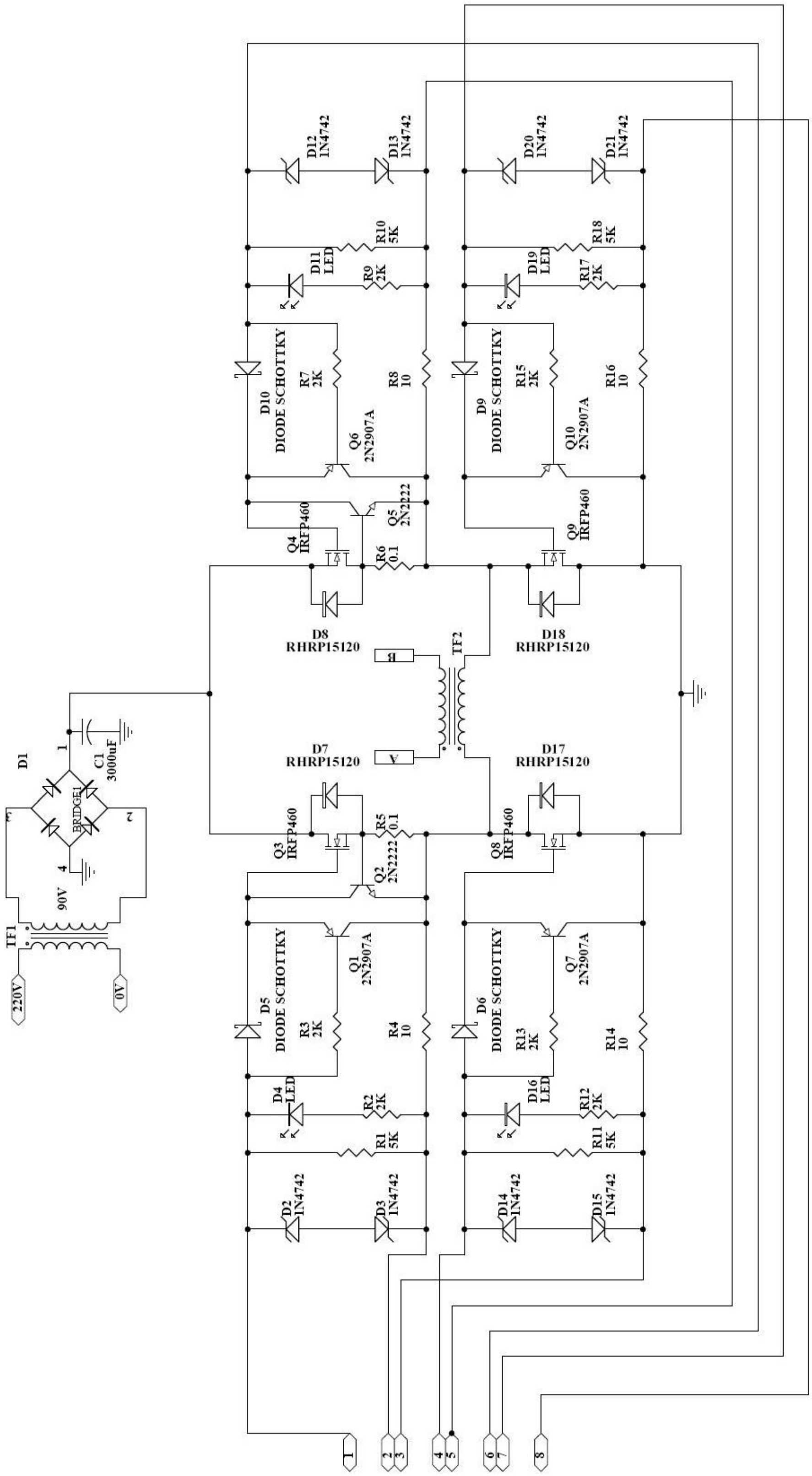


**Figure A2** Full bridge converter driven by gate drive circuit receiving signals from gate drive transformer and TL494 controller circuit.

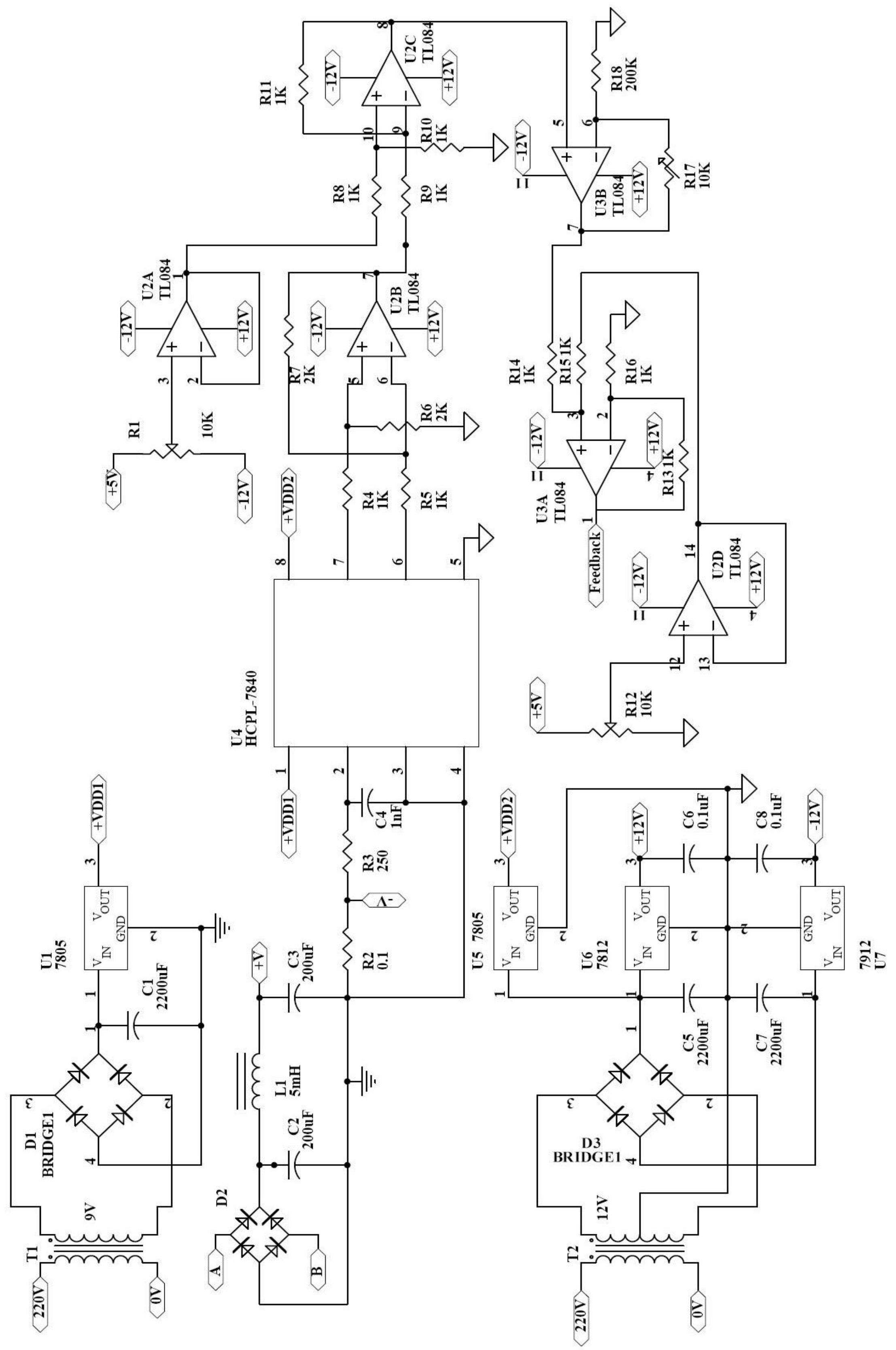


**Figure A3** A feedback controller circuit.

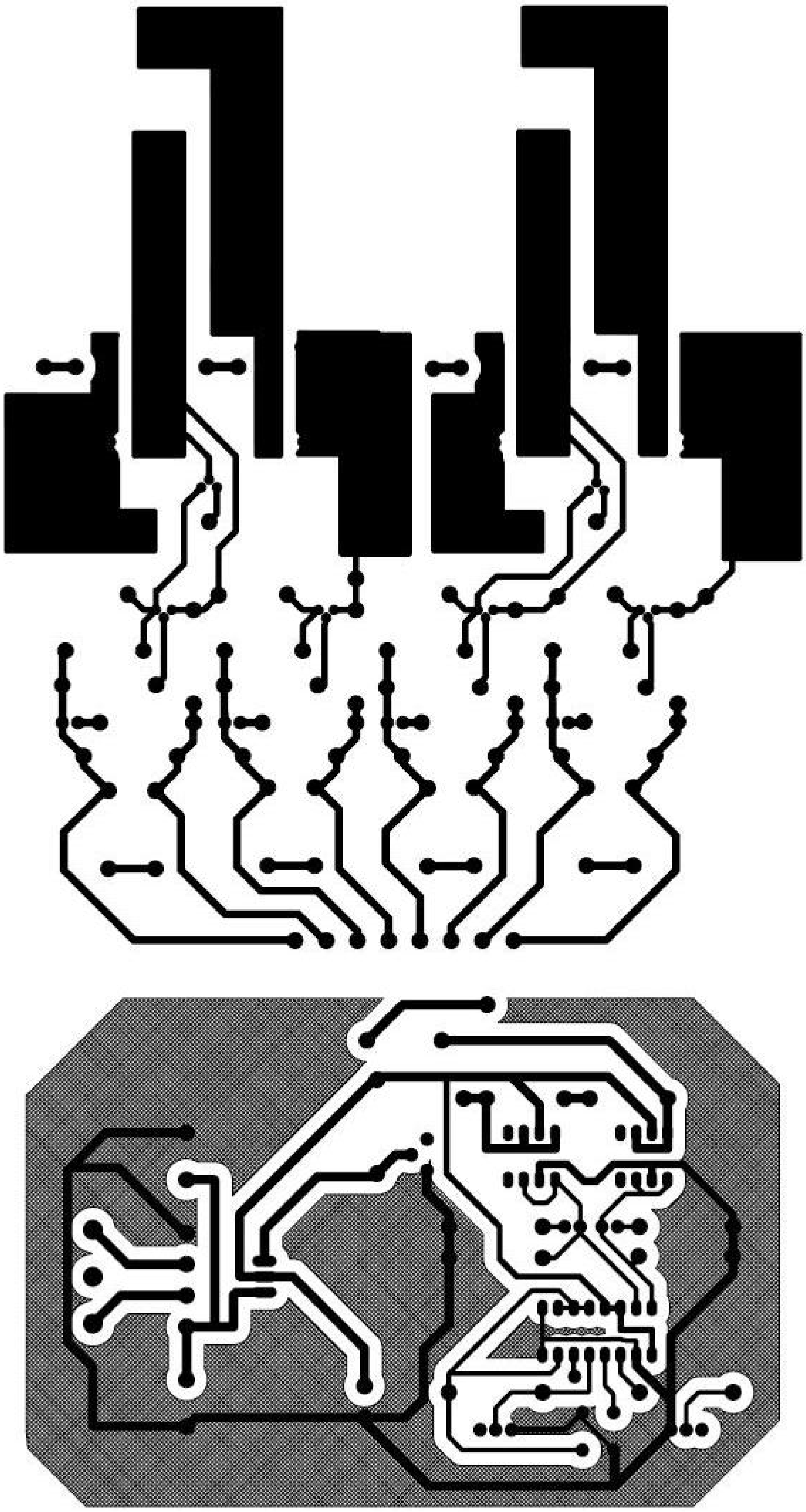

**Figure A4** Power controller and medium frequency inverter PCB.

# APPENDIX B

# DATASHEETS

## IRFP460

### N - CHANNEL 500V - 0.22 Ω - 20 A - TO-247 PowerMESH™ MOSFET

| TYPE | $V_{DSS}$ | $R_{DS(on)}$ | $I_D$ |
|---|---|---|---|
| IRFP460 | 500 V | < 0.27 Ω | 20 A |

- TYPICAL $R_{DS(on)}$ = 0.22 Ω
- EXTREMELY HIGH dv/dt CAPABILITY
- 100% AVALANCHE TESTED
- VERY LOW INTRINSIC CAPACITANCES
- GATE CHARGE MINIMIZED

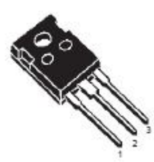


TO-247

**DESCRIPTION**

This power MOSFET is designed using the company's consolidated strip layout-based MESH OVERLAY™ process. This technology matches and improves the performances compared with standard parts from various sources.

**APPLICATIONS**

- HIGH CURRENT SWITCHING
- UNINTERRUPTIBLE POWER SUPPLY (UPS)
- DC/DC COVERTERS FOR TELECOM, INDUSTRIAL, AND LIGHTING EQUIPMENT.

**INTERNAL SCHEMATIC DIAGRAM**

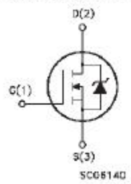


**ABSOLUTE MAXIMUM RATINGS**

| Symbol | Parameter | Value | Unit |
|---|---|---|---|
| $V_{DS}$ | Drain-source Voltage ($V_{GS}$ = 0) | 500 | V |
| $V_{DGR}$ | Drain- gate Voltage ($R_{GS}$ = 20 kΩ) | 500 | V |
| $V_{GS}$ | Gate-source Voltage | ± 20 | V |
| $I_D$ | Drain Current (continuous) at $T_c$ = 25 °C | 20 | A |
| $I_D$ | Drain Current (continuous) at $T_c$ = 100 °C | 13 | A |
| $I_{DM}$(•) | Drain Current (pulsed) | 80 | A |
| $P_{tot}$ | Total Dissipation at $T_c$ = 25 °C | 250 | W |
| | Derating Factor | 2 | W/°C |
| dv/dt(1) | Peak Diode Recovery voltage slope | 3.5 | V/ns |
| $T_{stg}$ | Storage Temperature | -65 to 150 | °C |
| $T_j$ | Max. Operating Junction Temperature | 150 | °C |

(•) Pulse width limited by safe operating area (1) $I_{SD} \leq 20$ A, di/dt ≤ 160 A/µs, $V_{DD} \leq V_{(BR)DSS}$, $T_j \leq T_{JMAX}$

September 1998 1/8

**Figure B1** IRFP460 MOSFET specification.

EPCOS

## U 93/76/30 cores

## UI 93/104/30 cores B67345

- For power transformers >1 kW (20 kHz)

**Magnetic characteristics** (per set)

| | UU 93/152/30 | UI 93/104/30 | |
|---|---|---|---|
| $\Sigma l/A$ | 0.42 | 0.31 | $mm^{-1}$ |
| $l_e$ | 354 | 258 | mm |
| $A_e$ | 840 | 840 | $mm^2$ |
| $A_{min}$ | 840 | 840 | $mm^2$ |
| $V_e$ | 297000 | 217000 | $mm^3$ |
| m | 1500 | 1100 | g/set |

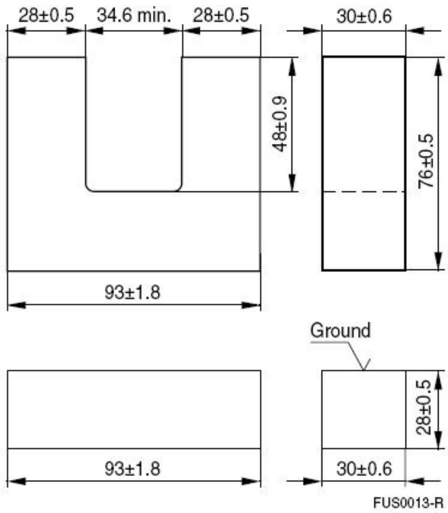


U and I cores are supplied as single units. The $A_L$ value in the table applies to a core set comprising two ungapped cores.

| Material | $A_L$ value nH | $\mu_e$ | $P_V$ W/set | Ordering code |
|---|---|---|---|---|
| Combination UU 93/152/30 | | | | |
| N27 | 5400 +30/–20% | 1800 | < 16 (100 mT, 25 kHz, 100 °C) | B67345B0001X027 |
| N87 | 5700 +30/–20% | 1900 | < 5.5 (100 mT, 25 kHz, 100 °C) | B67345B0001X087 |
| Combination UI 93/104/30 | | | | |
| N27 | 7400 +30/–20% | 1850 | < 12 (100 mT, 25 kHz, 100 °C) | B67345B0001X027 (U)<br>B67345B0002X027 (I) |
| N87 | 7900 +30/–20% | 1930 | < 4 (100 mT, 25 kHz, 100 °C) | B67345B0001X087 (U)<br>B67345B0002X087 (I) |

**Figure B2** UU 93/152/30 ferrite core specification.

# APPENDIX C
# CHAMBER DRAWINGS

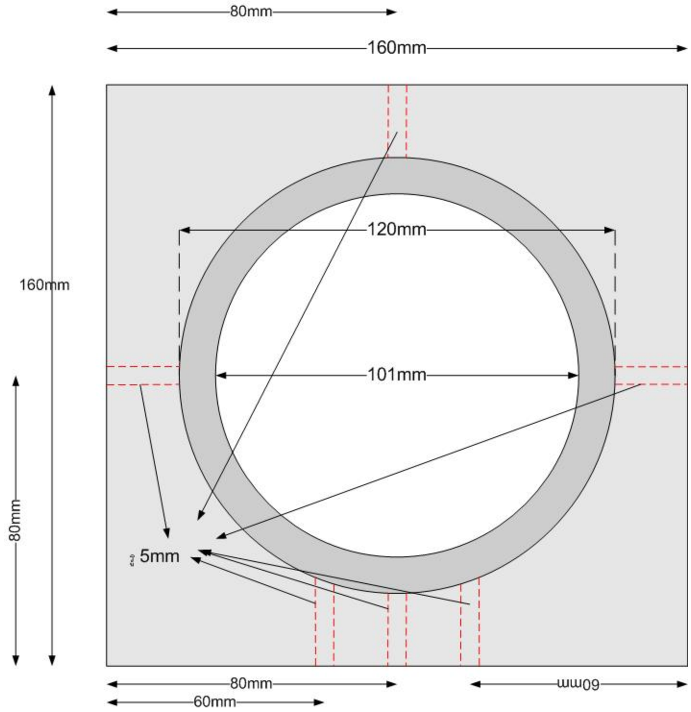


**Figure C1** Top view of new plasma chamber body and its dimension.

Acrylic

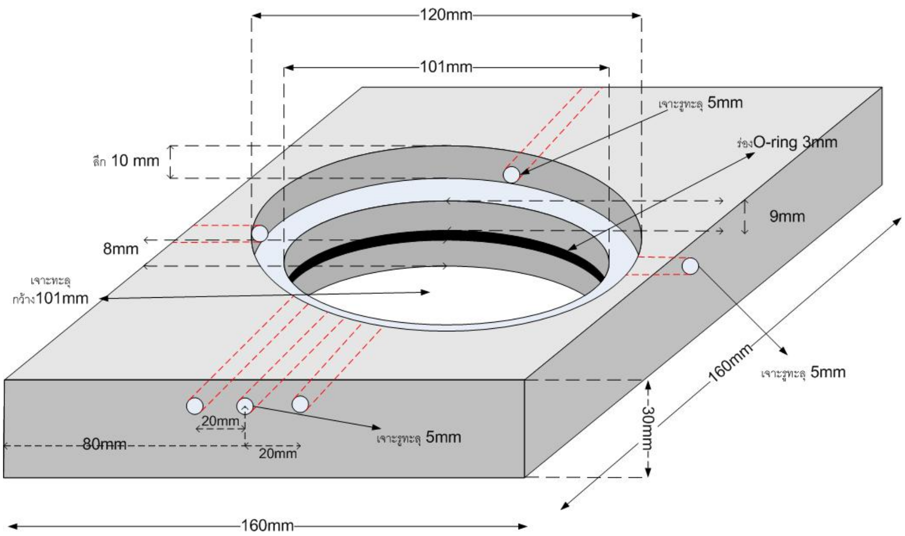


**Figure C2** Dimension of new plasma chamber body in perspective.

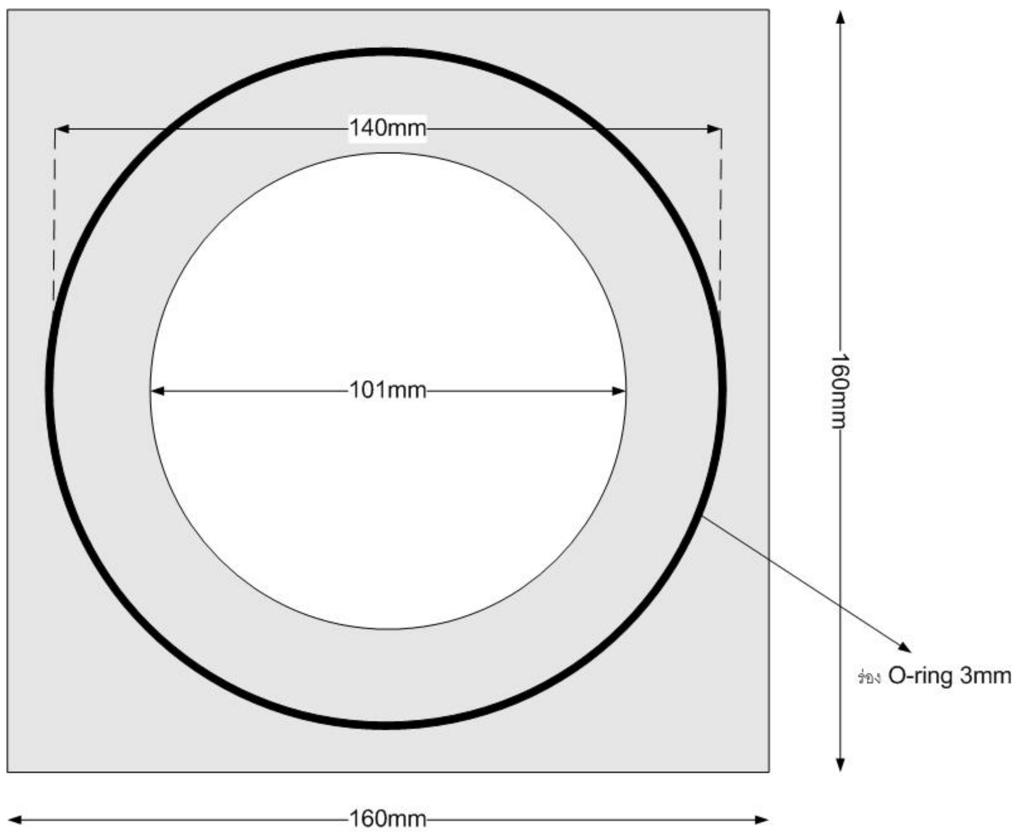


**Figure C3** Top view of plasma chamber cover and its dimension.

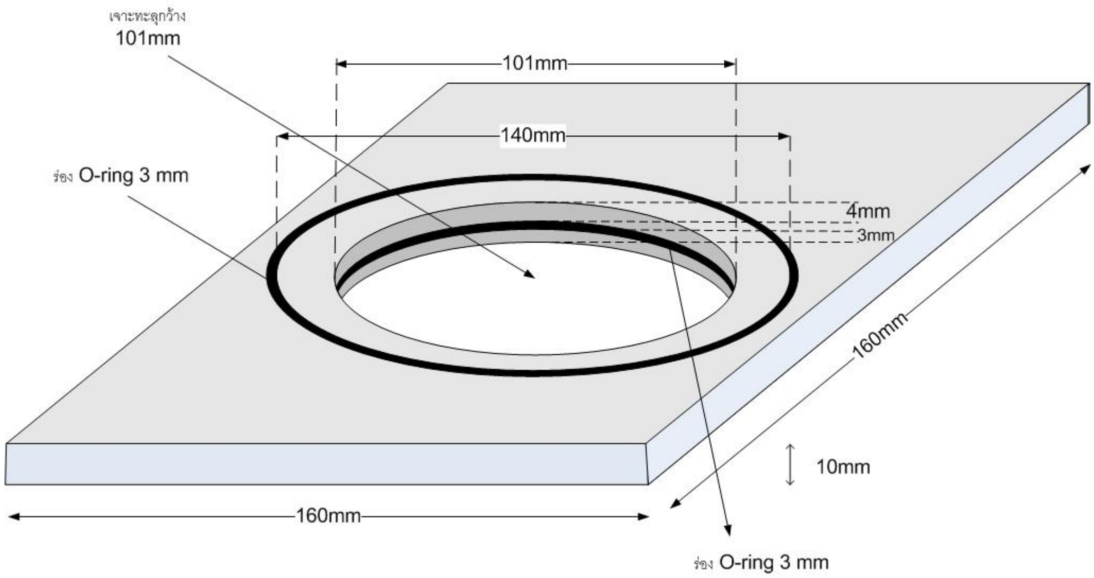


**Figure C4** Dimension of plasma chamber cover in perspective.

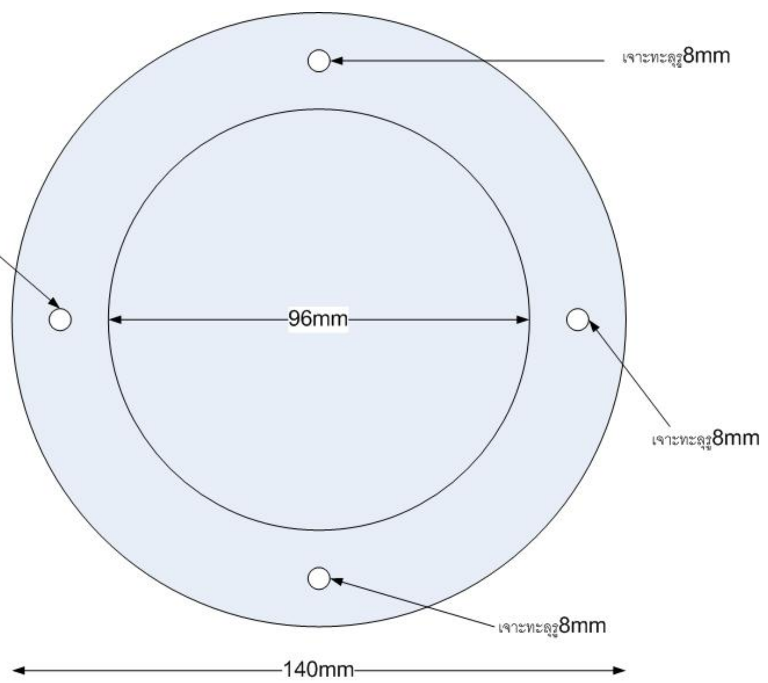


**Figure C5** Top view of power electrode and its dimension.

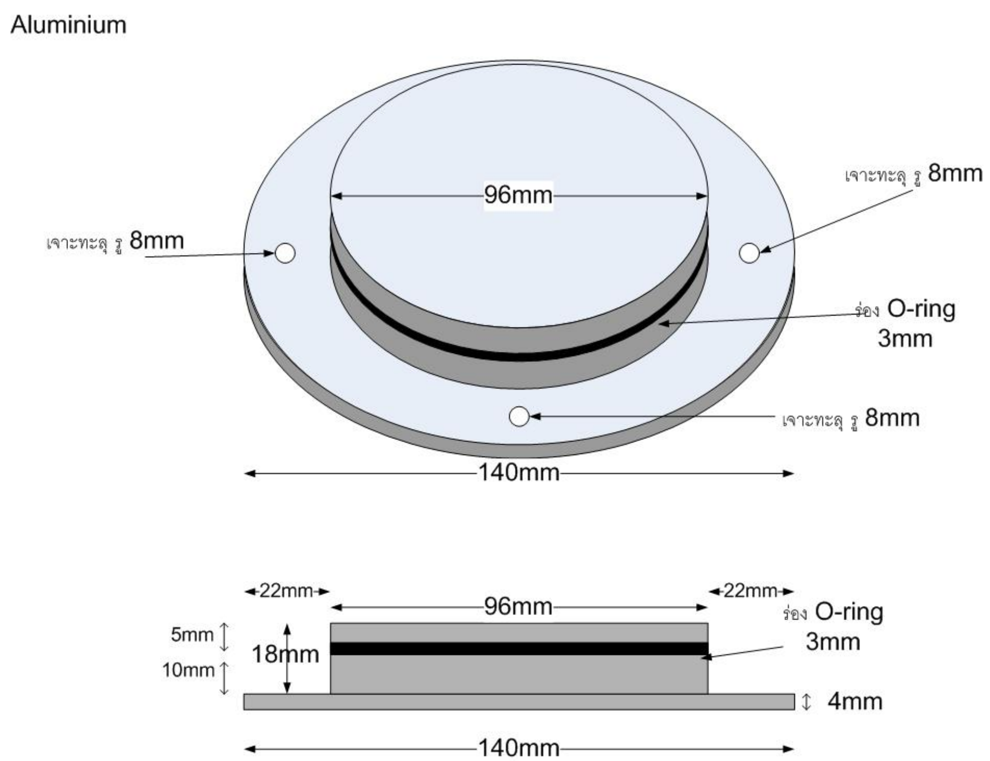


**Figure C6** Side and perspective view of power electrode and its dimension.

# BIOGRAPHY

| | |
|---|---|
| **NAME** | Mr. Pongsathon Jitsomboonmit |
| **DATE OF BIRTH** | 18 April 1984 |
| **PLACE OF BIRTH** | Nakhonphanom, Thailand |
| **INSTITUTIONS ATTENDED** | Mahidol University, 2002-2006: Bachelor of Science (Physics) |
| | Mahidol University, 2006-2010: Master of Science (Physics) |
| **HOME ADDRESS** | 844/42 Moo 1 Banlium, Amphur Mueng, Udonthani 41000, Thailand |
| | Tel. 0891517527 |
| | E-mail: beer_pj@yahoo.com |
| **PUBLICATIONS / PRESENTATION** | **P. Jitsomboonmit** and S. Dangtip. *Design of high voltage medium frequency power supply for plasma applications*, Proceeding of the 33rd Congress on Science and Technology of Thailand (STT 33), Walailak University, Nakhon Si Thammarat, Thailand, on October 18-20, 2007. |
| | **P. Jitsomboonmit**, M. Nisoa, and S. Dangtip. *Effect of Atmospheric Argon Plasma on Surface Properties of ITO Films*, Proceeding of Siam Physics Congress (SPC2009), Cha-am, Petchaburi, Thailand, on March 19-20, 2009. |